UNIVERSIDADE DE SÃO PAULO
INSTITUTO DE FÍSICA

Ânions Transientes de Moléculas Quirais

Julio Cesar Ruivo Costa

Orientado por Prof. Dr. Marcio Teixeira do Nascimento Varella

---

Uma tese apresentada ao Instituto de Física da Universidade de São Paulo como parte dos requisitos necessários para o exame de doutoramento em Física.

Banca examinadora:

Prof. Dr. Marcio Teixeira do Nascimento Varella (IFUSP)
Prof. Dr. Caetano Rodrigues Miranda (IFUSP)
Prof. Dr. Guilherme Menegon Arantes (IQUSP)
Profa. Dra. Jimena Diaz Gorfinkiel (Open University)
Prof. Dr. Timothy J. Gay (University of Nebraska)

São Paulo
2021

FICHA CATALOGRÁFICA
Preparada pelo Serviço de Biblioteca e Informação
do Instituto de Física da Universidade de São Paulo

Costa, Julio Cesar Ruivo

Anions transientes de moléculas quirais. São Paulo, 2022.

Tese (Doutorado) – Universidade de São Paulo. Instituto de Física. Depto. de Física Geral.

Orientador: Prof. Dr. Márcio Teixeira do Nascimento Varella
Área de Concentração: Modelagem Molecular

Unitermos: 1. Física molecular; 2. Química quântica; 3. Estrutura molecular (Química teórica); 4. Espalhamento; 5. Modelagem molecular.

USP/IF/SBI-019/2022

UNIVERSITY OF SÃO PAULO
INSTITUTE OF PHYSICS

Transient anion states of chiral molecules

Julio Cesar Ruivo Costa

Advised by Prof. Dr. Marcio Teixeira do Nascimento Varella

A thesis presented to the Institute of Physics of the University of São Paulo in partial fulfillment of the requirements for the PhD in Physics exam.

Dissertation committee:

Prof. Dr. Marcio Teixeira do Nascimento Varella (IFUSP)
Prof. Dr. Caetano Rodrigues Miranda (IFUSP)
Prof. Dr. Guilherme Menegon Arantes (IQUSP)
Prof. Dr. Jimena Diaz Gorfinkiel (Open University)
Prof. Dr. Timothy J. Gay (University of Nebraska)

São Paulo
2022

O presente trabalho foi realizado com apoio do CNPq, Conselho Nacional de Desenvolvimento Científico e Tecnológico - Brasil

Acknowledgments

This work was made possible due to dozens of collaborations, in so many different aspects that it would be extremally hard to pay all my gratitude here. Firstly, I would like to express my special thanks to my advisor and friend Marcio, for all his patience and guidance and the inspiration he arose in me. Also, I would like to acknowledge my colleagues and friends from the Physics Institute/USP, and mainly my coworking research group, who are all my friends, for all the support, help and the companionship they offered me. Each one had an enormous contribution in my work and life. I would also like to thank two special collaborators in this journey, Fábris Kossoski and Lucas Cornetta, two friends that I admire so much and were so generous to me. I also thank Marie for all her dedication teaching me, which strongly contributed to overcoming the language barrier.

In addition, I would like to thank my family in Portuguese, which is my native language. Agradeço ao apoio incondicional da minha família para que essa jornada fosse vivenciada. Ao apoio e companheirismo do meu irmão, Marco; à confiança e preparo de uma vida toda propiciado pela minha mãe, Luiza; à minha namorada, que se tornou minha companheira, e que se tornou minha esposa, Sarah, que me acompanhou por toda a aventura vivida, e que eu amo completamente.

To conclude, I would like to express my thanks to the committee for receiving and appreciating this work. I would also like to acknowledge the Graduation Department of the Institute of Physics for their support, as well as all the entire Institute staff. Finally, I would like to thank the financial support given by the Brazilian National Council for Scientific and Technological Development (CNPq), which has been bravely resisting the struggles we have been passing through, as the entire national scientific community.

Do not fear mistakes. There are none.

Miles Davis

Abstract

We present a study of anionic states of halocamphor molecules, in which we characterize mechanisms that should produce electron circular dichroism by chiral molecules. We evaluate the electronic cross section for elastic scattering for the 3-bromocamphor, the 3-iodocamphor and the 10-iodocamphor. The results show resonances that give rise to well known spin polarized electron transmission and dissociation asymmetries, which have been observed experimentally but not fully understood. We also presented a developed model for the electron scattering problem accounting for the spin-orbit interaction. We predicted the transmission and dissociation asymmetries for the halocamphor molecules, obtaining clarifying results. We show that the resonance energy, the lifetime, the occupied orbital character, and the potential energy surface topology are fundamental ingredients in the halocamphor chiral sensitivity. This study is an important contribution towards understanding the chiral selectivity in the biomolecules, an interesting problem for the scientific community.

Keywords: halocamphor – electron scattering – spin-polarization – chirality – chiral sensitivity – dissociation - asymmetry

Resumo

Nesta dissertação apresentamos um estudo dos estados aniônicos de halocânforas, no qual caracterizamos mecanismos capazes de produzir dicroísmo de elétrons circularmente polarizados por moléculas quirais. Nós calculamos as seções de choque eletrônicas para espalhamento elástico produzidas por 3-bromocânfora, 3-iodocânfora e 10-iodocânfora. Os resultados indicam ressonâncias, as quais devem gerar conhecidas assimetrias de transmissão eletrônica e de dissociação, obtidas experimentalmente, mas não totalmente explicadas. Também apresentamos um modelo desenvolvido para contabilizar a interação de spin-órbita no problema de espalhamento eletrônico, bem como a predição das assimetrias de transmissão e de dissociação. Nós mostramos que as características físicas das ressonâncias, como energia de formação, tempo de vida típico, caráter do orbital ocupado e topologia da superfície de energia potencial são elementos fundamentais na produção de sensibilidade quiral das halocânforas. Este estudo é uma importante contribuição para a compreensão do problema de seletividade quiral em biomoléculas, alvo de interesse por décadas pela comunidade científica.

Palavras-chave: halocânforas – espalhamento de elétrons – polarização – quiralidade – dissociação – sensibilidade quiral - assimetria

Transient Anion state of Chiral Molecules

Contents

List of Figures

Chapter 1

Introduction

In all known forms of life on Earth, the chiral molecules have only one definite handedness. For example, amino acids are only found in L enantiomer form, while sugars are only found as D enantiomers [2]. In biomolecules, amino acids are not found in the D enantiomer form, or sugars found as L enantiomers. Even the stable DNA structure itself is chiral and exists as a single enantiomer, where its helix only rotates in one sense. Explaining the causes of chiral selectivity in the biomolecules is a challenge for the science community.

One theory that attempts to explain this biological homochirality is the **Vester-Ulbricht (VU) hypothesis**. Vester and Ulbricht proposed that a connection could be established between asymmetry at the level of elementary particles and at the molecular level, which could have destroyed the initial balance between left-handed and right-handed molecules in the early stages of life on Earth [3]. Negative β particles (electrons) have a longitudinal spin polarization in the opposite direction of their motion. For the z component of spin ($\boldsymbol{\sigma_z} = \pm\hbar/2$) defined along their wave vector $\vec{k}$, they have $\boldsymbol{\sigma}\cdot\vec{k} < 0$, and they are called **left-handed particles**. Similarly, the longitudinal spin polarization of positive β particles (positrons) along their direction of motion is positive ($\boldsymbol{\sigma}\cdot\vec{k} > 0$), and they are called **right-handed particles** [4]. There are many more electrons than positrons in the Universe. As a consequence, the particles emerging from β-decay of radioactive nuclei are predominantly left-handed. According to the VU hypotesis, electrons are related by mirror-image symmetry which is, in principle, the same as that which gives rise to optical activity in chemical compounds. Electrons might thus selectively destroy a given enantiomer of chiral biomolecules. Fig. 1.1 illustrates the process proposed by the VU hypothesis. Several experiments have attempted to verify the VU conjecture, but they

have often been inconclusive [5]. The observation of chirally dependent electron-molecule interactions remained an open challenge for many years.

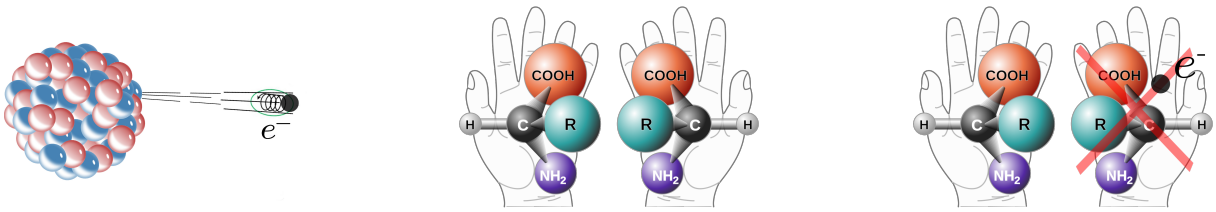

(a) (b) (c)

Figure 1.1: Scheme of the Vester-Ulbricht hypothesis. (1.1a): β-decay of radioactive nuclei producing electron with left-handed spin polarization. (1.1b): L and D enantiomers of a chiral species. (1.1c): The D enantiomer destroyed by the interaction with the left-handed electron, for example.

The first observation of spin-dependent electron scattering from optically active molecules was reported by Cambell and Farago in Nature, in 1985. The measurements indicate that spin-polarized electrons can distinguish right- and left-handed isomers, a phenomenon analogous to optical circular dichroism [6]. The latter study was followed by the gas-phase electron scattering experiments performed by the Münster group [7, 1]. In these experiments, an electron beam with low energy (< 10 eV) passes through a vapor of enantiomerically pure molecules. The electron beam is set up with an initial spin polarization P defined by

$$P = \frac{N^+ - N^-}{N^+ + N^-}, \tag{1.0.1}$$

where $N^{+(-)}$ is the number of right(left)-handed electrons. The incident beam has a non-zero polarization ($P \sim 30\%$) and intensity I_0. The transmitted current $I(P)$ is collected, and its attenuation is measured, where the total cross section can be obtained from the Beer-Lambert Law. The experiment is then repeated with the reverse polarization ($-P$), and the transmitted current $I(-P)$ is collected. This process is performed for each enantiomer, and the **transmitted current asymmetry** is defined as

$$a_{D(L)} = \left[\frac{I(P) - I(-P)}{I(P) + I(-P)}\right]_{D(L)}, \tag{1.0.2}$$

where the D and L subscripts denote the molecular handedness. Fig. 1.2 shows an scheme of the process described above.

The preferential scattering of electrons with a given handedness by chirally pure sam-

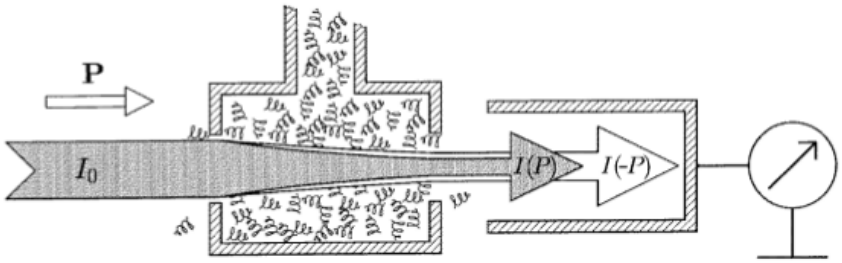

Figure 1.2: Scheme of the transmission experiment (reproduced from [1]). The incident electron beam I_0 has a spin polarization $P \sim 30\%$. The transmitted attenuated current $I(P)$ is collected after the gas cell. Then, the experiment is repeated with the inverse polarization $(-P)$, and the correspondent transmitted current $I(-P)$ is collected.

ples was named **electron circular dichroism (ECD)**, in analogy with the preferential absorption of circularly polarized light (optical circular dichroism). The experiments of the Münster group also point out two important things: **(i)** the transmitted current asymmetry has the same magnitude for L or D target molecules although with opposite signal, i.e., $a_D = -a_L$; **(ii)** the magnitude of the scattering asymmetry is enhanced by the formation of transient negative ions (resonances). It is well-known that the temporary capture of the incident electron gives rise to peaks (ideally Lorentzians) in the scattering cross sections [8], which are also evident in **electrons transmission spectroscopy (ETS)** measurements. The observed chiral asymmetries also show structures at the same energies where ETS measurements point out the formation of resonances, as illustrated in Fig. 1.3.

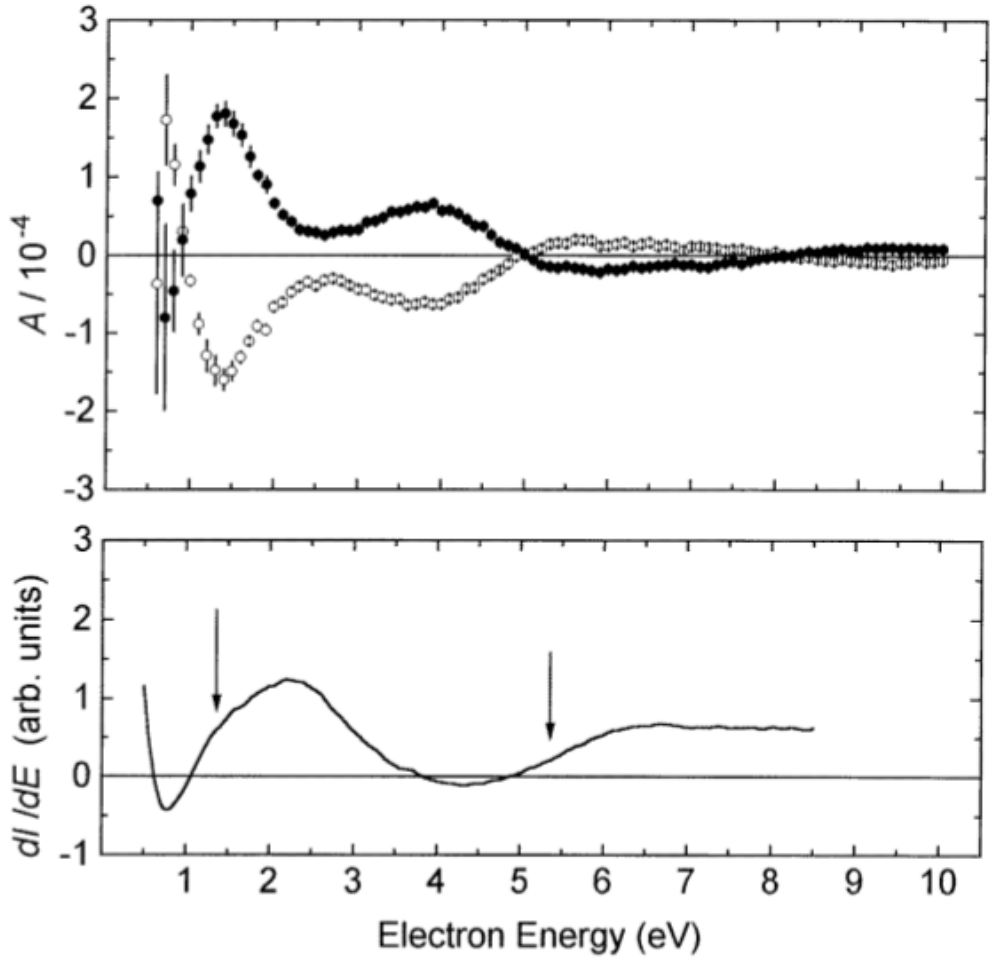

Figure 1.3: Asymmetry and electron transmission measured for 3-bromocamphor (adapted from [1]). Upper panel: scattering asymmetry A measured for D-bromocamphor (•) and L-bromocamphor (∘). The error bars give the statistical uncertainties. Bottom panel: derivative (dI/dE) of the transmitted current (ETS measurements). The resonance energies are indicated by the arrows. The resonances observed in ETS correlate with the structures in the asymmetry measurements.

The possible mechanisms underlying ECD were discussed by Farago [9, 10]. Chirally sensitive electron scattering arises from the spin-orbit interaction and comprise three effects:

- The spin-orbit coupling of the continuum electron interacting with a heavy atom is called **Mott scattering**. This mechanism would involve a Coulombic scattering from a light atom, and simultaneously, the Mott-scattering from a heaviest atom (Fig. 1.4). The first scattering is spin-independent, therefore the Coulomb interaction produces an electron deflection, whereas the spin remains the same. That turns the incident longitudinally spin polarized electron into a transverse one. The Mott scattering from the target's heaviest atom leads to asymmetric scattering of the two possible spin directions. A precise calculation of this effect for polyatomic molecules is a challenging collision problem. Its order of magnitude, however, can be estimated as $\propto Z^2$ [11], where Z is the atomic number of the heaviest atom in the target molecule.

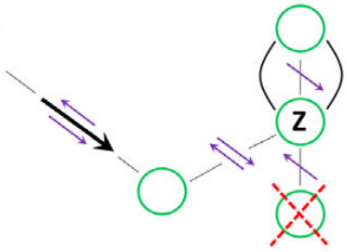

Figure 1.4: Scheme of Mott scattering (reproduced from [12]). Heavy and light arrows indicate electronic momenta and spins, respectively. Incident electrons arrives from the upper left, and it interacts with a light atom through the Coulomb interaction. The electron trajectory changes, but the spin remains the same. Thereafter, the electron interacts with a heaviest atom (with atomic number $\boldsymbol{Z}$) through the Mott scattering, with a predominant resulting spin.

- In the scattering process, the incident spin polarized electron and the target molecule are subjected to the exchange interaction, mediated by the target helicity density. The **helicity density** is produced by the spin-orbit coupling of the target electrons and the target nuclei. The description of spin-orbit effect concerns a linear combination of triplet and the singlet states, which gives rise to the exchange interaction. The helicity operator is defined as $\vec{k_i}\cdot\boldsymbol{\sigma_i}$, where $\vec{k_i}$ is the i-th electron momentum vector, and $\boldsymbol{\sigma_i}$ is the i-th electron spin. Thus, the helicity density corresponds to

the expectation value of the helicity operator over all the targets electrons,

$$\sum_i \langle \Phi_0 | \vec{k_i} \cdot \boldsymbol{\sigma_i} \, | \Phi_0 \rangle, \tag{1.0.3}$$

where Φ_0 is the target ground state. For the helicity density to be nonzero, the spin-orbit coupling must be included and the electronic states must not be parity eigenstates. Therefore, for optically inactive molecules, the helicity density is zero, but for a chiral species, this measurement is non-zero. In addition, the helicity density is a pseudoscalar under space inversion operator, which implies that its value for a given enantiomer has the opposite sign of the other. Since this effect depends of the target chirality, different enantiomes brings different contributions for the spin-dependent scattering (see Fig. 1.5). Once helicity density depends of the nuclei, as well as the molecular geometry, its size effect have dependence on higher Z^2 as closely as is the heaviest atom from the chiral center of molecule [13].

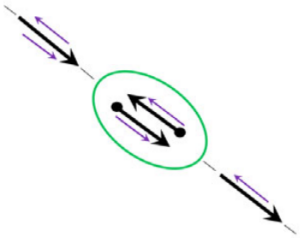

Figure 1.5: Schematic diagram of the helicity density process (reproduced from [12]). Heavy and light arrows indicate electronic momenta and spins, respectively. Incident electron arrives from the upper left, and it interacts with a target molecule (green elipse), with nonzero helicity density. An electron with a given spin projection is preferentially transmitted.

- The spin-orbit coupling between the incident electron and the target electrons is called **spin-other-orbit**. This effect may produce ECD, similar to the way it causes the optical activity and photonic circular dichroism [14]. The electromagnetic field from the incident electron induces a helical current in the target, producing a magnetic dipole moment. The spin of this incident electron would interact differently with this dipole, depending on whether it is forward or backward (see Fig. 1.6). Although this coupling would have no explicit Z dependence, it may tend to be related with the total atomic weight of the molecule [15].

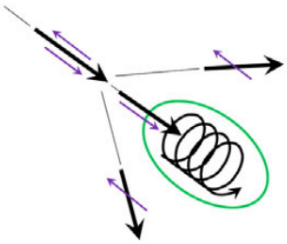

Figure 1.6: Schematic diagram of spin-other-orbit (obtained from [12]). The incident electrons induce a magnetic dipole current in target, and it interacts with an electron with a preferential spin.

More recently, a second generation of experiments was performed and reported by Dreiling and Gay [12]. A low-energy incident electron beam (≤ 0.6 eV) could interact with halocamphor targets in the gas phase, producing **dissociative electron attachment (DEA)**. Once an electron is attached to a molecule, giving rise to a resonance, one of the possible decay channels is the dissociation of the anion species. DEA generally refers to electron-induced dissociation [16], and the reactions observed in the experiments performed by the Gay group can be represented as

$$\mathrm{CX} + \mathrm{e}^- \longrightarrow \mathrm{CX}^- \longrightarrow \mathrm{C}^\bullet + \mathrm{X}^-, \tag{1.0.4}$$

where $\mathrm{C}^\bullet$ is the camphor radical and $\mathrm{X} = \mathrm{Br}, \mathrm{I}$, is an halogen atom. The yeld of anion fragments (X^-) was measured as function of the spin polarization of the incident electrons, and the dissociation asymmetry was defined as

$$A = a_L - a_D = \left[\frac{I\uparrow - I\downarrow}{I\uparrow + I\downarrow}\right]_L - \left[\frac{I\uparrow - I\downarrow}{I\uparrow + I\downarrow}\right]_D, \tag{1.0.5}$$

where, in this case, $I\uparrow$ ($I\downarrow$) is the current of anion fragments produced by incident spin-forward (spin-backward) electrons. The DEA asymmetry is analogous to the scattering asymmetry defined above (eq. 1.0.2), but concerns the current of anion fragments, as opposed to the current of quasi-elastically scattered electrons. The observed chirally selective degradation (dissociation) of molecules is consistent with the principle underlying the VU hypothesis, and was highlighted as an Editor's Choice in the Physical Review Letters. Subsequent experiments explored the DEA asymmetry of 3-bromocamphor (3BrC), 3-iodocamphor (3IC) and 10-iodocamphor (10IC) [12], and the results were puzzling. As

shown in Fig. 1.7, there is a significant difference in magnitude between the asymmetry of 3IC and 10IC, which is inconsistent with the $Z2$ dependence expected from the ECD mechanisms described above.

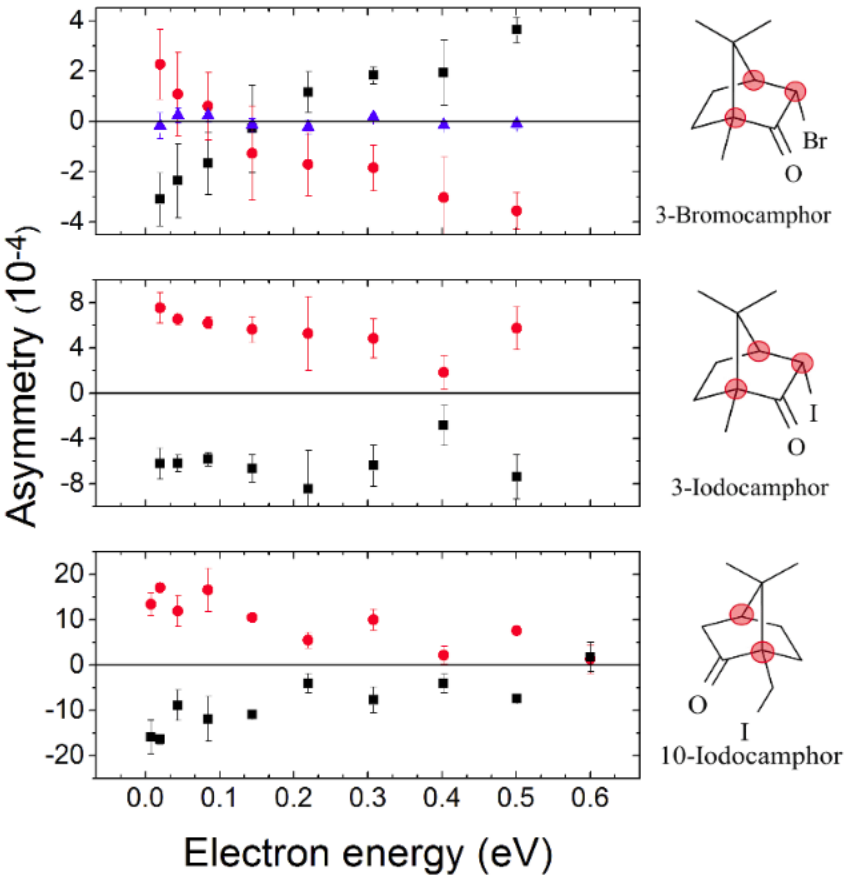

Figure 1.7: The DEA asymmetry as a function of the electron incident energy (adapted from [12]). Squares and circles represent opposite initial polarizations (P and $-P$), which should give rise to asymmetry measurements of opposite signs. The triangles indicate data taken with a racemic mixture of bromocamphor. The 10IC maximum asymmetry is 4 times greater than the 3IC maximum asymmetry.

The maximum asymmetry in 10IC (A_{10IC}) is about **100% greater than the maximum obtained in 3IC** (A_{3IC}), and about **300% greater than the maximum asymmetry obtained in 3BrC (A_{3BrC})**. Since this result contradicts all theoretical predictions, it was called "Anomalously Large" [12]. The expected results from the ECD are discussed below:

- Since $Z_I^2/Z_{Br}^2 \sim 2$, it was expected $A_{3IC} \approx 2 \cdot A_{3BrC}$, when considering the Mott and helicity density mechanisms as the main cause of these asymmetries.

- A_{10IC} was expected to be **less**, or at least **equal** to A_{3IC}. Both target molecules have the same heavy atom, but in 10IC the halogen is separated by two bonds from the

nearest chiral center, whereas in 3IC the halogen is immediately bound to a chiral carbon.

- The helicity density of the three molecules was calculated in Ref. [12] and shows a **negligible value for 10IC**, which indicate this mechanism is not the main cause of the asymmetry either.

The current lack of understanding about chirally sensitive dissociation is perharps best illustrated by the following remark by Dreiling *et al.* [12]:

> "This work thus points out the need for the development of fundamental quantum-dynamic calculations to provide a first, rudimentary understanding of the magnitudes and energy dependence of the asymmetries we observe. Even a qualitative theoretical picture of such effects would significantly improve our understanding of other, related areas such as low-energy electron-induced damage of biomolecules."

Very little is known about the dynamics of electron-halocamphor collisions, in particular the resonance spectra of those systems. In general, shape resonances, i.e., those formed by electron attachment to the ground state of the target molecule, are named π^* or σ^* in reference to the character of the virtual orbitals chiefly involved in the attachment. Those resonances are known to trigger DEA processes in biomolecules [16], such that a better understanding about the transient anion states of the halocamphors and the expected dissociation pathways would be crucial to interpret the experimental data of the Nebraska group. In addition, despite the basic knowledge on ECD mechanisms [9, 11, 13] and fundamental symmetry properties underlying the scattering asymmetries [10, 17], there is no available theory for the DEA asymmetries.

Describing collisions is a significant numerical challenge. Thus, an efficient methodology capable of performing scattering calculations quantum mechanically is essential. **The parallel version of the Schwinger Multichannel method implemented with pseudopotentials (SMCPP) is a particularly suitable tool for this purpose.** Our group has investigated the temporary electron occupation by elastic scattering calculations using the SMCPP. We have applied this method to infer dissociation mechanisms [18], which is broadly discussed in several studies involving halogenated DNA and RNA bases [19, 20, 21, 22]. We present in this work the integral cross sections of electron scattering with energies below 6 eV for the three halocamhor molecules. The anionic spectra

is analyzed and their resonances are characterized, from which we infer the molecular dissociative mechanisms due to electron attachment. In addition, a model for the spin-dependent electron scattering problem under the influence of a low energy resonance is proposed. Having understood the halocamphor dissociation mechanisms, this model explains the asymmetries in DEA current, in which the **Feshbach projection operator (FPO) formalism** is applied [23]. The FPO is a powerful method for the description of resonant scattering and reactions, based on the introduction of operators which project the scattering states onto the discrete states of the system and the continuous spectrum. Since the asymptotic scattering states are ruled by resonances, one can derive the vibrational excitations and the dissociation cross sections [24]. We focus on aspects of the collision dynamics, in which the most relevant novel aspect is the description of vibrationally inelastic scattering channels under influence of the Coulomb and the spin-orbit potentials. Having characterized the halocamphor low-lying states and proposed this model, we present estimates for the transmission and DEA asymmetries. We show the resonance lifetime, as well as the relaxation along the C-X pathway, have an important role in the asymmetry production.

The text is organized as follows. In the next chapter, we treat the scattering theories considered in this work, as well as the main formulation for quantum mechanics calculations. We discuss the basics of spinless scattering, and we present the SMCPP method for electronically elastic scattering. A review of spin-dependent electron scattering is presented, with the formulation of a scattering matrix and its symmetry properties. Then, we present a brief discussion about spin-dependent DEA and vibrational excitation, based on the FPO approach. The subsequent chapter presents the characterization of the anionic states, obtained so far for elastic electron scattering from the halocamphor molecules, as well as adjunct calculations, and the respective discussion. We then present results for the estimated transmission asymmetry and the DEA asymmetry. Finally, a concluding chapter summarizes our main points and challenges concerning this investigation.

Chapter 2

Theory and Methods

We present in this chapter a description of the scattering theories considered in this project. The first section is a brief discussion of the non relativistic scattering theory. We also present a short discussion about the optical theorem, the concept of resonance, and the frames of reference in which the scattering is described.

In the second section, we outline the Schwinger Multichannel Method (SMCPP) and its numerical aspects, such as the computational details and the inclusion of pseudopotentials. In the third section, we discuss the spin-dependent electron scattering theory formulated by Blum and Thompson [17]. The fourth section is dedicated to the dynamical aspects involving spin-polarized electron scattering from chiral molecules. In that section, we generalize the theory presented by Frandeyer, Thompson and Blum [25] for vibrationally inelastic scattering channels, especially the reactive dissociation electron attachment (DEA) channel. The fifth section concerns the Feshbach Projection Operator (FPO) and its approach to spin dependent scattering. There, we present a brief outline of the spin-independent FPO formalism and then we generalize it for the inclusion of the spin-orbit interaction.

2.1 Basics of scattering theory

We approach in this section the quantum electron scattering from a target molecule. The idea consists rewriting the Schrödinger equation in an integral form that incorporates the appropriate boundary condition, which is known as the Lippmann-Schwinger equation. It is the first step for the Schwinger Multichannel Method, as well as the Feshbach Projection Operator, which we treat later. The potential-scattering formulation can be found in quantum mechanics handbooks, such as Sakurai's Modern Quantum Mechanics [26]. However, at this level, we consider the target molecule in a many-body picture, with the electrons treated explicitly, and the molecular atoms within the Born-Oppenheimer approximation. We consider only the electronic degrees of freedom keeping the nuclei fixed.

Let us consider an incident electron traveling with the wave vector $\boldsymbol{k}$. The electron collides with a molecule composed of M nuclei and N electrons. We denote by V the Coulomb potential between the incident particle and the target, such that, the scattering Hamiltonian is given by

$$H = T_{N+1} + H_N + V, \tag{2.1.1}$$

where T_{N+1} is the kinetic energy of the incident electron and H_N is the Hamiltonian of the N-electron target. The electron-molecule scattering potential is given by the electron-electron and electron-nucleus interactions,

$$V = \sum_{A=1}^{M} \frac{-Z_A}{|\boldsymbol{r}_{N+1} - \boldsymbol{R}_A|} + \sum_{j=1}^{N} \frac{1}{|\boldsymbol{r}_{N+1} - \boldsymbol{r}_j|}, \tag{2.1.2}$$

where the $\boldsymbol{R}_A$ are the nuclear vector coordinates, $\boldsymbol{r}_j$ the electronic vector coordinates, and Z_A the electronic charge of A-th nuclei. We use atomic units in the entire formulation ($\hbar = m = e = 1$).

In an electron-molecule collisions, different phenomena can occur, such as elastic scattering, ionization, dissociation, electronic or vibrational excitation, etc. **Each possible process is called a channel**. We denote the entrance channel by the index Γ, which represents a complete set of quantum numbers defining the initial state of the system. On the other hand, the scattering channel is denoted by the index Γ', which represents a complete set of quantum numbers defining the final state of the system. The viability of each

phenomenon to occur depends, naturally, on the conditions of the scattering process. For example, for an incident electron energy below the electronic excitation threshold of the molecule target, any electonic excitation channel is not allowed. Commonly, the allowed channels are called **open channels**.

The energy conservation principle imposes the initial and final system energies to be the same:

$$E = \frac{k_\Gamma^2}{2} + \epsilon_\Gamma = \frac{k_{\Gamma'}^2}{2} + \epsilon_{\Gamma'}, \tag{2.1.3}$$

where $k_\Gamma(k_{\Gamma'})$ is the initial (final) incident electron momentum, and $\epsilon_\Gamma(\epsilon'_\Gamma)$ is the initial (final) energy of the target-molecule state Φ_Γ.

Considering the Hamiltonian given by eq. (2.1.1), the Schrödinger equation of the scattering problem is given by

$$H\Psi_{\boldsymbol{k}_\Gamma}(\boldsymbol{r}_1, ..., \boldsymbol{r}_{N+1}) = E\Psi_{\boldsymbol{k}_\Gamma}(\boldsymbol{r}_1, ..., \boldsymbol{r}_{N+1}), \tag{2.1.4}$$

where $\Psi_{\boldsymbol{k}_\Gamma}(\boldsymbol{r}_1, ..., \boldsymbol{r}_{N+1})$ is the scattering wave function, which depends on the coordinates of $(N+1)$ electrons (spin states are omitted for simplicity). The asymptotic boundary condition requires that the scattering wave function, in the $r_{N+1} \to \infty$ limit, behaves as a superposition of the non interacting wave function and a perturbed electron wave function,

$$\Psi^{(\pm)}_{\boldsymbol{k}_\Gamma}(\boldsymbol{r}_1, ..., \boldsymbol{r}_{N+1}) \xrightarrow{r_{N+1}\to\infty} S_\Gamma + \sum_{\Gamma'}^{open} f_{\Gamma',\Gamma} \frac{\exp(ik_{\Gamma'} r_{N+1})}{r_{N+1}}, \tag{2.1.5}$$

where S_Γ is a solution of the non interacting problem ($H_0 = T_{N+1} + H_N$). The spherical wave function $\frac{\exp(ik_{\Gamma'} r_{N+1})}{r_{N+1}}$ is modulated by the scattering amplitude $f_{\Gamma',\Gamma}$, and the sum is over all the open channels. The $^{(\pm)}$ index refers to the boundary condition: $^{(+)}$ is related to a divergent spherical wave in the asymptotic limit, while $^{(-)}$ is related to a convergent spherical wave. The non interacting solution is given by the product of a plane wave with the molecular target wave function

$$S_\Gamma = \Phi_\Gamma \otimes \exp(i\boldsymbol{k}_\Gamma \cdot \boldsymbol{r}_{N+1}). \tag{2.1.6}$$

The **scattering amplitude** $f_{\Gamma',\Gamma}$ is the probability amplitude of the transition from

the Γ channel to the Γ' channel. This function contains all the information about the electron scattering, and therefore, it is the object of interest. The scattering amplitude can be formally defined [26] by

$$f_{\Gamma',\Gamma} = -\frac{1}{2\pi}\langle S_{\Gamma'}|V|\Psi_{\Gamma}^{(+)}\rangle, \tag{2.1.7}$$

and is associated with the electronic differential cross section

$$\frac{d\sigma}{d\Omega}(\boldsymbol{k}_{\Gamma'}, \boldsymbol{k}_{\Gamma}) = \frac{k_{\Gamma'}}{k_{\Gamma}}|f_{\Gamma',\Gamma}(\boldsymbol{k}_{\Gamma'}, \boldsymbol{k}_{\Gamma})|^2, \tag{2.1.8}$$

which is related to probability of a scattered electron in a solid angle $d\Omega$ in the direction of $\boldsymbol{k}_{\Gamma'}$. Figure 2.1 illustrates the electron scattering from a target molecule. It is worth mentioning that the integral cross section can be obtained from

$$\begin{aligned}\sigma(\boldsymbol{k}_{\Gamma'}, k_{\Gamma}) &= \int d\hat{\boldsymbol{k}}_{\Gamma'}\frac{d\sigma}{d\Omega}(\boldsymbol{k}_{\Gamma'}, \boldsymbol{k}_{\Gamma}) \\ &= \int d\hat{\boldsymbol{k}}_{\Gamma'}\frac{k_{\Gamma'}}{k_{\Gamma}}|f_{\Gamma',\Gamma}(\boldsymbol{k}_{\Gamma'}, \boldsymbol{k}_{\Gamma})|^2,\end{aligned} \tag{2.1.9}$$

where $\int d\hat{\boldsymbol{k}}_{\Gamma'}$ is the 2-dimensional integral over all directions of $\boldsymbol{k}_{\Gamma'}$.

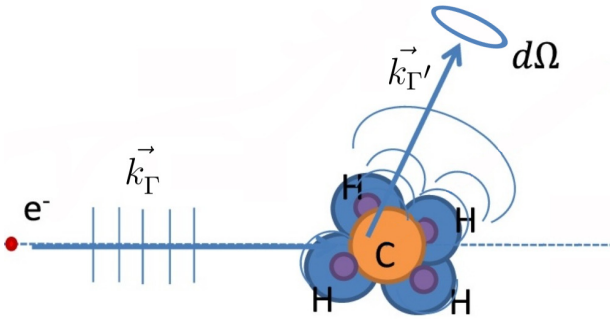

Figure 2.1: Scheme of electron scattering from a molecule target (adapted from [27]). The incident electron is represented by a plane wave with a wave vector $\boldsymbol{k}_{\Gamma}$. The scattered electron can be detected in the direction of $\boldsymbol{k}_{\Gamma'}$ and within the solid angle $d\Omega$.

2.1.1 The Lippmann-Schwinger Equation

The scattering Hamiltonian (2.1.1) can be decomposed in two parts, corresponding to the interaction-free Hamiltonian (H_0) and the scattering potential V,

$$H = H_0 + V, \tag{2.1.10}$$

$$H_0 = T_{N+1} + H_N. \tag{2.1.11}$$

The eigenstates and eigenvalues H_0 are assumed to be known:

$$H_0|S_\Gamma\rangle = \left(\epsilon_\Gamma + \frac{k_\Gamma^2}{2}\right)|S_\Gamma\rangle. \tag{2.1.12}$$

The separated Hamiltonian allows us to rewrite the Schrödinger equation as a non-homogeneous equation,

$$(E - H_0)|\Psi_{\boldsymbol{k}_\Gamma}\rangle = V|\Psi_{\boldsymbol{k}_\Gamma}\rangle, \tag{2.1.13}$$

where the general solution can be obtained from the superposition of S_Γ with a particular solution of (2.1.13) obtained from the Green's function method [8],

$$|\Psi_\Gamma^{(\pm)}\rangle_P = G_0^{(\pm)} V|\Psi_\Gamma^{(\pm)}\rangle_P. \tag{2.1.14}$$

The Green's operator associated to H_0 can be formally written as

$$G_0^{(\pm)} = \lim_{\varepsilon\to 0} \frac{I_{H_0}}{E - H_0 \pm i\varepsilon}, \tag{2.1.15}$$

where the identity operator I_{H_0} is given by product

$$I_{H_0} = I_N \otimes I_{\boldsymbol{k}}. \tag{2.1.16}$$

Here, I_N is the identity operator in the space generated by the molecular eigenstates and $I_{\boldsymbol{k}}$ is the identity operator in the continuum energy space of the incident electron. The identity operator can be written in the basis of the eigenstates of the H_0 operator ($|\Phi_l \boldsymbol{k}\rangle\langle\Phi_l \boldsymbol{k}|$) and consequently, the Green's operator can be represented in the same basis,

$$G_0^{(\pm)} = \lim_{\varepsilon\to 0} \sum\!\!\!\!\!\!\int_l \int d^3k \frac{|\Phi_l \boldsymbol{k}\rangle\langle\Phi_l \boldsymbol{k}|}{\frac{k_l^2}{2} - \frac{k^2}{2} \pm i\varepsilon}, \tag{2.1.17}$$

where the symbol $\sum\!\!\!\!\!\!\int_l$ means the sum over the l discrete target spectrum and integra-

tion over the continuum spectrum. In the above expression, we made the substitutions $H_0|\Phi_l \boldsymbol{k}\rangle = (E_l + \frac{k^2}{2})|\Phi_l \boldsymbol{k}\rangle$, and $E = E_l + \frac{k_l^2}{2}$ with aid of the energy conservation principle, as in eq. (2.1.3).

The formal solution of the scattering problem is obtained through an integral equation which incorporates the asymptotic boundary conditions, and is called **Lippmann-Schwinger equation**,

$$|\Psi_\Gamma^{(\pm)}\rangle = |S_\Gamma\rangle + G_0^{(\pm)} V |\Psi_\Gamma^{(\pm)}\rangle. \tag{2.1.18}$$

The divergent solution ($\Psi_{\boldsymbol{k}_\Gamma}^{(+)}$) has a physical meaning in the collision process, whereas the convergent solution ($\Psi_{\boldsymbol{k}_\Gamma}^{(-)}$) does not correspond to an expected behavior in the electron scattering. However, both solutions are mathematically possible and will be employed in the Schwinger Variational Principle in the next section.

2.1.2 The transition operator and the optical theorem

Now, we discuss two important elements in scattering theory that will be useful. The first one is the **transition operator** (T) or the **transition matrix**, which is defined by

$$V|\Psi^{(\pm)}\rangle = T|S_\Gamma\rangle. \tag{2.1.19}$$

We multiply from the left the Lippmann-Schwinger equation (2.1.18) by the interaction operator V,

$$V|\Psi_\Gamma^{(\pm)}\rangle = V|S_\Gamma\rangle + V G_0^{(\pm)} V |\Psi_\Gamma^{(\pm)}\rangle, \tag{2.1.20}$$

and using (2.1.19), we obtain

$$T = V + V \frac{I_{H_0}}{E - H_0 \pm i\varepsilon} V. \tag{2.1.21}$$

We replace $V|\Psi^{(\pm)}\rangle$ by $T|S_\Gamma\rangle$ in the scattering amplitude defined in (2.1.7), and using the expression for T developed above, we obtain the scattering amplitude in terms of the transition operator,

$$f_{\Gamma',\Gamma} = -\frac{1}{2\pi}\langle S_{\Gamma'}|T|S_\Gamma\rangle. \tag{2.1.22}$$

The transition operator carries all the information about the scattering

process, and its matrix elements correspond to the scattering amplitude. From the eq. (2.1.22), we can derive the **optical theorem**, which relates the imaginary part of the forward scattering amplitude to the total cross section.

Forward scattering consists of the elastically scattered electron in the incident direction, $\boldsymbol{k_\Gamma} = \boldsymbol{k'_\Gamma}$. Therefore, the forward scattering amplitude is given by

$$f_{\Gamma,\Gamma}(\boldsymbol{k_\Gamma}, \boldsymbol{k_\Gamma}) = -\frac{1}{2\pi}\langle S_\Gamma|T|S_\Gamma\rangle. \tag{2.1.23}$$

We next evaluate $\mathrm{Im}\langle S_\Gamma|T|S_\Gamma\rangle$ using (2.1.19), (2.1.18), and the hermiticity of V,

$$\begin{aligned}\mathrm{Im}\langle S_\Gamma|T|S_\Gamma\rangle &= \mathrm{Im}\langle S_\Gamma|T|\Psi^{(+)}\rangle \\ &= \mathrm{Im}\left[\Big(\langle\Psi^{(+)}| - \langle\Psi^{(+)}|V\frac{I_{H_0}}{E-H_0-i\varepsilon}\Big)V|\Psi^{(+)}\rangle\right].\end{aligned} \tag{2.1.24}$$

Now we use the well-known relation [26]

$$\frac{I_{H_0}}{E-H_0-i\varepsilon} = \mathbf{P}\Big(\frac{I_{H_0}}{E-H_0}\Big) + i\pi\delta(E-H_0), \tag{2.1.25}$$

where $\mathbf{P}$ is the Cauchy principal value, to reduce the right-hand side of (2.1.24) to the form

$$\begin{aligned}&\mathrm{Im}(\langle\Psi^{(+)}|V|\Psi^{(+)}\rangle) - \\ &\quad - \mathrm{Im}\langle\Psi^{(+)}|V\mathbf{P}\Big(\frac{I_{H_0}}{E-H_0}\Big)V|\Psi^{(+)}\rangle - \\ &\quad\quad - \mathrm{Im}(\langle\Psi^{(+)}|Vi\pi\delta(E-H_0)V|\Psi^{(+)}\rangle.\end{aligned} \tag{2.1.26}$$

The first two terms of (2.1.26) vanish because V and $V\mathbf{P}\Big(\frac{I_{H_0}}{E-H_0}\Big)V$ are hermitian and demand that these terms must be real. Hence, the expression reduces to

$$-\pi\langle\Psi^{(+)}|V\delta(E-H_0)V|\Psi^{(+)}\rangle. \tag{2.1.27}$$

Again, we can recast (2.1.27) using (2.1.19) as

$$\mathrm{Im}\langle S_\Gamma|T|S_\Gamma\rangle = -\pi\langle S_\Gamma|T^\dagger\delta(E-H_0)T|S_\Gamma\rangle. \tag{2.1.28}$$

To insert the identity operator of the H_0 space, we made the substitutions $H_0|S_{\Gamma'}\rangle = (E'_l + \frac{k^2_{\Gamma'}}{2})|S_{\Gamma'}\rangle$, and $E = E_l + \frac{k_l^2}{2}$, to obtain

$$
\begin{aligned}
\mathrm{Im}\langle S_\Gamma|T|S_\Gamma\rangle &= -\pi \sum\!\!\!\!\!\!\int_{l'} \int d\hat{\boldsymbol{k}}_{\Gamma'} \langle S_\Gamma|T^\dagger \delta(E-H_0)|S_{\Gamma'}\rangle\langle S_{\Gamma'}|T|S_\Gamma\rangle \\
&= -\pi \sum\!\!\!\!\!\!\int_{l'} \int d\hat{\boldsymbol{k}}_{\Gamma'} \langle S_\Gamma|T^\dagger|S_{\Gamma'}\rangle \delta\Big(\frac{k_l^2}{2} - \frac{k_{l'}^2}{2}\Big)\langle S_{\Gamma'}|T|S_\Gamma\rangle \\
&= -\pi k_\Gamma \int d\hat{\boldsymbol{k}}_{\Gamma'} \frac{k_{\Gamma'}}{k_\Gamma} |\langle S_{\Gamma'}|T|S_\Gamma\rangle|^2.
\end{aligned}
\tag{2.1.29}
$$

We recognize the last term as the integral cross section defined in eq. (2.1.9), and rewriting the left-hand side using (2.1.23), we finally obtain

$$
\mathrm{Im}\, f_{\Gamma,\Gamma}(\boldsymbol{k}_{\boldsymbol{\Gamma}}, \boldsymbol{k}_{\boldsymbol{\Gamma}}) = \frac{k_\Gamma}{4\pi}\sigma(\boldsymbol{k}_{\boldsymbol{\Gamma}}). \tag{2.1.30}
$$

The above derivation of the optical theorem which we discuss is restricted to elastic scattering. However, the optical theorem can be shown to be more general. It can be applied even in case inelastic channels are present, by replacing the integral cross section by the total cross section, $\sigma \to \sigma_{tot}$, where the latter comprises a sum over the energy-allowed collision channels. We will use that relationship in the next sections, to discuss the spin-dependent scattering and the reactive channels.

2.1.3 The Molecular frame and the Lab frame of reference

We have discussed the scattering amplitude to study the electron-molecule scattering. However, we did not define any frame of reference. We can define the molecular reference frame (MF), where it is usual to solve the electronic structure of the target molecule (H_N). On the other hand, for comparison with experimental results, it is necessary to consider the laboratory frame of reference (LF), with the z axis defined along the incident electron beam direction, and the target molecule in a defined orientation.

To transform from the MF to the LF, we first expand the outgoing angular dependence of the MF scattering amplitude in a linear combination of spherical harmonics,

$$
f(\boldsymbol{k}_{\Gamma'}, \boldsymbol{k}_\Gamma) = \sum_{l=0}^{l_{max}} \sum_{m=-l}^{+l} \tilde{f}_{l,m}(k_{\Gamma'}, \boldsymbol{k}_\Gamma) Y_l^m(\hat{\boldsymbol{k}}_{\Gamma'}), \tag{2.1.31}
$$

where the inverse transform is defined by

$$
\tilde{f}_{l,m}(k_{\Gamma'}, \boldsymbol{k}_\Gamma) = \int d\hat{\boldsymbol{k}}_{\Gamma'} Y_l^{m*}(\hat{\boldsymbol{k}}_{\Gamma'}) f(\boldsymbol{k}_{\Gamma'}, \boldsymbol{k}_\Gamma). \tag{2.1.32}
$$

In the laboratory frame, with the coordinates (x', y', z'), we assume the incident beam direction $\hat{\boldsymbol{k}}'_\Gamma$ is parallel to z' axis. The molecular frame (x, y, z) can be rotated to the laboratory frame to using the Wigner matrix $D^{(l)}_{m,m'}(\varphi, \theta, \gamma)$ [28], where φ, θ and ϕ are the Euler angles associated to rotation $(x, y, z) \to (x', y', z')$. The spherical harmonics, as functions of $\hat{\boldsymbol{k}}'_{\Gamma'}$, are rotated from the laboratory frame to the molecular frame by

$$Y^m_l(\hat{\boldsymbol{k}}_{\Gamma'}) = \sum_{m'} D^{*(l)}_{m',m}(\varphi, \theta, \gamma) Y^{m'}_l(\hat{\boldsymbol{k}}'_{\Gamma'}), \tag{2.1.33}$$

where $\hat{\boldsymbol{k}}'_{\Gamma'}$ is the electron scattered wave vector in the laboratory frame (note the "prime" over k), and $D^{*(l)}_{m,m'}(\varphi, \theta, 0)$ is the reverse rotation $(x', y', z') \to (x, y, z)$. We use (2.1.33) in (2.1.31) to obtain the scattering amplitude in the laboratory frame:

$$f^{(lab)}(\boldsymbol{k}'_{\Gamma'}, \boldsymbol{k}_\Gamma) = \sum_{l,m,m'} \tilde{f}_{l,m}(k_{\Gamma'}, \boldsymbol{k}_\Gamma) D^{*(l)}_{m,m'}(\varphi, \theta, 0) Y^{m'}_l(\hat{\boldsymbol{k}}'_{\Gamma'}). \tag{2.1.34}$$

The differential cross section in the laboratory frame can be obtained from the expression above using the eq. (2.1.8),

$$\frac{d\sigma}{d\Omega}^{(lab)}(k_\Gamma, \boldsymbol{k}'_{\Gamma'}) = \frac{k_{\Gamma'}}{k_\Gamma} \int d\hat{\boldsymbol{k}}_\Gamma |f^{(lab)}(\boldsymbol{k}'_{\Gamma'}, \boldsymbol{k}_\Gamma)|^2. \tag{2.1.35}$$

In electron collision experiments, the molecular sample is usually in the gas phase, where the molecules are randomly oriented. Therefore, the integral over $d\hat{\boldsymbol{k}}_\Gamma$ represents **the average over the molecular orientations in the LF**, or equivalently, the average over all incidence directions of the beam, in the MF. The integral cross section, $\sigma(k_\Gamma, k_{\Gamma'})$, can be obtained using (2.1.9), where it is already considered the average over the molecular orientations.

2.1.4 Resonances

At low collision energies, the incident electron may attach to the target molecule. Electron attachment produces a transient state with energy higher than the isolated target. This process generates a metastable state that lasts while the electron is attached, and it is called a **resonance**. A resonance has a signature in the integral cross section [8], and ideally it appears as a Lorentzian peak of the form

$$\sigma \sim \frac{(\Gamma/2)^2}{(E - E_{\text{res}})^2 + (\Gamma/2)^2}, \tag{2.1.36}$$

where E_{res} is the resonance energy, which is the most probable attachment energy, and Γ is the resonance width, which is also related to the resonance lifetime ($\tau \sim \frac{\hbar}{\Gamma}$) by the time-energy uncertainty relation. Typically, the lower the resonance energy is, the sharper will be its signature in the integral cross section, and the longer will be its lifetime. Commonly, the integral cross section presents a background, which may shift the resonance structure to higher energy, or even superimpose it. However, we limit this qualitative discussion to an ideal resonance model. Figure 2.2 presents an integral cross section for a model resonance.

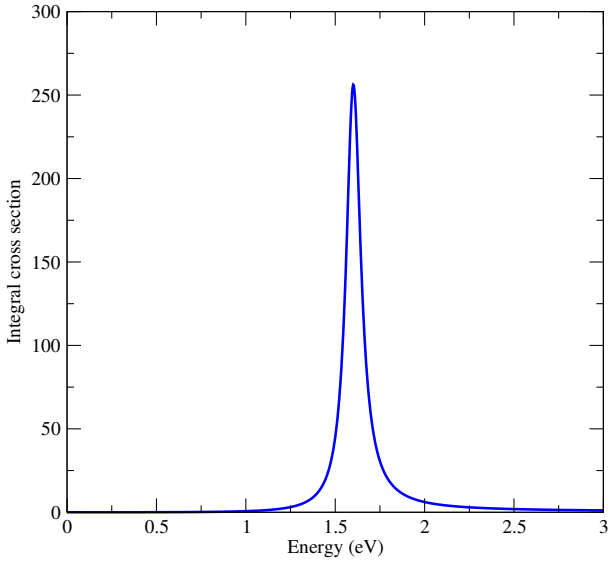

Figure 2.2: Integral cross section for a model resonance. The peak ideally Lorentzian is centred in 1.6 eV and has width of 0.2 eV.

From the molecular electronic structure perspective, a resonance occurs when the incident electron populates a vacant orbital in the target molecule. Qualitatively, it can also be understood from the temporary capture of the electron in a potential well. For illustrative purposes, let us consider a target interacting with an incident electron through a square potential well $U(r)$ with length a. The electron has an angular momentum l that produces a centrifugal barrier $l(l+1)/r^2$ which adds to $U(r)$, to produce the effective potential U_{eff}. Figure 2.3 presents an illustration of this model. If the electron energy is greater than the barrier, as E_1 in the figure, there is no electron attachment. However, when the energy is less than the barrier height, as E_2 in the same figure, the electron can

be trapped by tunneling across the barrier into the well. After a certain time, which can be understood as the resonance lifetime, the electron escapes by tunneling back out.

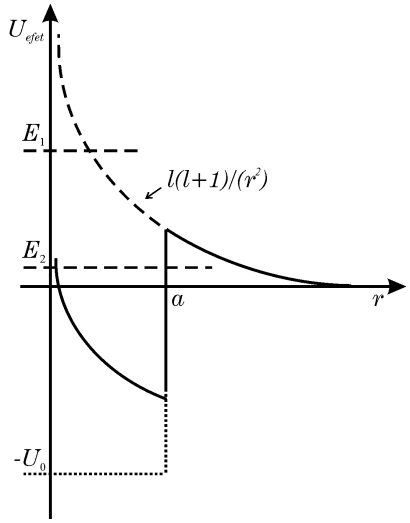

Figure 2.3: Illustration of the electron attachment. The square potential well adds to a centrifugal barrier, due to the electron angular momentum l, to produce the effective potential. E_1 represents a non-attachment process, whereas E_2 represents an energy lower then the barrier in U_{eff}, able to give rise to the electron attachment.

2.2 The Schwinger Multichannel Method

In the last section, we defined the basics of the electron scattering problem and presented the Lippmann-Schwinger equation. In this section we derive the **Schwinger Multichannel Method (SMC)**. It is a variational approach to the scattering amplitude based on the Lippmann-Schwinger equation. The method was originally designed to account for the electronic excitation channels in electron-molecule collisions, and can be viewed as an alternative derivation of the Schwinger Variational Principle suitable for numerical implementation.

The Schwinger Variational Principle (SVP) develops the scattering amplitude as a functional of the scattering states $\Psi_\Gamma^{(\pm)}$, and expands these states in a set of trial basis functions [29]. In the first step, the Lippmann-Schwinger equation (2.1.18) is multiplied by the potential V and rewritten as

$$A^{(\pm)}|\Psi_\Gamma^{(\pm)}\rangle = V|S_\Gamma\rangle, \tag{2.2.1}$$

where the $A^{(\pm)}$ operator is given by

$$A^{(\pm)} = V - VG_0^{(\pm)}V. \tag{2.2.2}$$

The scattering amplitude was formally defined above, in eq. (2.1.7). In fact, it can be formally defined from the two possible boundary conditions ($\pm$) [8], where the second is given by

$$f_{\Gamma',\Gamma} = -\frac{1}{2\pi}\langle\Psi_{\Gamma'}^{(-)}|V|S_\Gamma\rangle. \tag{2.2.3}$$

Using eq. (2.2.1) in (2.2.3), the scattering amplitude can also be written as

$$f_{\Gamma',\Gamma} = -\frac{1}{2\pi}\langle\Psi_{\Gamma'}^{(-)}|A^{(+)}|\Psi_\Gamma^{(+)}\rangle. \tag{2.2.4}$$

From the three expressions given in eqs. (2.1.7), (2.2.3) and (2.2.4), the scattering amplitude can be written in the following exact form,

$$[f_{\Gamma',\Gamma}] = -\frac{1}{2\pi}\left[\langle S_{\Gamma'}|V|\Psi_\Gamma^{(+)}\rangle + \langle\Psi_{\Gamma'}^{(-)}|V|S_\Gamma\rangle - \langle\Psi_{\Gamma'}^{(-)}|A^{(+)}|\Psi_\Gamma^{(+)}\rangle\right], \tag{2.2.5}$$

which is a functional of the scattering states. The functional above must be stable ($\delta[f] = 0$) under first-order variations,

$$\langle \Psi_{\Gamma'}^{(-)}| \to \langle \Psi_{\Gamma'}^{(-)}| + \langle \delta\Psi_{\Gamma'}^{(-)}| \tag{2.2.6}$$

and

$$|\Psi_{\Gamma}^{(+)}\rangle \to |\Psi_{\Gamma}^{(+)}\rangle + |\delta\Psi_{\Gamma}^{(+)}\rangle, \tag{2.2.7}$$

which results in the condition

$$A^{(+)\dagger} = A^{(-)}. \tag{2.2.8}$$

Let us now assume that the scattering state can be expanded in some arbitrary trial basis $|\chi_\mu\rangle$, such that

$$|\Psi^{(+)}\rangle = \sum_\mu a_\mu^{(+)} |\chi_\mu\rangle, \tag{2.2.9}$$

and

$$\langle \Psi^{(-)}| = \sum_\nu a_\nu^{*(-)} \langle \chi_\nu|. \tag{2.2.10}$$

To obtain the coefficients $a_\mu^{(+)}$ and $a_\nu^{(-)}$ we use the variational method,

$$\frac{\partial[f]}{\partial a_\mu^{(+)}} = \frac{\partial[f]}{\partial a_\nu^{*(+)}} = 0. \tag{2.2.11}$$

The analytical expressions for the variational coefficients $a_\mu^{(+)}$ and $a_\nu^{(-)}$ can be readily obtained. Substitution of these expressions back into eq. (2.2.5) leads to a representation of **the scattering amplitude in the trial basis**,

$$f(\boldsymbol{k}_{\Gamma'}, \boldsymbol{k}_\Gamma) = -\frac{1}{2\pi} \sum_{\mu,\nu} \langle S_{\Gamma'}|V|\chi_\mu\rangle (d^{-1})_{\mu\nu} \langle \chi_\nu|V|S_{\Gamma'}\rangle, \tag{2.2.12}$$

with

$$d_{\mu\nu} = \langle \chi_\mu | A^{(+)} | \chi_\nu \rangle. \tag{2.2.13}$$

At this point, we complete the Schwinger Variational Principle. It is important to emphasize some aspects of this expression:

- The asymptotic condition (2.1.5) is respected, even if the trial functions themselves do not comply. They are multiplied by the potential V, which goes to zero when the

$r_{N+1} \to \infty$ limit is taken, so the functions do not have to satisfy that condition. The Green's operator already carries such the boundary condition, independent of the behavior of those functions. Therefore, we can choose a square-integrable function set that facilitates the computation of the matrix elements.

- The integral over the target continuum states in the matrix elements $\langle \chi_\mu | V G_0^{(\pm)} V | \chi_\nu \rangle$ makes the calculation not feasible. The Green's operator carries the sum over the discrete target spectrum (electronic bound states) and integration over the continuum spectrum (ionization states). The inclusion of the whole spectrum is essential from the formal point of view, since the continuum states ensure the antisymmetry on the right-side of eq (2.1.18) [30]. However, the numerical description of the complete spectrum would obviously be impractical.

To make the SVP suitable for numerical implementation, we define a projection operator, which plays a central role in the SMC method as it defines the electronic channels Φ_l that will be included in the calculation [31]. The projection operator is given by

$$P \equiv \sum_{l}^{open} |\Phi_l(\boldsymbol{r}_1, ..., \boldsymbol{r}_{N+1})\rangle\langle\Phi_l(\boldsymbol{r}_1, ..., \boldsymbol{r}_{N+1})|, \tag{2.2.14}$$

and if we project the Lippmann-Schwinger equation on the P space,

$$P|\Psi_\Gamma^{(\pm)}\rangle = |S_\Gamma\rangle + G_P^{(\pm)} V |\Psi_\Gamma^{(\pm)}\rangle, \tag{2.2.15}$$

where $P|S_\Gamma\rangle = |S_\Gamma\rangle$ and $G_P^{(\pm)} = P G_0^{(\pm)}$. Following the same steps that lead to eq. (2.2.5), the SVP will be obtained with the operator $A^{(\pm)} = PV - V G_P^{(\pm)} V$. However, since $PV \neq VP$, the latter will not satisfy the variational stability condition in eq. (2.2.8).

The central point in the development of the SMC approach is obtaining the $A^{(\pm)}$ operator in a form that incorporates the projected Green's operator without violating the stability condition. To this end, the scattering Schrödinger equation can be written in the following form [31],

$$(E - H)[aP + (1 - aP)]|\Psi_\Gamma^{(+)}\rangle = 0, \tag{2.2.16}$$

which is exact for any value of the real arbitrary parameter a, as the $(1 - aP)$ term recovers the information on the closed channels projected out by aP. We obtain, after

some manipulation of eq. (2.2.16), the alternative form

$$A_P^{(\pm)}|\Psi_\Gamma^{(\pm)}\rangle = V|S_\Gamma\rangle, \tag{2.2.17}$$

with

$$A_P^{(\pm)} = \frac{1}{2}(PV + VP) - VG_P^{(\pm)}V + \frac{1}{a}\left[\hat{H} - \frac{a}{2}(\hat{H}P + P\hat{H})\right], \tag{2.2.18}$$

and $\hat{H} = E - H$. This expression is equivalent to the Lippmann-Schwinger equation multiplied by V, although now the $A^{(\pm)}$ operator conveniently incorporates the symmetrized potential $(PV + VP)$ and the projected Green's operator,

$$G_P^{(\pm)} = \lim_{\varepsilon\to 0}\sum_l^{open}\int d^3k \frac{|\Phi_l \boldsymbol{k}\rangle\langle\Phi_l \boldsymbol{k}|}{\frac{k_l^2}{2} - \frac{k^2}{2} \pm i\varepsilon}, \tag{2.2.19}$$

whithout the continuum eigenstates of the molecule.

Let us now consider the representation of the $A_P^{(\pm)}$ operator in the trial basis, as proposed in eq. (2.2.10). The variational stability condition, eq. (2.2.8), will be immediately satisfied for the $\langle\chi_\nu|(PV + VP)|\chi_\mu\rangle$ matrix elements, since the interaction operator has been properly symmetrized. Likewise, since the Green's operator satisfies $G_0^{\dagger(+)} = G_0^{(-)}$ [8], it may be easily realized that the $\langle\chi_\nu|(VG_P^{(\pm)}V)|\chi_\mu\rangle$ matrix elements are also compatible with the stability condition. The third term on the right-hand side of eq. (2.2.18) would be a little more complicated because $\hat{H}$ contains the T_{N+1} kinetic energy operator that would give rise to surface terms in the continuum-continuum matrix elements. Recalling that eqs. (2.2.16) to (2.2.18) are exact for any value of the arbitrary parameter, it is possible to verify that $a = (N+1)$ zeroes out the contribution from the continuum-continuum matrix elements, such that a working expression for the SMC scattering amplitude is given by eqs. (2.2.12) and (2.2.18), with $a = (N+1)$.

2.2.1 Computational aspects

We discussed the construction of the SMC method, starting from the SVP to the projection operator which restricts the open channels to discrete electronic states of the target. The final expression for the scattering amplitude in this approximation,

$$f(\boldsymbol{k}_{\Gamma'}, \boldsymbol{k}_{\Gamma}) = -\frac{1}{2\pi} \sum_{\mu,\nu} \langle S_{\Gamma'}|V|\chi_\mu\rangle (d^{-1})_{\mu\nu} \langle \chi_\nu|V|S_{\Gamma'}\rangle, \tag{2.2.20}$$

with

$$d_{\mu\nu} = \langle \chi_\mu | A_P^{(+)} | \chi_\nu \rangle, \tag{2.2.21}$$

is the same as eq. (2.2.12), but the operator $A_P^{(+)}$ is given by

$$A_P^{(\pm)} = \frac{1}{2}(PV + VP) - VG_P^{(\pm)}V + \frac{1}{N+1}\left[\hat{H} - \frac{N+1}{2}(\hat{H}P + P\hat{H})\right]. \tag{2.2.22}$$

In what follows, we discuss the computational details to evaluate the scattering amplitude in terms of the $|\chi_\nu\rangle$ and the $\langle \chi_\mu | A_P^{(+)} | \chi_\nu \rangle$ matrix elements.

Elastic channel and ground state at the Hartree-Fock level

The electron scattering problem proposed in this work consists in the characterization of the metastable anionic states of halocamphor molecules. The low-lying anionic states are produced with incident electrons with energies lower than 3 eV, which may be below the electronic excitation threshold of the target molecules. Therefore, **only the elastic channel is relevant**, and the projection operator we may consider is given by $P = |\Phi_0\rangle\langle\Phi_0|$. We emphasize that we are not considering vibrational excitations in this argument, but only the electronic excitations.

In principle, we would be inclined to use highly sophisticated methods to describe the ground state of the target. However, care must be taken to compromise accuracy with numerical effort, as the scattering states are more computationally demanding than bound states. An accurate calculation thus requires a balanced description of electronic correlation in the $(N+1)$- and in the N-electron states. In the case when a high-level method is employed to describe the isolated target, a similar description might not be possible for the scattering state, due to computational limitations. As a result, the energy of the anion states would be overestimated, as well as their widths. Otherwise, these resonance parameters would likewise be underestimated in the case when the anion state was overcorrelated with respect to the target state. In this sense, it is convenient to describe the target molecule at the Hartree-Fock (HF) level, in view of its low cost.

Configuration states functions for the static-exchange and static-exchange plus polarization approximations

Configuration state function (CSF) is a spin-adapted linear combination of Slater determinants. CSFs are employed as trial basis functions (χ_μ) that the scattering wave function is expanded. Concerning the description of the anion state, the CSFs represent the possible electronic occupations in the anion states. A first approximation to the scattering state is given by

$$|\chi_\mu\rangle = \mathcal{A}|\Phi_0\rangle|\phi_\mu\rangle, \tag{2.2.23}$$

where the operator $\mathcal{A}$ imposes the antisymmetrization among the $(N+1)$ electrons and $|\phi_\mu\rangle$ is a scattering orbital.

We refer to eq. (2.2.23) as **the static-exchange (SE) approximation**, since the target is frozen in the ground state, implying no dynamical response to the incident electron. To improve the description of the scattering state, we take into account virtual excitations of the target by promoting a single electron from a hole orbital to a particle orbital. Denoting this singly-excited virtual state by Φ_j, we obtain a second approximation called **the static-exchange plus polarization** (SEP) approximation,

$$|\chi_\mu\rangle = \mathcal{A}|\Phi_j\rangle|\phi_\mu\rangle. \tag{2.2.24}$$

As discussed above, a balanced description among the anionic states and the target molecule is desired. Once the CSFs in the SEP approximation include dynamic correlation effects in the scattering calculation, it stabilizes the anionic states energies. On the other hand, the target is described in the Hartree-Fock level, therefore the difference between anionic state energies and the neutral ground state energy can be underestimated if the number of configurations is excessively large [32]. The CSF space is obtained from the energy criterion proposed by Kossoski and Bettega [33]. The target excitations with the singlet and triplet spin coupling were chosen according to $\Delta \geq \epsilon_{part} - \epsilon_{hole} + \epsilon_{scat}$, where ϵ_{scat}, ϵ_{part}, and ϵ_{hole} are the energies of the scattering, particle, and hole orbitals, respectively, and Δ is an energy threshold.

We applyed the HF orbitals obtained from the target description as hole, particle and scattering orbitals. The last two are modified virtual orbitals, which are generated from

a cation electric field for the same target molecule [34]. These orbitals are concentrated in a limited region of the molecule, and improve the convergence of the scattering state in the CFS expansion.

Matrix elements computation

The SMC method allows us to employ square-integrable functions, as discussed above. Even though the scattering orbitals would be more diffuse than those representing the bound electrons, they do not necessarily need to include continuum states. In practice, the bound and scattering orbitals are obtained from the HF calculation, being both expanded in Cartesian Gaussian basis sets, since these are often employed in electronic structure calculations.

The matrix elements of the projected Green's operator are computationally demanding. Formally, $\langle\chi_\nu|VG_p^{(+)}V|\chi_\mu\rangle$ can be evaluated by employing the residue theorem, to obtain

$$G_P^{(+)} = G_P^{Pr} + G_P^R, \tag{2.2.25}$$

with G_P^{Pr} the Cauchy principal value,

$$G_P^{Pr} = \mathrm{P}\int_0^\infty dk' \frac{k'^2}{\frac{k^2}{2} - \frac{k'^2}{2}} \int d\hat{\boldsymbol{k}}' |\Phi_0 \boldsymbol{k'}\rangle\langle\Phi_0 \boldsymbol{k'}|, \tag{2.2.26}$$

and G_P^R the residue of $G_P^{(+)}$,

$$G_P^R = i\pi k \int d\hat{\boldsymbol{k}} |\Phi_0 \boldsymbol{k}\rangle\langle\Phi_0 \boldsymbol{k}|. \tag{2.2.27}$$

As a result, the matrix element can be separated into a real part and an imaginary part,

$$\langle\chi_\mu|VG_P^{(+)}V|\chi_\nu\rangle = \langle\chi_\mu|VG_P^{Pr}V|\chi_\nu\rangle + \langle\chi_\mu|VG_P^RV|\chi_\nu\rangle. \tag{2.2.28}$$

The first term on the right-hand side of eq. (2.2.28), which is **off-the-energy-shell**, is given by

$$\langle\chi_\mu|VG_P^{Pr}V|\chi_\nu\rangle = \mathrm{P}\int_0^\infty dk' \frac{k'^2}{\frac{k^2}{2}-\frac{k'^2}{2}} g_{\mu\nu}(k'), \tag{2.2.29}$$

with

$$g_{\mu\nu}(k) = \int d\hat{\boldsymbol{k}}\langle\chi_\mu|\Phi_0\boldsymbol{k}\rangle\langle\Phi_0\boldsymbol{k}|\chi_\nu\rangle, \tag{2.2.30}$$

and can be evaluated by the Gauss-Legendre or Gauss-Laguerre numerical methods. The radial k-space is discretized on the quadrature points $\{k_j\}$, where the $g_{\mu\nu}(k_j)$ matrix elements are calculated, and angular quadrature points $\{\hat{\boldsymbol{k}}_i\}$ are also employed to obtain $g_{\mu\nu}$, according to eq. (2.2.30). In general, for each quadrature point in the radial k-space we perform angular integrations (2.2.30) typically with 2048 points. Considering 64 points in the radial quadrature, also a typical choise, we have more than 130,000 quadrature points for each matrix element, which is clearly computationally demanding.

The second term on the right-hand side of eq. (2.2.28) is **on-the-energy-shell** and is given by

$$\langle\chi_\mu|VG_P^{R}V|\chi_\nu\rangle = i\pi k g_{\mu\nu}(k), \tag{2.2.31}$$

which depends on the momentum of the incident electron k, and is evaluated by Gauss-Legendre or Lebedev-Laikov numerical methods.

Apart from the Green's operator matrix elements, all integrals in the denominator of eq. (2.2.13) can be computed with standard quantum chemistry techniques. The numerator involves the matrix elements $\langle\Phi_0\boldsymbol{k}|V|\chi_\mu\rangle$ that can be reduced to one- and two-electron integrals involving Cartesian Gaussian functions and plane waves. The two-electron integrals are given by

$$(\alpha\beta|\gamma\boldsymbol{k}) = \int d\boldsymbol{r}_1 \int d\boldsymbol{r}_2 \alpha(\boldsymbol{r}_1)\beta(\boldsymbol{r}_1)\frac{1}{|\boldsymbol{r}_1-\boldsymbol{r}_2|}\gamma(\boldsymbol{r}_2)e^{i\boldsymbol{k}\cdot\boldsymbol{r}_1}, \tag{2.2.32}$$

where α, β and γ denote Cartesian Gaussian functions. The computational effort scales as $\sim N_\alpha^3$, where N_α is the dimension of the basis, and should be calculated for every incident ($\boldsymbol{k}_i$) and outgoing ($\boldsymbol{k}_f$) wave vector.

Use of pseudopotentials

To reduce the computational effort required by these and other integrals, the use of the analytical norm-conserving pseudopotentials of Bachelet, Hamann and Schlüter [35] in the SMC framework was proposed [36]. In this version of the SMCPP method, the nuclei and core electrons are replaced by the pseudopotentials, such that only the valence electrons are explicitly described. This may lead to a significant reduction of the numerical effort, especially if heavy atoms are present, for instance in the halogenated species. The efficient use of pseudopotentials in the SMCPP framework requires the optimization of Gaussian basis sets, following the procedure of Bettega *et al.* [36]. Even if pseudopotentials are employed, the description of polarization effects, according to eq. (2.2.24), can make the computations very demanding. The SMCPP method allows for efficient parallelization codes based on OpenMP directives [37].

2.3 The spin-dependent electron scattering theory

We present in this section a review of the spin-dependent electron scattering theory formulated by Blum and Thompson [17]. The theory incorporates the transition matrix generalized in terms of Pauli matrices and the construction of its components under symmetry operators. The spin-dependent scattering amplitude is derived from these terms, which results in a scattering asymmetry when the molecular target chiral states are considered.

2.3.1 The spin scattering matrix M

Let us consider the T-matrix as expressed in eq. (2.1.19). For a generalized expression, the transition from a state $|\Psi_\Gamma; m_0\rangle$ with initial spin m_0 to a states $|\Psi_{\Gamma'}; m_1\rangle$ with final spin m_1 is expressed by

$$\langle \Psi_\Gamma; m_0 | T | \Psi_{\Gamma'}; m_1 \rangle. \tag{2.3.1}$$

We will treat explicitly the spin-dependence in the scattering problem, then it is convenient to express the matrix element only in terms of the spin m_0 and m_1. Therefore, we define an operator M in the spin space[1] by the condition that its matrix elements give the corresponding amplitude

$$\langle m_1 | M | m_0 \rangle = f(m_1, m_0). \tag{2.3.2}$$

We are going to derive an expression for M for **elastic forward scattering from spinless molecules, which in our problems are all closed shell**. The total system is composed of the target molecule and the incident electron, hence its total spin is $1/2$. Once the operator lies in the spin space, we can expand M in terms of the 2×2 Pauli matrices $\boldsymbol{\sigma} = (\sigma_x, \sigma_y, \sigma_z)$. The spin scattering matrix is usually assumed to depend linearly on the Pauli matrices [17],

$$M = g_0 \mathbb{1} + \boldsymbol{u} \cdot \boldsymbol{\sigma}, \tag{2.3.3}$$

where g_0 is the spinless transition matrix element, $\mathbb{1}$ is the identity matrix in the spin

[1] The M operator is the transition matrix for the spin-dependent problem, that acts *only* on the spin states.

state and $\boldsymbol{u}$ is the vector to be determined.

In order to proceed we use symmetry arguments. The electron-molecule interaction is invariant under rotations, spatial inversion and time reversal of the system, where we neglect the small parity violating terms due to weak neutral currents[2]. It follows that M must transform as a **proper scalar operator**, i.e, it must be invariant under the three operations mentioned above.

From the well-known symmetry properties of the Pauli matrices [17] (see Tab. 2.1), the invariance of the M matrix requires that $\boldsymbol{u}$ transforms according to:

- (i) $\boldsymbol{u}$ should be even under space inversion,
- (ii) $\boldsymbol{u}$ must be odd under time reversal.

We can construct an expression for $\boldsymbol{u}$, without loss of generality, by defining the unit vectors $\hat{\boldsymbol{e}}_1, \hat{\boldsymbol{e}}_2, \hat{\boldsymbol{e}}_3$, which form an orthogonal coordinate system in the molecular frame, and the wave vector $\boldsymbol{k}$ of the incident electron ($\boldsymbol{k} \equiv \boldsymbol{k_i}$).

Table 2.1: Transformation properties of the relevant vectors. The plus (minus) sign denotes even (odd) behaviour of the vectors under a given operation.

	Space inversion	Time reversal
$\boldsymbol{k}$	$-$	$-$
$\boldsymbol{\sigma}$	$+$	$-$
$\hat{\boldsymbol{e}}_i$	$-$	$+$
$\boldsymbol{k} \times \hat{\boldsymbol{e}}_i$	$+$	$-$

Using the transformation properties shown in Table 2.1, it follows that the three vectors $\boldsymbol{k} \times \hat{\boldsymbol{e}}_i$ have the required symmetry properties (i) and (ii). These vectors lie in the plane orthogonal to $\boldsymbol{k}$, therefore it is necessary to include one more vectors to construct a linearly independent set to using as a basis set for $\boldsymbol{u}$. This additional vector must, of course, satisfy the properties (i) and (ii). A choice that satisfies these properties is the product of the pseudoscalar $((\hat{\boldsymbol{e}}_1 \times \hat{\boldsymbol{e}}_2) \cdot \hat{\boldsymbol{e}}_3)$ with $\boldsymbol{k}$ [17]. Then, we can express $\boldsymbol{u}$ by the following form:

$$\boldsymbol{u} = \sum_{i=1}^{3} g_i(\boldsymbol{k} \times \hat{\boldsymbol{e}}_i) + g_4((\hat{\boldsymbol{e}}_1 \times \hat{\boldsymbol{e}}_2) \cdot \hat{\boldsymbol{e}}_3)\boldsymbol{k}. \tag{2.3.4}$$

[2]Weak neutral current are subatomic particles interactions by means of the weak force, which is the only fundamental interaction that breaks parity-symmetry [26].

Substitution of (2.3.4) into (2.3.3) yields a general expression for the spin scattering matrix M:

$$M = g_0\mathbb{1} + \sum_{i=1}^{3} g_i(\boldsymbol{k} \times \hat{\boldsymbol{e}}_i)\cdot\boldsymbol{\sigma} + g_4((\hat{\boldsymbol{e}}_1 \times \hat{\boldsymbol{e}}_2)\cdot\hat{\boldsymbol{e}}_3)\boldsymbol{k}\cdot\boldsymbol{\sigma}, \tag{2.3.5}$$

where the parameters $g_i = g_i(\hat{\boldsymbol{e}}_1, \hat{\boldsymbol{e}}_2, \hat{\boldsymbol{e}}_3, \boldsymbol{k})$ are required to transform as proper scalars and are functions of any proper scalar which can be constructed from the set $\{\hat{\boldsymbol{e}}_i\}$ and $\boldsymbol{k}$. All information on the scattering is contained in the functions g_0, g_1, g_2, g_3 and g_4.

For a chiral molecule, **the pseudoscalar term** $((\hat{\boldsymbol{e}}_1 \times \hat{\boldsymbol{e}}_2)\cdot\hat{\boldsymbol{e}}_3)$ **defines which enantiomer the target is**. As an illustrative example, let us consider a "model molecule" of the type AH_3, shown in Fig. 2.4, which will have a chiral structure if all bond lengths are different. The chirality is defined by the left-handed (anticlockwise) or right-handed (clockwise) sequence of the groups H_1A and H_2A when viewed in the direction of H_3A. The sequence defines an axial vector $\hat{\boldsymbol{e}}_1 \times \hat{\boldsymbol{e}}_2$ and when multiplied with the vector $\hat{\boldsymbol{e}}_3$, gives the scalar triple product $((\hat{\boldsymbol{e}}_1 \times \hat{\boldsymbol{e}}_2) \cdot \hat{\boldsymbol{e}}_3)$. The inversion operation defined by $(\hat{\boldsymbol{e}}_1, \hat{\boldsymbol{e}}_2, \hat{\boldsymbol{e}}_3) \to (-\hat{\boldsymbol{e}}_1, -\hat{\boldsymbol{e}}_2, -\hat{\boldsymbol{e}}_3)$ transforms a right-handed system into a left-handed one. As a consequence, the triple product changes sign under parity transformations.

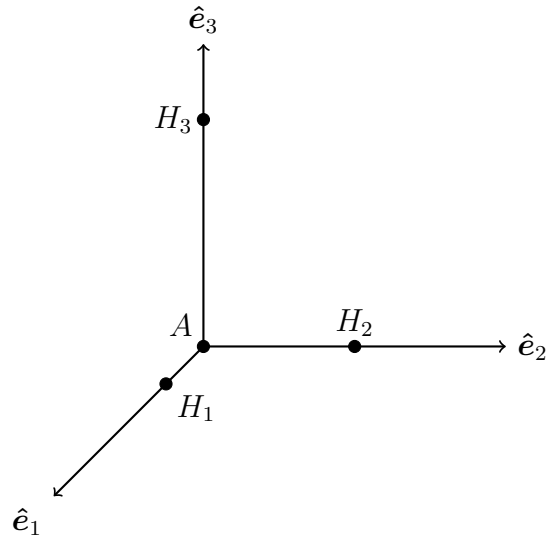

Figure 2.4: Model molecule for the illustration.

We note that (2.3.4) and (2.3.5) are overdetermined. The three vectors $\boldsymbol{k} \times \hat{\boldsymbol{e}}_i$ are contained in the plane perpendicular to $\boldsymbol{k}$. Once two linearly independent vectors are sufficient to span this plane, one of the three terms g_i $(i = 1, 2, 3)$ can therefore always be eliminated. It follows that M is **completely determined by four independent**

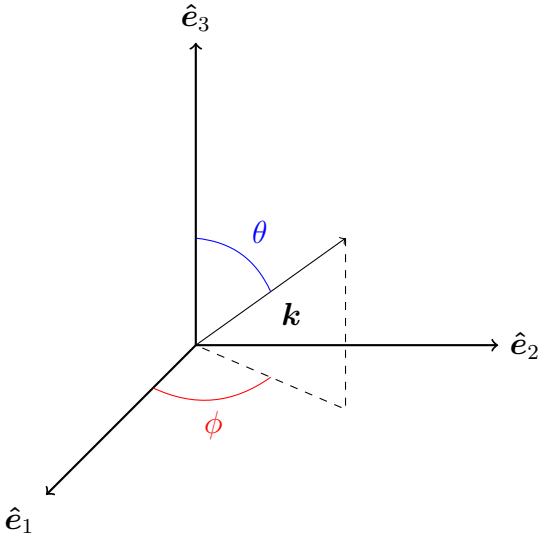

Figure 2.5: The vector $\boldsymbol{k}$ projected in the molecular frame.

parameters for any value of $\boldsymbol{k}$ and any orientation of the molecule. For a reduced expression of eq. (2.3.5), we consider the projection of $\boldsymbol{k}$ onto the coordinates $\hat{\boldsymbol{e}}_{\boldsymbol{i}}$. We denote the azimuth angle between $\boldsymbol{k}$ and $\hat{\boldsymbol{e}}_3$ by θ and the polar angle between $\hat{\boldsymbol{e}}_1$ and the projection of $\boldsymbol{k}$ into the $\hat{\boldsymbol{e}}_2$-$\hat{\boldsymbol{e}}_3$ plane by ϕ, as shown in Fig. 2.5. The decomposition of $\boldsymbol{k}$ can be written in the form

$$\boldsymbol{k} = \hat{\boldsymbol{e}}_1 \sin\theta\cos\phi + \hat{\boldsymbol{e}}_2 \sin\theta\sin\phi + \hat{\boldsymbol{e}}_3 \cos\theta. \tag{2.3.6}$$

For the vector $\boldsymbol{k} \times \hat{\boldsymbol{e}}_3$, we obtain, after some algebra,

$$\boldsymbol{k} \times \hat{\boldsymbol{e}}_3 = -(\boldsymbol{k} \times \hat{\boldsymbol{e}}_1)\tan\theta\cos\phi - (\boldsymbol{k} \times \hat{\boldsymbol{e}}_2)\tan\theta\sin\phi, \tag{2.3.7}$$

for $\theta \neq 90^0$, that is, if $\boldsymbol{k}$ is not contained in the $\hat{\boldsymbol{e}}_2$-$\hat{\boldsymbol{e}}_3$ plane. We insert (2.3.7) in (2.3.5) and obtain

$$M = g_0\mathbb{1} + g_1'(\boldsymbol{k} \times \hat{\boldsymbol{e}}_1)\cdot\boldsymbol{\sigma} + g_2'(\boldsymbol{k} \times \hat{\boldsymbol{e}}_2)\cdot\boldsymbol{\sigma} + g_4((\hat{\boldsymbol{e}}_1 \times \hat{\boldsymbol{e}}_2)\cdot\hat{\boldsymbol{e}}_3)\boldsymbol{k}\cdot\boldsymbol{\sigma}, \tag{2.3.8}$$

with

$$g_1' = g_1 - g_3\tan\theta\cos\phi \qquad g_2' = g_2 - g_3\tan\theta\sin\phi. \tag{2.3.9}$$

A similar expression can also be obtained if $\boldsymbol{k}$ is contained in the $\hat{\boldsymbol{e}}_1$-$\hat{\boldsymbol{e}}_2$ plane. However, in general discussions it is more convenient to use (2.3.5) [17].

Summarizing, the scattering operator M expressed in eq. (2.3.5) can be used to

describe spin-dependent effects in elastic forward scattering of electrons from oriented spinless molecules. The functions g_i must contain all the information on the scattering process, which underlie the asymmetries observed in the experiments [6, 1, 12].

2.3.2 Relation to scattering amplitudes

We have discussed that, in general, the spin scattering matrix M is characterized by four parameters g_i. This number is related to the number of possible spin-dependent processes, two non-flip ones with $\pm\frac{1}{2} \to \pm\frac{1}{2}$ and two spin-flip processes $\pm\frac{1}{2} \to \mp\frac{1}{2}$. The corresponding four scattering amplitudes $f(m_1, m_0)$ are related to M by eq. (2.3.2). For a specific target orientation, we can discuss which terms of M correspond to these processes. If we choose the direction of $\boldsymbol{k}$ as the z axis of a laboratory frame, we have $\boldsymbol{k}\cdot\boldsymbol{\sigma} \sim \sigma_z$, and we define the $\boldsymbol{k}$ direction as the quantization axis of the spin operator. The terms $g_i(\boldsymbol{k} \times \hat{\boldsymbol{e}}_i)\cdot\boldsymbol{\sigma}$ are combinations of σ_x and σ_y. We can obtain the spin-preserving scattering amplitudes

$$f(\pm, \pm) = \langle \pm | M | \pm \rangle, \tag{2.3.10}$$

where $+(-)$ denotes spin up (down).

In eq. (2.3.5), the first term accounts for spin-preserving scattering because it pertains to spinless scattering ($g_0\mathbb{1}$ is diagonal in the spin space). The second term, which concerns $g_i(\boldsymbol{k} \times \hat{\boldsymbol{e}}_i)\cdot\boldsymbol{\sigma}$, vanishes because the matrix elements are non-diagonal in the spin space. The last term, $g_4((\hat{\boldsymbol{e}}_1 \times \hat{\boldsymbol{e}}_2) \cdot \hat{\boldsymbol{e}}_3)\boldsymbol{k}\cdot\boldsymbol{\sigma}$ is diagonal in the σ_z space representation, with eigenvalues $\pm$ for the $|\pm\rangle$ eigenstates. We have, therefore,

$$f(+, +) = g_0 + g_4((\hat{\boldsymbol{e}}_1 \times \hat{\boldsymbol{e}}_2) \cdot \hat{\boldsymbol{e}}_3) \tag{2.3.11}$$

and

$$f(-, -) = g_0 - g_4((\hat{\boldsymbol{e}}_1 \times \hat{\boldsymbol{e}}_2) \cdot \hat{\boldsymbol{e}}_3). \tag{2.3.12}$$

The spin-flip amplitudes are related to g_1, g_2 and g_3. We can derive the corresponding relation for the case of the model molecule introduced above, and illustrated in Fig. 2.4. Assuming that $\boldsymbol{k}$ is parallel to $\hat{\boldsymbol{e}}_3$, we obtain from (2.3.5):

$$f(+, -) = -ig_1 - g_2 \tag{2.3.13}$$

and

$$f(-,+) = ig_1 - g_2, \tag{2.3.14}$$

since the vector product $\boldsymbol{k} \times \hat{\boldsymbol{e}}_3$ vanishes, and by using $\sigma_x = \frac{1}{2}(\sigma_+ + \sigma_-)$ and $\sigma_y = \frac{1}{2i}(\sigma_+ - \sigma_-)$.

Scattering from chiral molecules

Equations (2.3.11), (2.3.12), (2.3.13) and (2.3.14) show that electrons with spin up and spin down are scattered with different amplitudes if g_4 is different from zero. To define $\boldsymbol{k}$ parallel to z axis in the laboratory frame, electrons with spin projection parallel or antiparallel to $\boldsymbol{k}$ have a definite handedness. The right-handed character derives from the relation $\boldsymbol{k}\cdot\boldsymbol{\sigma} > 0$, while the left-handed character is given by the antiparallel relation $\boldsymbol{k}\cdot\boldsymbol{\sigma} < 0$. In order for both handednesses of electrons to be scattered with different amplitudes, the molecules must be able to distinguish between electrons with different spin projections.

Let us assume that (2.3.5) gives the M matrix for a give enantiomer. We can derive the corresponding matrix $M^{(oppos)}$ for the other enantiomer. The application of the space inversion operator to an asymmetric molecule transforms it into its mirror-image isomer. Under this operation, the basis vectors $\hat{\boldsymbol{e}}_i$ reverse their sign, $\hat{\boldsymbol{e}}_i \to -\hat{\boldsymbol{e}}_i$, and, correspondingly

$$g_i(\hat{\boldsymbol{e}}_1, \hat{\boldsymbol{e}}_2, \hat{\boldsymbol{e}}_3, \boldsymbol{k}) \to g_i^{(oppos)} = g_i(-\hat{\boldsymbol{e}}_1, -\hat{\boldsymbol{e}}_2, -\hat{\boldsymbol{e}}_3, \boldsymbol{k}), \tag{2.3.15}$$

for $i = 1, \ldots, 4$[3]. The isomer is described in terms of the left-handed frame $(-\hat{\boldsymbol{e}}_1, -\hat{\boldsymbol{e}}_2, -\hat{\boldsymbol{e}}_3)$ and the corresponding M matrix is obtained from equation (2.3.5) by the transformation $\hat{\boldsymbol{e}}_i \to -\hat{\boldsymbol{e}}_i$ and $g_i \to g_i^{(oppos)}$. We also can obtain the set $g_i^{(oppos)}$ in terms of g_i by space inversion followed by time reversal operation on the scattering system (see Tab. 2.1), such that the combined operation preserves the direction of $\boldsymbol{k}$ but reverses the sign of the vectors $\hat{\boldsymbol{e}}_i$. Since the functions g_i are proper scalar functions with regard to transformations of the total system, they must remain invariant under the combined operation discussed. That is, we have the condition

[3]Note that this transformation acts on the coordinate system, only

$$g_i(\hat{\boldsymbol{e}}_1, \hat{\boldsymbol{e}}_2, \hat{\boldsymbol{e}}_3, \boldsymbol{k}) = g_i(-\hat{\boldsymbol{e}}_1, -\hat{\boldsymbol{e}}_2, -\hat{\boldsymbol{e}}_3, \boldsymbol{k}). \tag{2.3.16}$$

We conclude that electron scattering from chiral molecules is therefore characterized by the same set of functions g_i, and the corresponding spin scattering matrix $M^{(oppos)}$ can be written in the form

$$M^{(oppos)} = g_0 \mathbb{1} - \sum_{i=1}^{3} g_i(\boldsymbol{k} \times \hat{\boldsymbol{e}}_i) \cdot \boldsymbol{\sigma} - g_4((\hat{\boldsymbol{e}}_1 \times \hat{\boldsymbol{e}}_2) \cdot \hat{\boldsymbol{e}}_3)\boldsymbol{k} \cdot \boldsymbol{\sigma} \,. \tag{2.3.17}$$

In practice, the difference between M and $M^{(oppos)}$ is obtained only for a chiral target, because chiral states are not eigenstates of space inversion. The operator applied to the total system implies the substitution of a given enantiomer for the opposite one. For a non-chiral target molecule, their states are parity eigenstates. In this case, the space inversion operator applied to the system results in the same target molecule, but with an inverse coordinate system. In this case, it requires that $M = M^{(oppos)}$ and g_i must be zero.

The probability of transmission by chiral molecules for right- and left-handed projectiles is proportional to the expressions

$$|f(+,+)|^2 = |g_0 + g_4|^2 \tag{2.3.18}$$

and

$$|f(-,-)|^2 = |g_0 - g_4|^2, \tag{2.3.19}$$

respectively, as follows from (2.3.11) and (2.3.12) for molecules with $((\hat{\boldsymbol{e}}_1 \times \hat{\boldsymbol{e}}_2) \cdot \hat{\boldsymbol{e}}_3) = 1$. If we assume that $\mathrm{Re}(g_0 g_4^*) > 0$, we have that the right-handed electrons are predominantly scattered ($|f(+,+)| > |f(-,-)|$). For collisions with the other enantiomer ($(\hat{\boldsymbol{e}}_1 \times \hat{\boldsymbol{e}}_2) \cdot \hat{\boldsymbol{e}}_3) = -1$, it follows from (2.3.11) and (2.3.12) that left-handed electrons have a larger transmission probability:

$$|f(+,+)|^2 = |g_0 - g_4|^2 \tag{2.3.20}$$

and

$$|f(-,-)|^2 = |g_0 + g_4|^2. \tag{2.3.21}$$

If $\mathrm{Re}(g_0 g_4^*) < 0$ then the opposite results hold. In any case, **the chiral molecules act as spin filters**.

We might also say that the molecular pseudoscalar $((\hat{\boldsymbol{e}}_1 \times \hat{\boldsymbol{e}}_2) \cdot \hat{\boldsymbol{e}}_3)$ imposes a preferred relation between the momentum $\boldsymbol{k}$ and the axial spin vector $\boldsymbol{\sigma}$ of the incident electron: if under a given molecular transformation, the quantity $((\hat{\boldsymbol{e}}_1 \times \hat{\boldsymbol{e}}_2) \cdot \hat{\boldsymbol{e}}_3)$ changes sign, the pseudoscalar $\boldsymbol{k}\cdot\boldsymbol{\sigma}$, characterizing the helicity of the electron, changes its sign too. It implies that scattering of an electron with a given handedness by an enantiomer is preferred over the other electron handedness, and also the other enantiomer, which will generally gives rise to a transmission asymmetry. It can also be useful, with help of (2.3.11) and (2.3.12), to express g_4 by the relation

$$g_4 = \frac{1}{2}[f(+,+) - f(+,+)^{(oppos)}], \tag{2.3.22}$$

which implies that g_4 can be considered as a measure of the amount by which longitudinally polarized electrons can distinguish between the two enantiomers.

2.3.3 Spin polarization of the scattered electrons

We now consider the spin polarization of electrons scattered from an ensemble of unoriented chiral molecules. Let us consider the **forward scattering of an initially unpolarized electron beam**. The spin polarization $\boldsymbol{P}$ of the scattered electrons is given by the trace [17]

$$I\boldsymbol{P} = \frac{1}{2} Tr[MM^\dagger \boldsymbol{\sigma}], \tag{2.3.23}$$

with I being the unpolarized differential cross section. It is convenient to consider the two relations

$$\begin{gathered}(\boldsymbol{\sigma}\cdot\boldsymbol{A})(\boldsymbol{\sigma}\cdot\boldsymbol{B}) = \boldsymbol{A}\cdot\boldsymbol{B} + i\boldsymbol{\sigma}(\boldsymbol{A}\times\boldsymbol{B}) \\ \text{and} \\ Tr[(\boldsymbol{A}\cdot\boldsymbol{\sigma})\,\boldsymbol{\sigma}] = 2\boldsymbol{A},\end{gathered} \tag{2.3.24}$$

where $\boldsymbol{A}$ and $\boldsymbol{B}$ are two arbitrary vectors. Using (2.3.5) in (2.3.23) and applying (2.3.24) yields, after some algebra, a general expression for the spin polarization vector

$$I\boldsymbol{P} = \sum_{i=1}^{3}(g_0 g_i^* + g_0^* g_i)(\boldsymbol{k}\times\hat{\boldsymbol{e}}_i) + i\sum_{i=1}^{3}(g_4 g_i^* - g_4^* g_i)[(\hat{\boldsymbol{e}}_1\times\hat{\boldsymbol{e}}_2)\cdot\hat{\boldsymbol{e}}_3][\boldsymbol{k}\times(\boldsymbol{k}\times\hat{\boldsymbol{e}}_i)]$$
$$+ (g_0 g_4^* + g_0^* g_4)[(\hat{\boldsymbol{e}}_1\times\hat{\boldsymbol{e}}_2)\cdot\hat{\boldsymbol{e}}_3]\boldsymbol{k} + i\sum_{\substack{i=j=1\\ i>j}}^{3}(g_1 g_j^* - g_i^* g_j)[(\hat{\boldsymbol{e}}_i\times\hat{\boldsymbol{e}}_j)\cdot\boldsymbol{k}]\boldsymbol{k}. \tag{2.3.25}$$

The expression above contains the spin polarization for the forward transmitted electron beam, in terms of the four terms g_i, $i = 1,\ldots,4$. The total transverse polarization is given by the first two sums of (2.3.25). The terms $\sim \boldsymbol{k}\times\hat{\boldsymbol{e}}_i$ contain a contribution of transverse polarization, since they are orthogonal to $\boldsymbol{k}$. Also, they are independent of g_4 and, recalling our discussions in subsection 2.3.2, these components are produced by spin-flip processes only. The terms $\sim \boldsymbol{k}\times(\boldsymbol{k}\times\hat{\boldsymbol{e}}_i)$ lie in the $\boldsymbol{k}$-$\hat{\boldsymbol{e}}_i$ plane, therefore they also carry a contribution of transverse polarization.

The third and fourth terms in (2.3.25) account for the longitudinal polarization component $\boldsymbol{P}_{\parallel}$, since they have a contribution parallel to $\boldsymbol{k}$. The third term depends on g_0 and g_4 and can only be produced by non-flip processes, which implies that left- and right-handed electrons must be scattered differently. On the other hand, the terms $\sim g_1 g_j^* - g_i^* g_j$ contain the contributions of the spin-flip processes to $\boldsymbol{P}_{\parallel}$.

Finally, we consider the forward scattering of an initially spin unpolarized electron beam by **an ensemble of unoriented molecules**. Firstly, we note that the total system of incident electrons and unoriented molecules is axially symmetric with respect to $\boldsymbol{k}$. Consequently, no transverse polarization can be obtained, and the first two terms of (2.3.25) must vanish after an average over all molecular orientations.

Secondly, when we consider the collisions with chiral molecules, we can conclude that no spin-flip processes can contribute to $\boldsymbol{P}_{\parallel}$. For a given orientation of a molecular subensemble with $(\hat{\boldsymbol{e}}_i\times\hat{\boldsymbol{e}}_j)\cdot\boldsymbol{k} > 0$, we can always find contributions from molecules where $(\hat{\boldsymbol{e}}_i\times\hat{\boldsymbol{e}}_j)\cdot\boldsymbol{k}$ cancels out the first contribution. This can be obtained by rotating the molecular subsystem around $\boldsymbol{k}$, followed by a time reversal operation, which transforms $(\hat{\boldsymbol{e}}_i\times\hat{\boldsymbol{e}}_j)\cdot\boldsymbol{k} \to -(\hat{\boldsymbol{e}}_i\times\hat{\boldsymbol{e}}_j)\cdot\boldsymbol{k}$. Since the g_i functions are invariant, it is always possible to transform the given subensemble into another one where $(\hat{\boldsymbol{e}}_i\times\hat{\boldsymbol{e}}_j)\cdot\boldsymbol{k}$ has the same magnitude but the opposite sign. Hence, all contributions of the fourth term of (2.3.25) vanish.

The spin polarization of transmitted electron beam averaged over all orientations is given by

$$I\boldsymbol{P} = g[(\hat{\boldsymbol{e}}_1 \times \hat{\boldsymbol{e}}_2) \cdot \hat{\boldsymbol{e}}_3]\boldsymbol{k}, \tag{2.3.26}$$

where we denote by g the integral of $g_0 g_4^* + g_0^* g_4$ over all orientations of the molecules. The sign of $(\hat{\boldsymbol{e}}_1 \times \hat{\boldsymbol{e}}_2) \cdot \hat{\boldsymbol{e}}_3$ changes with the handedness of the molecule while g_i remain the same, as discussed in the previous subsection. We can, therefore, conclude that: (i) the spin polarization vector has the opposite sign if the handedness of the molecules is reversed, (ii) $\boldsymbol{P}$ vanishes for a racemic mixture, and (iii) the electron circular dichorism observed [6, 1] cannot be produced by a spin-flip process.

2.4 The transmission asymmetry and the dissociation asymmetry

In this section, we discuss the electronic transmission from the standpoint of spin-dependent electron scattering, discussed in section 2.3. We present a review of the transmission asymmetry formulated by Fandreyer, Thompson and Blum [25], as well as, for the first time, the inclusion of a reactive DEA channel and vibrational excitation channels.

It is well known that in the experiments of interest [6, 1, 12], the incident electron beam has a spin-polarization along the incident wave vector direction $\hat{\boldsymbol{k}}_{\boldsymbol{i}} = \hat{\boldsymbol{z}}$ in the laboratory frame, given by

$$P_0 = \frac{N_0^+ - N_0^-}{N_0^+ + N_0^-} \equiv \frac{\Delta N_0}{N_0}, \tag{2.4.1}$$

where $N_0^{\pm}$ is the number of right- $(+)$ and left-handed $(-)$ electrons entering the collision chamber at $z = 0$.

Let us first consider the electronically elastic scattering channel[4]. Along the path into the gas sample, the number of right-handed (spin-up) electrons in the solid angle $\Delta\Omega$ around $\hat{\boldsymbol{z}}$ will vary according to three spin mechanisms [25]:

- (i) scattering of spin-up electrons out of the solid angle $\Delta\Omega$;
- (ii) spin-flip $(+\frac{1}{2} \rightarrow -\frac{1}{2})$ processes into all directions;
- (iii) spin-flip processes $(-\frac{1}{2} \rightarrow +\frac{1}{2})$ into the solid angle $\Delta\Omega$;

The number of right-handed electrons collected after the collision follows the Beer-Lambert Law [25],

$$\frac{dN^+}{dz} = -\rho Q^+ N^+(z) \Longrightarrow N^+(d) = N_0^+ e^{-Q^+\rho d}, \tag{2.4.2}$$

where ρ is the sample density and d is the sample thickness. The total cross section, Q^+ for the scattering of spin-up electrons[5] is obtained by the integral of the spin-up cross section over the solid angle Ω,

[4] In fact, the vibrational excitation channel could be included in this formulation. However, we will do this in sec. 2.4.1, when we include explicitly the reactive channel.

[5] The total cross section could also incorporate the vibrationally-resolved one, but we consider the electronic elastic scattering for now.

$$Q^{+} = \int_{\Omega} d\Omega \;\; \sigma^{+}, \tag{2.4.3}$$

where $\sigma^{+} = \sigma^{++} + \sigma^{-+}$ is sum of the spin-preserving σ^{++} cross section and spin-flip σ^{-+} cross section for spin-down incident electrons. Analogously, the number of left-handed electrons N^{-} is given by

$$N^{-}(d) = N_0^{-} e^{-Q^{-}\rho d}. \tag{2.4.4}$$

Combining both equations (2.4.2) and (2.4.4) and using $N = N^{+} + N^{-}$, we obtain

$$N = N^{+} + N^{-} = N_0^{+} e^{-Q^{+}\rho d} + N_0^{-} e^{-Q^{-}\rho d}. \tag{2.4.5}$$

By using eq. (2.4.1) and transforming to current intensities

$$\frac{I(d)}{I_0} = \frac{N(d)}{N_0}, \tag{2.4.6}$$

we obtain the transmitted current intensity $I(d)$ for an initial longitudinal polarization P_0, after some algebra:

$$I(d) = I_0 e^{-\frac{1}{2}(Q^{+}+Q^{-})\rho d} \times \left\{ \cosh\left(\frac{1}{2}(Q^{+} - Q^{-})\rho d\right) - P_0 \sinh\left(\frac{1}{2}(Q^{+} - Q^{-})\rho d\right) \right\}, \tag{2.4.7}$$

where I_0 is the initial current intensity.

The total cross section for a given initial spin of the incident electron can be obtained from the optical theorem

$$Q^{\pm} = \frac{4\pi}{k_i} \operatorname{Im} f(\pm, \pm), \tag{2.4.8}$$

with the forward-direction elastic scattering amplitude given by eqs. (2.3.11) and (2.3.12).

For randomly oriented molecules, we obtain the transmitted intensity by making the substitution for the average over the molecular orientations, denoted as

$$Q^{\pm} \rightarrow \langle Q^{\pm} \rangle. \tag{2.4.9}$$

For a chiral target, the difference $\langle Q^{+} \rangle - \langle Q^{-} \rangle$ changes sign if the handedness of molecular sample is reversed, as we discussed in section 2.3.

It should be noted that the intensity $I(d)$ is also a function of the initial polarization. If $I(d, P_0)$ is the value of $I(d)$ in equation (2.4.1) for polarization $+P_0$ and $I(d, -P_0)$ the value for polarization $-P_0$, we can introduce the transmission asymmetry $a(P_0)$ which was measured by Campbell and Farago [6], and by Kessler *et al* [1], for camphor compounds,

$$a(P_0) = \frac{I(d, P_0) - I(d, -P_0)}{I(d, P_0) + I(d, -P_0)}. \tag{2.4.10}$$

Using eq. (2.4.7), the transmission asymmetry can be written in the form

$$a(P_0) = -P_0 \tanh\left[\frac{1}{2}(Q^+ - Q^-)\rho d\right]. \tag{2.4.11}$$

We can rewrite the argument of the hyperbolic function in terms of the total cross section, and apply the optical theorem to obtain

$$Q = Q^+ + Q^- = 2\frac{4\pi}{k_i}\,\mathrm{Im}\, g_0. \tag{2.4.12}$$

In terms of the quantity

$$x = ((\boldsymbol{e_1} \times \boldsymbol{e_2})\cdot\boldsymbol{e_3})\frac{\mathrm{Im}\, g_4}{\mathrm{Im}\, g_0}, \tag{2.4.13}$$

the transmission asymmetry can be written as

$$a(P_0) = -P_0 \tanh\left[\frac{1}{2}Qx\rho d\right]. \tag{2.4.14}$$

The equation above allows us to infer a "dichroism ability" by the estimate of x. Considering randomly oriented molecules, we have to substitute the averages $\langle Q\rangle$ and $\langle x\rangle$ for Q and x. For electron scattering energy around 5 eV, Campbell and Farago obtained $\langle x\rangle > 2 \times 10^{-3}$ [25].

2.4.1 The DEA asymmetry

We now consider the inclusion of the reactive DEA and vibrational excitation channels, i.e,

$$e^- + AB \begin{array}{l} \nearrow\ e^- + AB^* \\ \searrow\ A^- + B^\bullet \end{array}, \tag{2.4.15}$$

where AB denotes the target molecule that might dissociate into the A^- fragment and the $B^\bullet$ radical (DEA channel), while AB^* indicates the possibility of vibrational excitation in the electron scattering channel. The electronically elastic scattering is still assumed, with the target molecule in its ground state. We also consider the reactive DEA channel for spin-up electrons, in addition to the three spin mechanisms proposed above on page 41. The total cross section is now given by

$$Q^+ \to Q^+_{tot} = Q^+_{vib} + Q^+_{DEA} = \sigma^{-+}_{vib} + \sigma^{++}_{vib} + \sigma^{-+}_{DEA} + \sigma^{++}_{DEA}, \tag{2.4.16}$$

where σ^{-+}_{vib} and σ^{++}_{vib} are the spin-flip and spin-preserving vibrational-excitation cross sections, and σ^{-+}_{DEA} and σ^{++}_{DEA} are the spin-flip and spin-preserving DEA cross sections, respectively, also for spin-up electrons. In our notation, the total cross sections are already convoluted over the solid angle $d\Omega$ and averaged over the molecular orientations, as in equations (2.4.12) and (2.4.9). Analogously, for a spin-down incident electron,

$$Q^- \to Q^-_{tot} = Q^-_{vib} + Q^-_{DEA} = \sigma^{+-}_{vib} + \sigma^{--}_{vib} + \sigma^{+-}_{DEA} + \sigma^{--}_{DEA}. \tag{2.4.17}$$

The electron transmission asymmetry, as given in equations (2.4.10) and (2.4.11), has the same form, but now includes the vibrational and DEA channels,

$$a_{vib}(P_0) = \frac{I(d,P_0) - I(d,-P_0)}{I(d,P_0) + I(d,-P_0)} = -P_0 \tanh\left(\frac{1}{2}(Q^+_{tot} - Q^-_{tot})\rho d\right). \tag{2.4.18}$$

Let us now focus on the formation of spin-up and spin-down fragments in reactive scattering. Denoting the number of these fragments by $\eta^\pm$, with right-handed (+) or left-handed (−) superscripts, we have, for the right-handed (spin-up) species,

$$\frac{d\eta^+}{dz} = \rho\sigma^{++}_{DEA}N^+(z) + \rho\sigma^{+-}_{DEA}N^-(z). \tag{2.4.19}$$

Using equations (2.4.2) and (2.4.4), we obtain

$$\eta^+(d) = N^+_0\frac{\sigma^{++}_{DEA}}{Q^+_{tot}}(1 - e^{-Q^+_{tot}\rho d}) + N^-_0\frac{\sigma^{+-}_{DEA}}{Q^-_{tot}}(1 - e^{-Q^-_{tot}\rho d}), \tag{2.4.20}$$

and analogously, the formation of spin-down fragments is given by

$$\eta^-(d) = N^-_0\frac{\sigma^{--}_{DEA}}{Q^-_{tot}}\left(1 - e^{-Q^-_{tot}\rho d}\right) + N^+_0\frac{\sigma^{-+}_{DEA}}{Q^+_{tot}}\left(1 - e^{-Q^+_{tot}\rho d}\right). \tag{2.4.21}$$

The quantities $\eta^{\pm}(d)$ as well as $N^{\pm}(d)$ defined above depend on the spin polarization of the incident electron beam through $N_0^{\pm} = \frac{N_0}{2}(1 \pm P_0)$, where we have employed the notation of equation (2.4.1). The total number of right- and left-handed fragments for a given polarization P_0 is, therefore, written as

$$\eta(d, P_0) = \eta^{+}(d) + \eta^{-}(d) = \eta_{\infty}^{+}(P_0)\left[1 - e^{-Q_{tot}^{+}\rho d}\right] + \eta_{\infty}^{-}(P_0)\left[1 - e^{-Q_{tot}^{-}\rho d}\right], \tag{2.4.22}$$

where

$$\eta_{\infty}^{\pm}(P_0) = N_0^{\pm}\frac{Q_{DEA}^{\pm}}{Q_{tot}^{\pm}} = \frac{N_0}{2}(1 \pm P_0)\frac{Q_{DEA}^{\pm}}{Q_{tot}^{\pm}}. \tag{2.4.23}$$

Equation (2.4.22) can also be written with hyperbolic functions, as in equation (2.4.11), after some algebra, in the form

$$\begin{aligned}\eta(d, P_0) = \eta_{\infty}(P_0)\Big\{1 - e^{-\frac{1}{2}(Q_{tot}^{+}+Q_{tot}^{-})\rho d}\Big[\cosh\Big(\frac{1}{2}(Q_{tot}^{+} + Q_{tot}^{-})\rho d\Big) - \\ -\Pi(P_0)\sinh\Big(\frac{1}{2}(Q_{tot}^{+} + Q_{tot}^{-})\rho d\Big)\Big]\Big\},\end{aligned} \tag{2.4.24}$$

with

$$\eta_{\infty}(P_0) = \eta_{\infty}^{+}(P_0) + \eta_{\infty}^{-}(P_0) \text{ and } \Pi(P_0) = \frac{\eta_{\infty}^{+}(P_0) - \eta_{\infty}^{-}(P_0)}{\eta_{\infty}(P_0)}. \tag{2.4.25}$$

We define the DEA asymmetry in terms of the initial electron polarization,

$$A_{DEA}(P_0) = \frac{\eta(d, P_0) - \eta(d, -P_0)}{\eta(d, P_0) + \eta(d, -P_0)}. \tag{2.4.26}$$

Introducing the dissociation probability asymmetry,

$$\alpha_{DEA} = \frac{(Q_{DEA}^{+}/Q_{tot}^{+}) - (Q_{DEA}^{-}/Q_{tot}^{-})}{(Q_{DEA}^{+}/Q_{tot}^{+}) + (Q_{DEA}^{-}/Q_{tot}^{-})}, \tag{2.4.27}$$

and the auxiliary function

$$t(Q_{tot}^{+}, Q_{DEA}^{-}, \rho d) = \frac{e^{-\frac{1}{2}(Q_{tot}^{+}+Q_{tot}^{-})\rho d}\sinh\left(\frac{1}{2}(Q_{tot}^{+} - Q_{tot}^{-})\rho d\right)}{1 - e^{-\frac{1}{2}(Q_{tot}^{+}+Q_{tot}^{-})\rho d}\cosh\left(\frac{1}{2}(Q_{tot}^{+} - Q_{tot}^{-})\rho d\right)}, \tag{2.4.28}$$

we obtain the DEA asymmetry in terms of the gas density and thickness, the total cross sections and the initial electron polarization, for a given molecule,

$$A_{DEA}(P_0) = P_0\left[\frac{\alpha_{DEA} + t(Q^+_{tot}, Q^-_{tot}, \rho d)}{1 + \alpha_{DEA} t(Q^+_{tot}, Q^-_{tot}, \rho d)}\right]. \tag{2.4.29}$$

In the experiments performed by Dreiling *et al* [12], the electron beam is attenuated to about 50%. According to eqs. (2.4.2) and (2.4.4), this condition can be expressed as $Q^+_{tot}\rho d \approx Q^-_{tot}\rho d \approx \ln 2$. This approximation implies that $\alpha_{DEA} t \ll \alpha_{DEA} + t$, once $Q^+_{tot} - Q^-_{tot}$ is a small quantity. The hyperbolic functions in eq. (2.4.28) can be expanded to a first-order Taylor series and the DEA asymmetry for an attenuation of about 50% can be obtained as

$$A_{DEA} = 0.3\,[\alpha_{DEA} + 0.35 a_{tot}]. \tag{2.4.30}$$

The final asymmetry is obtained by using the expression above for DEA asymmetry, for each L- and D- enantiomer,

$$A = A_{DEA}(P_0)_L - A_{DEA}(P_0)_D, \tag{2.4.31}$$

and represents the asymmetry measured by Dreiling *et al* [12].

2.5 Feshbach Projection Operator

We present in this section a brief outline of the theory based on the Feshbach projection operator (FPO) approach to reactive electron scattering, and then we discuss the inclusion of the spin-orbit (SO) interaction. The latter formulation was derived by professor Marcio Varella.

Firstly, we consider the spin-independent scattering problem. There is a vast literature regarding the FPO formalism [38, 39]. Its application to electron-molecule scattering and DEA is discussed at length in a review paper by Domcke [40]. In the FPO formalism, the space spanned by the scattering states is decomposed with orthogonal projection operators, $QP = PQ = 0$, that complement each other, $(P + Q = 1)$. The definition of the Q projector is

$$Q = |\phi_d\rangle\langle\phi_d|, \tag{2.5.1}$$

where $|\phi_d\rangle$ is a localized (square integrable) state describing electron attachment to the target molecule, and accounts for resonance formation. The P-space comprises a continuum of delocalized states that should be orthogonal to $|\phi_d\rangle$ to impose the $QP = PQ = 0$ condition. The expression of the P-projection operator can be written in the form

$$P = \int d\boldsymbol{k}|\phi_{\boldsymbol{k}}\rangle\langle\phi_{\boldsymbol{k}}|. \tag{2.5.2}$$

In the expression above, $|\phi_{\boldsymbol{k}}\rangle = |\Phi_0\rangle|\boldsymbol{k}\rangle$, where $|\Phi_0\rangle$ is the target ground state and $|\boldsymbol{k}\rangle$ is a plane wave, so that $\langle\phi_d|\phi_{\boldsymbol{k}}\rangle = 0$.

The localized state $|\phi_d\rangle$, often referred to as the discrete component (in reference to its discrete energy), is parametrically dependent on the nuclear coordinate R in the sense of the Born-Oppenheimer (BO) approximation, $\langle \boldsymbol{r}R|\phi_d\rangle = \phi_d(\boldsymbol{r}; R)$, and likewise for the continuum states, $\langle \boldsymbol{r}R|\phi_{\boldsymbol{k}}\rangle = \phi_{\boldsymbol{k}}(\boldsymbol{r}; R)$, where $\boldsymbol{r}$ denotes all the electronic coordinates and the semicolon indicates the parametric dependence on R. For simplicity, the dissociation process is described in a pseudo-diatomic model, such that a single vibrational coordinate describing the relative motion of the fragments will suffice.

Let us consider the vibrational excitation and DEA channels. The outgoing asymptotic states in P-space represent the direct scattering, and are given by

$$P\psi^{(+)}_{\boldsymbol{k_i}\nu_i} \xrightarrow{r_{N+1}\to\infty} \phi_{\boldsymbol{k}\nu_i} + \sum_{\nu_i}^{open} T_{\boldsymbol{k_f}\nu_f,\boldsymbol{k_i}\nu_i}\Phi_{0\nu_f}\left(\frac{1}{r_{N+1}}e^{ik_f r_{N+1}}\right), \tag{2.5.3}$$

where $\nu_{i(f)}$ denotes the initial (final) vibrational state, $\boldsymbol{k_{i(f)}}$ is the initial (final) wave vector, and $T_{\boldsymbol{k_f}\nu_f,\boldsymbol{k_i}\nu_i}$ is the T-matrix element for the vibrational excitation.

The reactive scattering is represented in Q-space, with the outgoing asymptotic condition

$$Q\psi^{(+)}_{\boldsymbol{k_i}\nu_i} \xrightarrow{R\to\infty} \int^{open} dK\ T^{DEA}_{K,\boldsymbol{k_i}\nu_i}\Phi_{A^-}\Phi_B\ e^{iKR}, \tag{2.5.4}$$

where $T^{DEA}_{K,\boldsymbol{k_i}\nu_i}$ is the T-matrix element for DEA. The electronic states Φ_{A^-} and Φ_B represent the molecular fragments, K is a plane wave accounting for the relative free motion of the fragments, and R is the pseudo-diatomic coordinate that describes the dissociation process in the model. In eq. (2.5.4), the plane wave e^{iKR} follows from the assumption of one-dimensional motion.

The Hamiltonian describing Coulomb scattering is denoted as

$$H_C = T_{nuc} + H_{free} + V_C \equiv T_{nuc} + H_{ele}, \tag{2.5.5}$$

where T_{nuc} is the nuclear kinetic operator, H_{free} is the interaction-free electronic Hamiltonian, given by the sum of the projectile kinetic energy (T_{N+1}) and the electronic Hamiltonian of the N-electron target molecule (H_N), and V_C is the Coulomb interaction.

Since the description is in the BO approximation, we have $[T_{nuc}, P] = [T_{nuc}, Q] = 0$, and the Hamiltonian projected onto $Q + P$ is given by

$$\begin{aligned} H_C = (Q+P)H_C(Q+P) = \\ (PH_CP + QH_CQ) + (QH_{ele}P + PH_{ele}Q) \equiv \mathcal{H}_{free} + \mathcal{H}_{rea}, \end{aligned} \tag{2.5.6}$$

where $\mathcal{H}_{free} = PH_CP + QH_CQ$ accounts the direct reaction, and $\mathcal{H}_{rea} = QH_{ele}P + PH_{ele}Q$ accounts the reactive scattering. The corresponding Lippmann-Schwinger equation is

$$|\psi^{(\pm)}_{\boldsymbol{k_i}\nu_i}\rangle = |\phi_{\boldsymbol{k_i}}\rangle|\nu_i\rangle + \mathcal{G}^{(\pm)}_{free}\mathcal{H}_{rea}|\psi^{(\pm)}_{\boldsymbol{k_i}\nu_i}\rangle, \tag{2.5.7}$$

with $\mathcal{G}^{(\pm)}_{free} = [E - \mathcal{H}_{free} \pm i\epsilon]^{-1}$. The projection of eq. (2.5.7) onto the Q- and P-spaces

leads to a system of coupled equations for the projected states, $P|\psi^{(\pm)}_{\boldsymbol{k_i}\nu_i}\rangle \equiv |\psi^{(\pm)}_{P,i}\rangle$ and $Q|\psi^{(\pm)}_{\boldsymbol{k_i}\nu_i}\rangle \equiv |\psi^{(\pm)}_{Q,i}\rangle$, having well-known solutions [24],

$$|\psi^{(\pm)}_{P,i}\rangle = |\phi_{\boldsymbol{k_i}}\rangle|\nu_i\rangle + \mathcal{G}^{(\pm)}_{PP} H^{ele}_{PQ}|\psi^{(\pm)}_{Q,i}\rangle, \tag{2.5.8}$$

with

$$|\psi^{(\pm)}_{Q,i}\rangle \equiv |\phi_d\rangle|\xi^{(\pm)}_d\rangle = |\phi_d\rangle \frac{1}{E - T_{nuc} - V^{\pm}_{opt}} U_{\boldsymbol{k_i}}|\nu_i\rangle. \tag{2.5.9}$$

In the equations above, $\mathcal{G}^{(\pm)}_{PP} = [E - PH_C P \pm i\epsilon]^{-1}$ and $H^{ele}_{PQ} = PH_{ele}Q$, while $|\xi^{(\pm)}_d\rangle = \langle\phi_d|\psi^{(\pm)}_{\boldsymbol{k_i}\nu_i}\rangle$ is the Q-component vibrational state (with integration over electronic coordinates implied), and

$$U_{\boldsymbol{k_i}} = \langle\phi_d|H^{ele}_{QP}|\phi_{\boldsymbol{k_i}}\rangle \tag{2.5.10}$$

is the entry amplitude describing electron attachment ($P \rightarrow Q$), while $U^*_{\boldsymbol{k}}$ is the exit amplitude accounting for auto-ionization ($Q \rightarrow P$). The optical potential V_{opt} is a complex and energy dependent potential surface wherein the nuclear dynamics of the resonance state takes place. It is given in the form [24]

$$V^{(\pm)}_{opt} = V_0(R) + \epsilon_d(R) + \Delta(R, E - H_0) \mp \frac{i}{2}\Gamma(R, E - H_0), \tag{2.5.11}$$

where $V_0(R)$ is the BO potential energy surface of the target electronic ground state and $\epsilon_d(R) = \langle\phi_d|H^{ele}_{QQ}|\phi_{\boldsymbol{k_i}}\rangle$ is a correction to V_0 arising from electron attachment [24]. The coupling of ϕ_d to the continuum gives rise to the complex potential $\Delta \mp \frac{i}{2}\Gamma$, which is in turn dependent on the vibrational Hamiltonian of the target, $H_0 = T_{nuc} + V_0(R)$. Here, $\Delta(R, E - H_0)$ and $\Gamma(R, E - H_0)$ are defined by

$$\Delta(R, E - H_0) = \frac{1}{2\pi}\mathrm{P}\int_0^\infty dE' \frac{\Gamma(R, E')}{E - E'}, \tag{2.5.12}$$

and

$$\Gamma(R, E - H_0) = 2\pi \int_\Omega d\hat{\boldsymbol{k}}_{\boldsymbol{i}} |U_{\boldsymbol{k_i}}|^2, \tag{2.5.13}$$

where P indicates the Cauchy principal value in eq. (2.5.12), and Ω in the integral in eq. (2.5.13) indicates it is performed over all directions. Since both are non-local functions,

in the sense that these operators depend on the energy of the system in regions beyond that defined by R, evaluating these terms can be complicated. Therefore it is common to use the local approximation

$$V_{opt}(R) \approx V_0(R) + (\epsilon_d(R) + \Delta) \mp \frac{i}{2}\Gamma, \tag{2.5.14}$$

where $(\epsilon_d + \Delta)$ would be the resonance position and Γ the corresponding width. According to eq. (2.5.4), the DEA transmission amplitude can be obtained as [24]

$$T^{DEA}_{K,\boldsymbol{k_i}\nu_i} = \left(\frac{\mu}{K}\right)^{1/2} \lim_{R\to\infty} e^{-iKR}\xi_d^{(+)}(R), \tag{2.5.15}$$

where μ is the reduced mass for pseudo-diatomic model. The vibrational wave function $\xi_d^{(+)}(R)$ is obtained by using eq. (2.5.9) and is given by

$$\xi_d^{(+)}(R) = \langle R| \frac{1}{E - T_{nuc} - V_{opt}^{(+)}} U_{\boldsymbol{k_i}} |\nu_i\rangle. \tag{2.5.16}$$

In practice, we can evaluate the DEA cross section for a pseudo-diatomic model running a quantum dynamical simulation. We would then obtain the quantity corresponding to eq. (2.5.15) in the local approximation for the optical potential, given by (2.5.14).

Analogously, the T-matrix elements for vibrational excitation is obtained by using eq. (2.5.8) and the asymptotic condition (2.5.4),

$$T_{\boldsymbol{k_f}\nu_f,\boldsymbol{k_i}\nu_i} = T^{bg}_{\boldsymbol{k_f}\nu_f,\boldsymbol{k_i}\nu_i} + \langle \nu_f | U^*_{\boldsymbol{k_f}} \frac{1}{E - T_{nuc} - V_{opt}^{(+)}} U_{\boldsymbol{k_i}} |\nu_i\rangle, \tag{2.5.17}$$

where $T^{bg}_{\boldsymbol{k_f}\nu_f,\boldsymbol{k_i}\nu_i}$ is the background contribution.

2.5.1 Inclusion of the spin-orbit interaction

We now comment on the reactive scattering from the full potential, $V = V_C + V_{SO}$. The latter is the spin-orbit potential, which is written in terms of the Pauli matrices $\boldsymbol{\sigma}$:

$$V_{SO} = \boldsymbol{\Lambda} \cdot \boldsymbol{\sigma} = \Lambda_x\sigma_x + \Lambda_y\sigma_y + \Lambda_z\sigma_z, \tag{2.5.18}$$

where $\boldsymbol{\Lambda} \cdot \boldsymbol{\sigma}$ represents the spin-orbit coupling, $\boldsymbol{\Lambda} = \vec{E} \times \vec{p}$, and $\vec{E}$ and $\vec{p}$ are the molecular electric field and electron momentum, respectively. The scattering states must be repre-

sented with the inclusion of spin states, so that $|\psi^{(\pm)}_{\boldsymbol{k_i}\nu_i}\rangle \rightarrow |\psi^{(\pm)}_{\boldsymbol{k_i}\nu_i m_s}\rangle$, where m_s denotes the spin projection on the $\boldsymbol{k_i}$ direction in the laboratory-fixed frame ($m_s = \pm\frac{1}{2}$).

The projection of the SO operator onto $(P+Q)$ gives

$$(P+Q)V_{SO}(P+Q) \equiv (V^{SO}_{PP} + V^{SO}_{QQ}) + (V^{SO}_{PQ} + V^{SO}_{QP}) \equiv \mathcal{W}_{free} + \mathcal{W}_{rea}, \tag{2.5.19}$$

where $\mathcal{W}_{free}$ accounts for non reactive collisions ("direct" $P \rightarrow P$ and $Q \rightarrow Q$ scattering), while $\mathcal{W}_{rea}$ accounts for reactive scattering (Q-P coupling). This way, we can generalize eq. (2.5.6) for $H_C + V_{SO}$ and obtain the Lippmann-Schwinger equation with inclusion of the spin-orbit interaction.

The T-matrix decomposition with the SO interaction is similar, but more complicated than the one discussed above, so we skip to the final expressions for the T-matrix elements. Some convenient approximations are made for simplicity. We neglect second- and higher-order terms in the interaction, denoted as $\mathcal{O}(V_C V_{SO})$, $\mathcal{O}(V_C V^2_{SO})$ and $\mathcal{O}(V^2_C V_{SO})$, as well as spin-orbit interactions in the direct P-channel, V^{SO}_{PP}. The vibrational excitation T-matrix elements are given by

$$\begin{aligned} T_{\boldsymbol{k_f}\nu_f m_f, \boldsymbol{k_i}\nu_i m_i} = \langle \nu_f m_f | \Bigg\{ & \left[T^{bg}_{\boldsymbol{k_f}\nu_f, \boldsymbol{k_i}\nu_i} + U^*_{\boldsymbol{k_f}} \frac{1}{E - T_{nuc} - V^{(+)}_{opt}} U_{\boldsymbol{k_i}} \right] + \\ & \left[W^{0*}_{\boldsymbol{k_f}} \sigma_z \frac{1}{E - T_{nuc} - V^{(+)}_{opt}} U_{\boldsymbol{k_i}} + U^*_{\boldsymbol{k_f}} \frac{1}{E - T_{nuc} - V^{(+)}_{opt}} W^0_{\boldsymbol{k_i}} \sigma_z \right] + \\ & \left[W^{-*}_{\boldsymbol{k_f}} \sigma^*_- \frac{1}{E - T_{nuc} - V^{(+)}_{opt}} U_{\boldsymbol{k_i}} + U^*_{\boldsymbol{k_f}} \frac{1}{E - T_{nuc} - V^{(+)}_{opt}} W^-_{\boldsymbol{k_i}} \sigma_- \right] + \\ & \left[W^{+*}_{\boldsymbol{k_f}} \sigma^*_+ \frac{1}{E - T_{nuc} - V^{(+)}_{opt}} U_{\boldsymbol{k_i}} + U^*_{\boldsymbol{k_f}} \frac{1}{E - T_{nuc} - V^{(+)}_{opt}} W^+_{\boldsymbol{k_i}} \sigma_+ \right] \Bigg\} |\nu_i m_i\rangle, \end{aligned} \tag{2.5.20}$$

where we use $\sigma_x = \frac{1}{2}(\sigma_+ + \sigma_-)$ and $\sigma_y = \frac{1}{2i}(\sigma_+ - \sigma_-)$, and we define the amplitudes that account for the SO effects

$$W^0_{\boldsymbol{k_i}} = \langle \phi_d | Q \Lambda_z P | \phi_{\boldsymbol{k_i}} \rangle \quad \text{and} \quad W^{\pm}_{\boldsymbol{k_f}} \langle \phi_d | Q(\Lambda_x \pm i\Lambda_y) P | \phi_{\boldsymbol{k_i}} \rangle. \tag{2.5.21}$$

Due to the above mentioned approximations, the first-order terms in V_{SO} are kept

only in the numerators of eq. (2.5.20). Therefore, the model accounts for spin-dependent scattering through the amplitudes $W^{0,\pm}_{\boldsymbol{k_f}}$, but not through the complex potential V_{opt}. As a concrete example let us consider spin-flip processes in the vibrational excitation T-matrix. The SO amplitudes can describe spin-flips in the P-Q and Q-P transitions, i.e., as the electron attaches ($W^{\pm}_{\boldsymbol{k_i}}$) to the target molecule forming a resonance, and also as it subsequently detaches ($W^{\pm *}_{\boldsymbol{k_f}}$). However, the vibration dynamics on the V_{opt} complex potential will be governed by the Coulomb potential.

It is clear that the terms in the first square brackets correspond to the T-matrix element for spinless scattering, given in eq. (2.5.17). The terms in the second square brackets account for spin-preserving matrix elements, analogously to g_4 discussed in section 2.3, while the terms in the third and fourth square brackets account for the spin-flip matrix elements, analogously to g_i, $i = 1, 2, 3$, discussed in the same section.

The chiral asymmetry in forward electron scattering by a sample of randomly oriented molecules would arise from the spin-preserving T-matrix elements [17], so hereafter we disregard the spin-flip matrix elements. The expression of interest is

$$T_{\pm\pm} = \left(T^{bg}_{\boldsymbol{k_f}\nu_f,\boldsymbol{k_i}\nu_i} + \langle \nu_f | U^*_{\boldsymbol{k_f}} \frac{1}{E - T_{nuc} - V^{(+)}_{opt}} U_{\boldsymbol{k_i}} | \nu_i \rangle \right) \pm \left(\langle \nu_f | W^{0*}_{\boldsymbol{k_f}} \frac{1}{E - T_{nuc} - V^{(+)}_{opt}} U_{\boldsymbol{k_i}} | \nu_i \rangle + \langle \nu_f | U^*_{\boldsymbol{k_f}} \frac{1}{E - T_{nuc} - V^{(+)}_{opt}} W^{0}_{\boldsymbol{k_i}} | \nu_i \rangle \right) \equiv T_0 \pm T_1, \tag{2.5.22}$$

where, for simplicity, $T_{\pm\pm} = T_{\boldsymbol{k_f}\nu_f=\pm\frac{1}{2},\boldsymbol{k_i}\nu_i=\pm\frac{1}{2}}$.

We use the convention for the normalization of the free states as in Ref. [24], $k^{1/2}(2\pi)^{-3/2}|\boldsymbol{k}\rangle$, where $|\boldsymbol{k}\rangle$ is a plane wave, so the relation between scattering amplitudes and T-matrix elements is given by

$$f_{\pm\pm} = \frac{(2\pi)^2}{\sqrt{k_i k_f}} T_{\pm\pm} = \frac{(2\pi)^2}{\sqrt{k_i k_f}} (T_0 \pm T_1) \equiv f_0 \pm f_1. \tag{2.5.23}$$

We recall the total cross section for an initial spin of the incident electron can be obtained from the optical theorem, expressed in eq. (2.4.8). Also, for randomly oriented molecules, we make the average over the molecular orientations, as in eq. (2.4.9). The total cross section for incident electrons with $\pm$ spin projection averaged over the target orientation

is given by

$$\langle Q_{tot}^{\pm}\rangle = \frac{4\pi}{k_i}\frac{1}{4\pi}\int d\Omega \frac{(2\pi)^2}{\sqrt{k_i k_f}}\,\mathrm{Im}[T_{\pm\pm}(\nu_0,\boldsymbol{k_i}\leftarrow\nu_0,\boldsymbol{k_i})] = \frac{4\pi}{k_i}\Big[\langle \mathrm{Im}(f_0)\rangle \pm \langle \mathrm{Im}(f_1)\rangle\Big], \tag{2.5.24}$$

where forward scattering in the vibrationally elastic channel has been indicated in the T-matrix by $T_{\pm\pm}(\nu_0,\boldsymbol{k_i}\leftarrow\nu_0,\boldsymbol{k_i})$. From eq. (2.5.24), we obtain the asymmetry quantity for a given enantiomer,

$$\langle Q_{tot}^{+}\rangle - \langle Q_{tot}^{-}\rangle = \frac{8\pi}{k_i}\langle \mathrm{Im}(f_1)\rangle. \tag{2.5.25}$$

Using the expression above, we obtain the transmission asymmetry, as it was expressed in eq. (2.4.10),

$$a(P_0) = -P_0\Big[\tanh\left(\frac{4\pi}{k_i}\langle \mathrm{Im}(f_1)\rangle \rho d\right)\Big] \approx \frac{4\pi P_0}{k_i}\langle \mathrm{Im}(f_1)\rangle \rho d, \tag{2.5.26}$$

where we made the approximation $\tanh(z)\approx z$ for $z \ll 1$, since the asymmetry effects are of the order of 10^{-5}-10^{-3} [13, 25].

The above expression provides a theoretical basis to understand the experimental signature of resonances in the scattering asymmetries. This signature would arise from the inverse of the $[E - T_{nuc} - V_{opt}]$ operator, and the simplest possible approximation to illustrate this fact would be: (i) neglecting the dependence of V_{opt} on the collision energy, (ii) neglecting the nonlocal dependence of V_{opt} on the vibrational coordinates and also the dependence of the amplitudes $U_{\boldsymbol{k}}$ and $W_{\boldsymbol{k}}$ on these coordinates (in this case, only vibrationally elastic scattering can be accounted for), and (iii) making a fixed-nuclei approximation to the vibrationally elastic cross section. In this perhaps oversimplified collision picture, the complex potential can be written as $V_{opt} \approx E_{res} - \frac{i}{2}\Gamma_{res}$, where the resonance position E_{res} and width Γ_{res} are no longer operators, such that

$$T_1 \approx W_{\boldsymbol{k_f}}^{0*}\frac{1}{E - E_{res} - \frac{i}{2}\Gamma_{res}}U_{\boldsymbol{k_i}} + U_{\boldsymbol{k_f}}^{*}\frac{1}{E - E_{res} - \frac{i}{2}\Gamma_{res}}W_{\boldsymbol{k_i}}^{0} = \frac{2\,\mathrm{Re}[W_{\boldsymbol{k_f}}^{0*}U_{\boldsymbol{k_i}}]}{E - E_{res} - \frac{i}{2}\Gamma_{res}}, \tag{2.5.27}$$

and hence

$$a(P_0) \approx -\rho d P_0 \frac{(2\pi)^3}{E} \langle \mathrm{Re}[W^{0*}_{\boldsymbol{k_f}} U_{\boldsymbol{k_i}}] \rangle \frac{\Gamma_{res}}{(E - E_{res})^2 + (\frac{1}{2}\Gamma_{res})^2}. \tag{2.5.28}$$

The expression above has a Lorentzian profile directly related to those found in the elastic cross section, which represent the resonance characterization. In chapter 4, we will present a linear fit analysis employing eq. (2.5.28) over for the Münster experimental data. We obtain a feasible value for $W_{\boldsymbol{k}}$ and discuss the scattering asymmetry behaviour for energies below 1 eV.

Analogously to the transmission asymmetry, the DEA asymmetry for a randomly oriented gas would only arise from the spin-preserving processes, as does the scattering asymmetry. In this case,

$$\begin{aligned} T^{DEA}_{\pm\pm} \approx \left(\frac{\mu}{K}\right)^{1/2} \lim_{R\to\infty} e^{-iKR} \Bigg[\langle R| \frac{1}{E - T_{nuc} - V^{(+)}_{opt}} U_{\boldsymbol{k_i}} |\nu_i\rangle \pm \\ \langle R| \frac{1}{E - T_{nuc} - V^{(+)}_{opt}} W^0_{\boldsymbol{k_i}} |\nu_i\rangle \Bigg] \equiv T^{DEA}_0 \pm T^{DEA}_1. \end{aligned} \tag{2.5.29}$$

We do not obtain simple expressions for the DEA channel, as in (2.5.27) and (2.5.28). Even so, it is possible to estimate the DEA T-matrix if an adequate approximation for V_{opt} is applied. In chapter 4, we evaluate T^{DEA}_0 and T^{DEA}_1 using three approximations for the complex potential and discuss the relation between the dissociation amplitude and the dissociation asymmetry.

Chapter 3

Anionic states of halocamphor molecules

We present in this chapter the integral cross sections (ICSs) for the halocamphors 3BrC, 3IC and 10IC. The resonances are characterized from these calculations and the dissociation mechanisms are inferred. We also discuss the asymmetry measuremens of Dreiling and Gay [12], as well as the transmission asymmetry measured by Mayer *et al.* [1], in light of the present results. Our results and discussion were reported in the journal Physical Chemistry Chemical Physics in 2021 [41].

3.1 Computational Procedures

The molecular geometries were optimized using density functional theory (DFT), as implemented in the Gaussian09 [42] package, with the B3LYP functional and aug-cc-pVDZ basis set. For iodocamphor molecules, a pseudopotential also was applied for the iodine atom with a 9s7p7d/5s4p3d basis set [43]. The target electronic structure calculations were performed with the GAMESS package [44]. In both the bound-state and scattering calculations, the nuclei and core electrons were replaced with the norm-conserving pseudopotentials of Bachelet, Hamann and Schüter (BHS) [35]. The target electronic ground state was described at the restricted Hartree-Fock (HF) level, with a set of Cartesian Gaussian basis sets generated as described by Bettega *et al* [36]. We employed a 5s5p2d basis set for the carbon and oxygen atoms, 6s5p2d for the halogen atoms, and the 4s/3s basis set reported by Dunning [45] for the hydrogen atoms, resulting in a total of 430 basis

functions and 406 molecular orbitals (MOs), after dropping the 24 spherical contaminants.

As we discussed in Section 2.2, the scattering wave function is expanded in a basis formed by spin-adapted $(N+1)$-electron Slater determinants, named configuration state functions (CFSs). These configurations are given by products of target states and single-particle functions (scattering orbitals) and were considered in the static-exchange (SE) and the static-exchange plus polarization (SEP) approximations.

Modified virtual orbitals (MVOs) [34] were used as both particle and scattering orbitals. The MVOs were generated from positively charged Fock operators, giving rise to more compact virtual orbitals which can be compared with those calculated with the 6-31G(d) basis sets, which helps the assignment of resonance characters. Following this strategy, the MVOs for 3BrC were generated with charge +8, while the 3IC and 10IC MVOs were generated with charge +12.

The CSF spaces were obtained from the energy criterion proposed by Kossoski and Bettega [33]. Single electron excitations of the target with the triplet spin coupling were chosen according to $\Delta \geq \epsilon_{part} - \epsilon_{hole} + \epsilon_{scat}$, where ϵ_{scat}, ϵ_{part}, and ϵ_{hole} are the energies of the scattering, particle, and hole orbitals, respectively, and Δ is an energy threshold. The energy cutoffs were adjusted until we were able to reproduce some previously obtained results, such as the resonances observed by Scheer and Gay [15] in the case of 3BrC. For iodocamphors, we evaluated the energy difference between the anionic and neutral states (vertical energy) using DFT calculations. For 3BrC, the threshold was set to $\Delta = -2.000$ hartree, which generated 15,142 CFSs. For 3IC, we obtained 10,897 CFSs with $\Delta = -3.5880$ hartree, and 28,310 configurations with $\Delta = -1.6514$ hartree, for 10IC.

The resonance characters were inferred from two procedures: The inspection of pseudo eigenstates obtained from the diagonalization of the scattering Hamiltonian represented in the CSF basis, and the analysis of virtual orbitals calculated with the compact 6-31G(d) basis set.

3.2 Results

First of all, we would like to mention some preliminary results using the DFT method. We investigated the existence of valence bound states employing the M06-2X functional and the aug-cc-pVDZ basis set, following the benchmark in [46]. Only 3IC indicates a bound-state with the not so significant energy of 0.05 eV. The anion forms of the three compounds show a negative dissociation threshold for the halide elimination reaction, evaluated by the energy difference between isolated fragments and neutral species. The target molecules have dipole moment magnitudes around 4.42 D (3BrC), 4.22 D (3IC), and 3.38 D (10IC). Since the target molecules have supercritical dipole moments, we investigated the dipole bound states (DBSs) employing the strategy proposed by Skurski et al. [47]. The aug-cc-pVDZ basis set was augmented with 6s6p diffuse functions placed at the hydrogen lying the closest to the positive site of the dipole moment vector. We performed MP2 and CCSD calculations, for the neutral and anion species, in the same geometries employed in the scattering study. The results indicate the formation of weakly bound DBSs for the three halocamphor molecules. The CCSD method provides larger VBEs than MP2, around 7 meV for 10IC, and 16 meV for both 3BrC and 3IC, indicating that shorter-ranged correlation interactions play an important role in binding the extra electron. Fig. 3.1 shows the dipole orbitals that represent the formation of DBS.

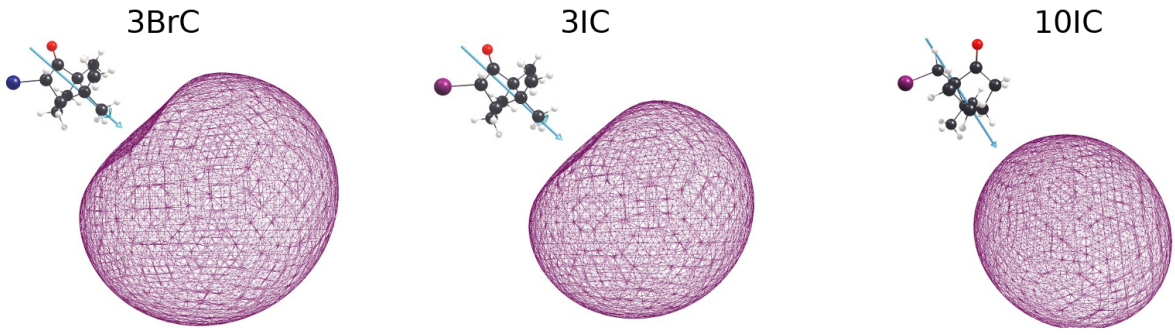

Figure 3.1: Singly occupied orbitals of the dipole bound states of 3-bromocamphor (left), 3-iodocamphor (center), and 10-iodocamphor (right), for the isovalues 0.0020, 0.0020, and 0.0013, respectively.

3-bromocamphor

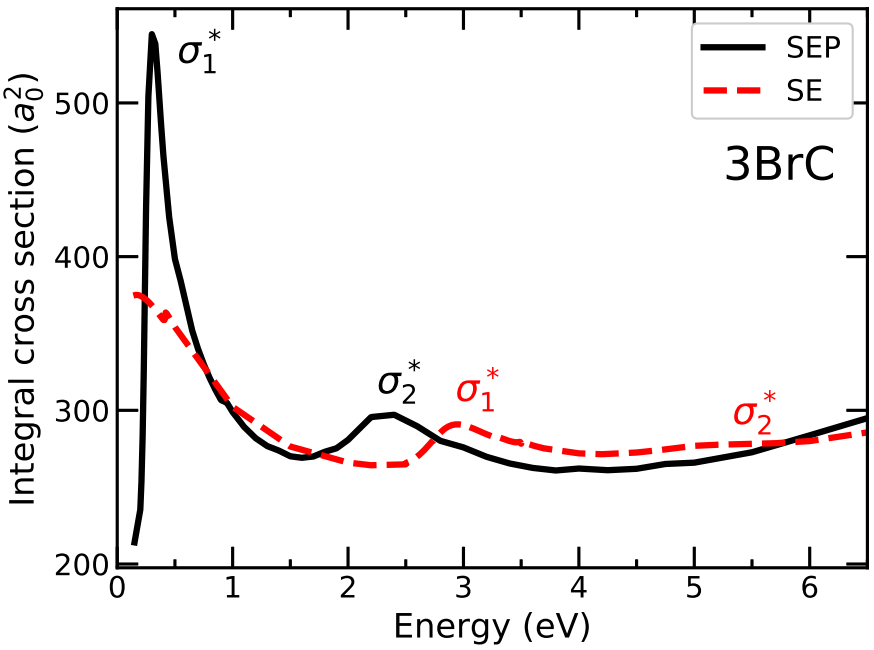

Figure 3.2: Integral cross section for 3BrC in the SE (red-dashed line) and SEP (black-full line) approximations.

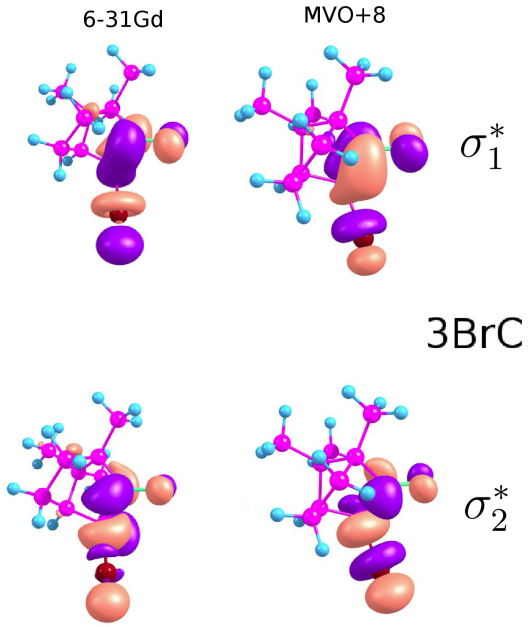

Figure 3.3: Lowest-lying virtual orbitals obtained with the 6-31G(d) compact basis set (left panel) along with the MVOs obtained with the charge +8 (right panel), for 3BrC.

The calculated ICS for 3BrC in the SE and SEP approximations are presented in Fig. 3.2. The compact virtual orbitals obtained from the HF/6-31Gd, as well as the correspondent MVOs are presented in Fig. 3.3. The ICS in the SE approximation displays two broad structures around 3.0 eV and 5.1 eV. As expected, the inclusion of correlation-polarization effects in the SEP approximation shifts the resonances to lower energies, namely 0.29 eV (width of 0.126 eV) and 2.53 eV (width of 0.37 eV). The resonance characters can be inferred from the virtual orbitals. As shown in Fig. 3.3, the LUMO and LUMO+1 have an antibonding amplitude on the C=O bond, as well as on the C-Br bond, thus having mixed π^*/σ^* character. In spite of the π^* admixture, the resonances will be labelled σ_1^* and σ_2^* in order of increasing energy.

3-iodocamphor

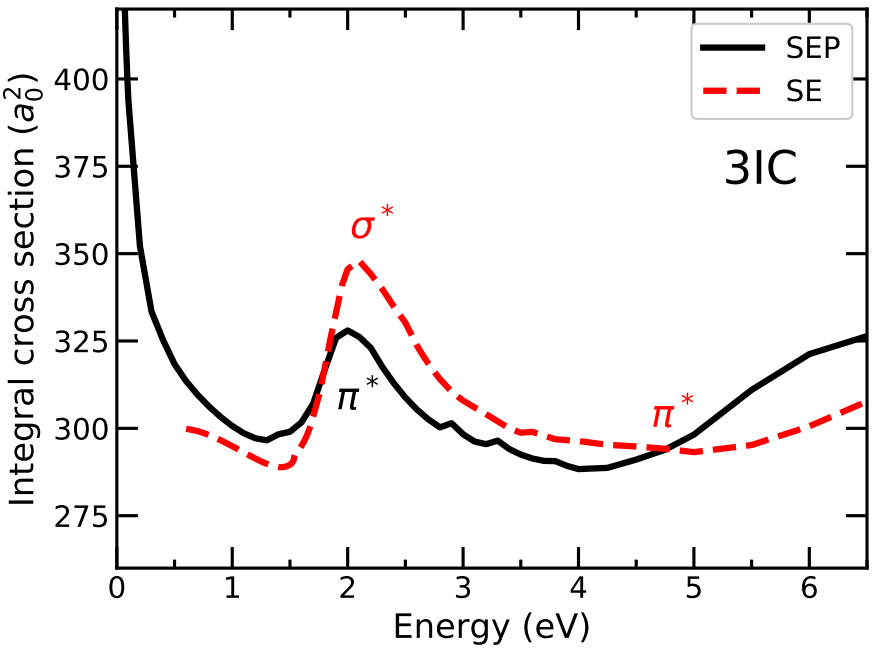

Figure 3.4: Integral cross section for 3IC in the SE (red-dashed line) and SEP (black-full line) approximations.

Fig. 3.4 presents the calculated ICS for 3IC in the SE and SEP approximations. As in the case of 3BrC, the ICS in the SE approximation has two broad structures around 2.2 eV and 4.5 eV. In the SEP approximation, the lower lying anion state becomes bound by 0.10 eV, as indicated by the diagonalization of the scattering Hamiltonian represented in the CSF basis. The second resonance is shifted to 2.00 eV and shows a more clear signature

than in the SE level, having a width of 0.50 eV. We also analyzed the lowest lying VOs, as shown in Fig. 3.5. The 3IC LUMO has a predominant σ^* character, although with some admixture of π^* character, while the 3IC LUMO+1 has π^* character. Following these orbital characters, the anion states will be labelled σ^* for the bound state and π^* for the resonance.

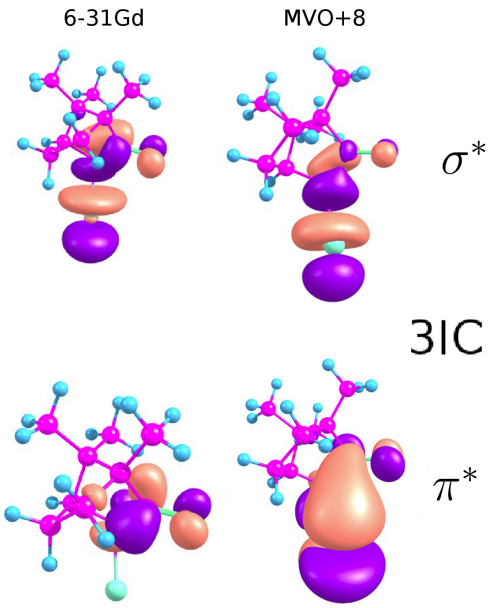

Figure 3.5: Lowest-lying virtual orbitals obtained with the 6-31G(d) compact basis set (left panel) along with the MVOs obtained with the charge+12 (right panel), for 3IC.

10-iodocamphor

The calculated ICS for the 10IC in the SE and SEP approximations are presented in Fig. 3.6. The ICS in the SE approximation has two broad structures, as well as in the 3IC and 3BrC results, around 2.4 eV and 5.5 eV. In the SEP approximation, the first resonance is shifted to 0.23 eV and has a width of 0.037, the sharpest resonance identified in both molecules. The second resonance is shifted to 1.77 eV, having a width of 0.194 eV. In accord to lowest lying VOs, as shown in Fig. 3.7, the first anionic state is a σ^* resonance, analogue that σ^* bound state in 3IC. The second resonance is a π^* temporary state, similarly to that obtained in 3IC.

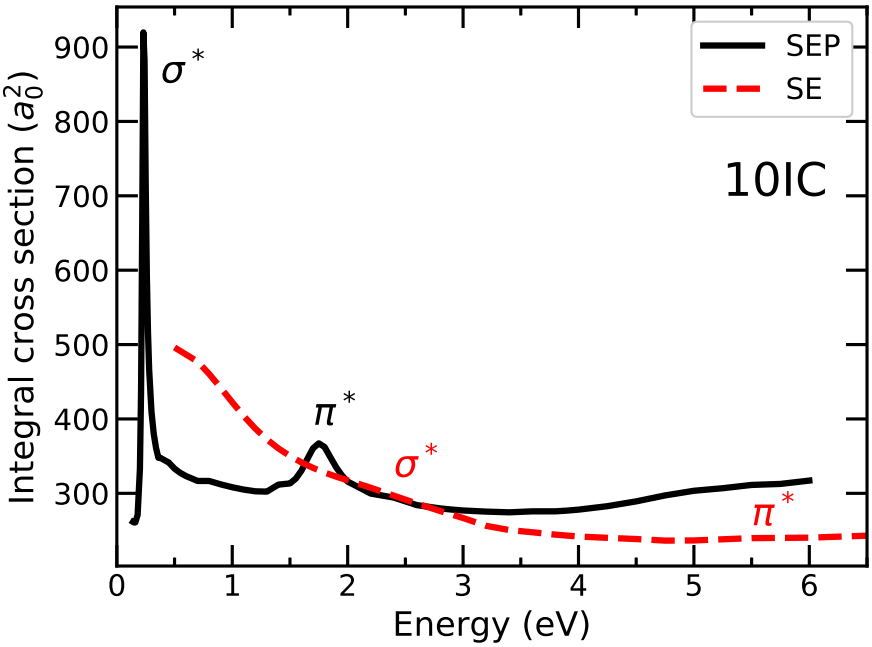

Figure 3.6: The integral cross section calculated for 10IC. The black-full line is the SEP level, while the red-dashed line is the SE level.

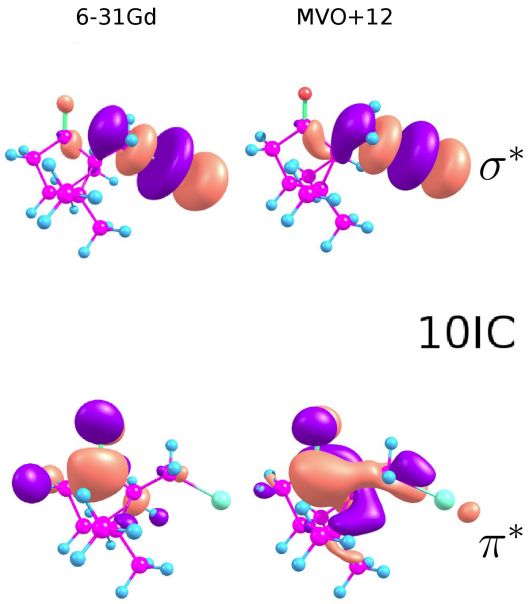

Figure 3.7: The two lowest-lying compact virtual orbitals with HF/6-31Gd and the correspondent MVOs for the 10IC.

3.3 Discussion

Table 3.1 summarizes the SMCPP results in the SEP level, along with the ETS data for 3BrC [15] and the estimated energies of the lowest-lying anion states obtained with M06-2X/aug-cc-pVDZ level. We also show vertical attachment energies (VAEs) obtained from empirical corrections of the compact virtual orbital energies (VOEs), according to Staley and Strnad [48] for π^* resonances and Chen and Gallup [49] for σ^* resonances. The latter is expected to be less accurate, as learned from experience.

Table 3.1: Energies of anionic states and widths (in parenthesis), in eV, obtained with the SMCPP method. States are labeled according to orbital character. Other results are shown for comparison.

3-bromocamphor	σ_1^*	σ_2^*
SMCPP	0.29 (0.126)	2.53 (0.37)
ETS data [15]	0.53	1.94
Scaled VOEs	0.03	1.71
M06-2X/aug-cc-pVDZ	0.36	
3-iodocamphor	σ^*	π^*
SMCPP	-0.10	2.00 (0.50)
Scaled VOEs	-0.23	1.09
M06-2X/aug-cc-pVDZ	-0.05	
10-iodocamphor	σ^*	π^*
SMCPP	0.23 (0.037)	1.77 (0.19)
Scaled VOEs	0.26	1.10
M06-2X/aug-cc-pVDZ	0.429	

In general, our calculations are in good agreement with previous results, as shown in Table 3.1. The resonance positions obtained from the SMCPP method typically agree within 0.3 eV with the ETS data. The estimated VAEs obtained from scaled VOEs are close to the present scattering results. Considering the energy precision in our calculations, the nature of the 3IC σ^* state must be better understood. It is possible its energy corresponds to a positive value, which implies in a resonance close to 0 eV. This aspect is discussed later.

We can conclude that the polarization levels proposed are adequate, and that the

calculated halocamphors anionic spectra are consistently described. Having said this, we should discuss the resonances lifetimes estimated from the widths of the peaks in the calculated ICSs. During the vibration of the anion states, the electronic ejection (auto-ionization) and dissociation channels compete, where larger lifetimes (smaller widths) favor the latter channel. Energies and widths of resonances should vary as a function of the molecular geometry, particularly, the stretch of carbon-halogen bonds, although the vertical widths provide important information on the lifetimes. The 3BrC σ_1^* and 10IC σ^* resonances have the largest lifetimes, and they may allow for longer vibrational relaxation times. The 10IC σ^* lifetime (vertically $\sim$ 18 fs) is about 4 times larger than that of 3BrC σ_1^* ($\sim$ 5 fs), which could be expected to significantly enhance the dissociation rates of the former molecule with respect to the latter. **We bring to light one point concerning the larger DEA asymmetry measured by Dreiling *et al.*** [12]. Because 10IC has a longer lifetime, it should have a larger DEA cross section, and therefore a larger DEA asymmetry. The higher lying resonances (3BrC σ_2^*, 3IC π^* and 10IC π^*) have widths around 0.5 eV, corresponding to small lifetimes ($\sim$ 1 fs) that disfavor dissociation. The shorter the lifetime, the greater the electron detachment probability, which eliminates the dissociative process. In addition, those resonances lie above 1 eV, above the energy range addressed in the DEA asymmetry experiments [12], although they give rise to broad peaks in the transmission asymmetry measurements [1, 50].

3.3.1 Molecular dynamics

The investigation of other physical aspects of the molecule can help us to have a better understanding about the experimental data. The elastic scattering calculations were performed in the fixed-nuclei approximation using the optimal ground-state structures of the target molecules. However, in a thermal gas the population of excited vibrational states is significant, which can result in a different energy (and width) of the resonances. The 3I bound state does not produce, in principle, resonances in vibrational excited states that would trigger the dissociation through the C-I stretch. Nevertheless, because the vertical bound energy is small in view of the thermical energy scale (see Table 3.1), it is possible that the bound state becomes a resonance in slightly different geometries.

A molecular dynamics study was carried out to obtain a conformational sampling of the possible geometries of the molecules. We performed a Born-Oppenheimer Molecular

Dynamics (BOMD) study for the electronic ground states of the isolated iodocamphor compounds at 353K. This simulation uses a classical molecular dynamics for the nuclei, where the energy and the electron density are computed from quantum mechanical electronic structure methods [51]. The simulations reproduced the gas of molecules at the same temperature used in the experiments of Dreiling *et al.* [12].

We employed the DFT method to describe the ground state using the PBE energy functional with the pseudopotential GTH-PBE, a DZVP basis set (for C, O and H), and a DZVP-MOLOPT-SR basis set for iodine, as implemented in the CP2K package [52]. The simulations used 70,000 steps with $\Delta t = 0.25$ fs, after 10,000 thermalization steps. The transient regime was identified analyzing the potential energy (Fig. 3.8a), although temperature and kinetic energy reach a stationary regime well before that. We obtained the auto-correlation function ($C(t)$) for potential energy (Fig. 3.8b). A total of 100 configurations equally spaced in time were obtained from the last 15 ps of the simulation, from which we evaluated the VBEs and scaled VO energies.

The configurations from the 3IC BOMD simulation indicate an oscillation around the equilibrium geometry. We considered the ensemble with 100 configurations to estimate the vertical energy for each geometry using M062X/aug-cc-pVDZ, as shown in Fig. 3.9a. **About** 24% **of them have positive vertical energies, corresponding to a resonance rather than a bound σ^* state**. This indicates that a significant population of molecules in the experiment may attach electrons around 0 eV, forming a σ^* resonance. This state would have a low energy (with a correspondingly narrow width), which could trigger dissociation and account for the DEA asymmetry observed experimentally. Moreover, VAE estimates for the π^* resonance shows this state remains in the same energy region, so that it does not contribute to asymmetry measurements.

The simulation for 10IC shows two representative configurations related to the dihedral angle of the CCCI moiety (see Fig. 3.9b), where the first one is the chiral carbon bonded to the oxygen. The dihedral angle has two typical values, which correspond to an iodine position nearest to the oxygen atom, and a distant position, similar to the optimal neutral ground state (Fig. 3.9b). We estimate about 33% of the total population in the first geometry. Despite the similar σ^* VAE in these two equilibrium geometries, the π^* resonance in the first configuration is more stable. Using the scaled VOE, its resonance energy decreases to 0.99 eV when compared to the previous value of 1.10 eV.

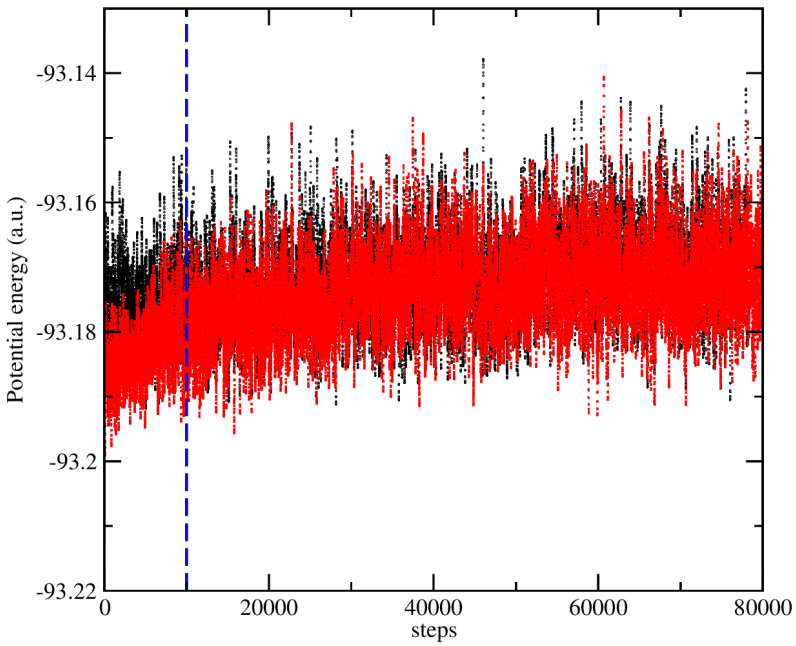

(a)

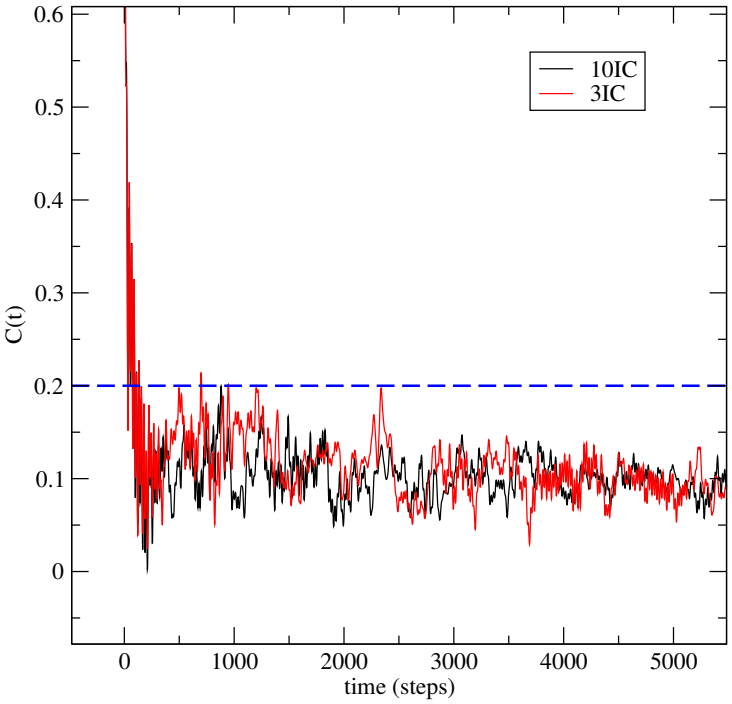

(b)

Figure 3.8: 3.8a: Potential energies (in atomic units), for 10IC (black) and 3IC (red). The blue dashed line represents the transient limit. 3.8b: The auto-correlation function for 10IC and 3IC. The blue dashed line shows a 20% auto-correlation.

Despite the stabilization of the π^* resonance, it may not significantly contribute to the DEA asymmetry below 0.6 eV [12].

With this investigation, we conclude that the 3IC σ^* anion state should trigger the dissociation process, but the situation is a little more complicated in this case. The formation of the vibrational bound state by electron attachment should be accompanied by unlikely vibrational transitions from eigenstates of the neutral molecule to the continuum of the anion, therefore suppressing the elastic cross section. Nonetheless, electron attachment can be considered a fast (vertical) process on the time scale of molecular vibrations, such that the formation of the σ^* resonance is possible for 3IC in principle, for short enough carbon-iodine bond lengths. Once formed, the σ^* state should undergo fast dissociation, since the potential energy surface is strongly repulsive along the reaction coordinate at the favorable attachment geometries; and the autoionization width is expected to be fairly small, since the most likely energies of the σ^* resonance are 0.1 eV.

Having established that, at the low energies of interest, DEA to the halocamphors should essentially arise from the σ^* resonances we can consider some aspects related to the dissociation dynamics. In view of the anti-bonding character of the σ^* states, the expected anion fragments would be X^- or $[M{-}X]^-$, where $X = Br, I$, and $[M{-}X]$ indicates the abstraction of the neutral halogen atom from the halocamphor molecule, such that $M = 3BrC, 3IC, 10IC$. While the experiments could not distinguish the anion fragments[53, 12], the carbon-halogen bonds can be viewed as the reaction coordinates. Here we addressed whether the main dissociation channel would produce X^- or $[M{-}X]^-$, by computing zero-temperature energy thresholds for each reaction. We employed the G4(MP2)[54] composite method for the case of 3BrC, which showed that the DEA signal observed below 0.6 eV should stem from the Br^- fragment (exothermic by -0.90 eV) but not from $[M{-}Br]^-$ (endothermic by 0.96 eV). Since the standard basis sets employed in the G4(MP2) protocol are not available for the iodine atom, for 3IC and 10IC we employed the DFT/B3LYP/aug-cc-pVDZ method to optimize the structures and DFT/M06-2X/aug-cc-pVDZ to evaluate the thresholds. The results indicate that the observed DEA signals also arise from I^- fragments (exothermic by -1.03 eV for 3IC and -0.71 eV for 10IC) rather than $[M{-}I]^-$ (endothermic by 1.49 eV for 3IC and 2.03 for 10IC).

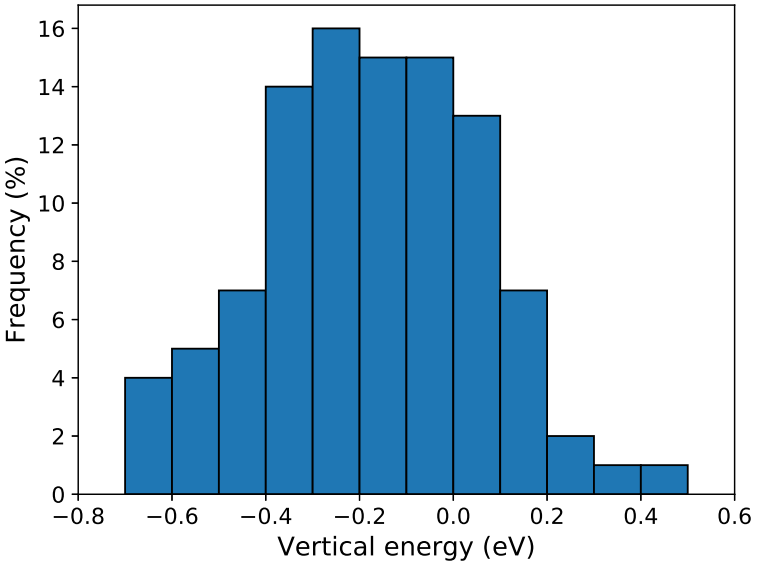

(a)

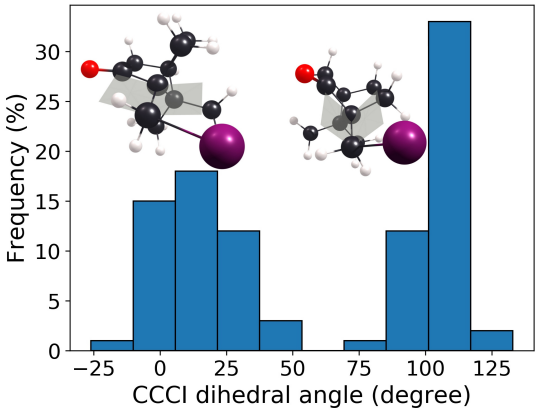

(b)

Figure 3.9: 3.9a: 3IC VAE non normalized histogram. 3.9b: CCCI dihedral angle histogram for 10IC.

Chapter 4

Transmission and DEA asymmetries

This chapter brings our results and discussion about the transmission and DEA asymmetries, obtained from applying the ECD theory formulated in Chapter 2 and the results from scattering calculations presented in Chapter 3. It is divided in two sections, where the first one concerns the transmission asymmetry. There, we obtain an estimated value for the spin-orbit coupling for 3BrC from the experimental data, and reproduce the transmission asymmetries for the iodocamphor species. In the subsequent section, we present the DEA asymmetry for 3BrC and 10IC considering two different approximations, and obtain a consistent relation of magnitude between them.

4.1 The transmission asymmetry

In this section, we discuss the evaluation of the transmission asymmetries for the halocamphor molecules. We applied the ECD formalism developed in Section 2.4, where we derive the expression (2.5.28) from the Feshbach operator formalism including the spin-orbit coupling. The transmission asymmetry is then expressed in the form

$$a_{trs}(P_0) \approx -\rho d P_0 \frac{(2\pi)^3}{E} \langle \mathrm{Re}[W^{0*}_{\boldsymbol{k_i}} U_{\boldsymbol{k_i}}] \rangle \frac{\Gamma_{res}}{(E - E_{res})^2 + (\frac{1}{2}\Gamma_{res})^2},$$

where P_0 is the spin polarization; ρ is the sample density and d is the sample thickness; E is the incident electron energy, E_{res} and Γ_{res} are the vertical resonance energy and width, respectively; $U_{\boldsymbol{k_i}}$ is the entry amplitude matrix element and $W^{0*}_{\boldsymbol{k_i}}$ is the spin-preserving component of the spin-orbit coupling amplitude. The expression above was derived under the following assumptions: (i) the fixed nuclei approximation; (ii) the operators $W^{0*}_{\boldsymbol{k_i}}$ and

$U_{\boldsymbol{k_i}}$ do not depend on energy and vibrational coordinates; (iii) the local approximation for the optical potential, that is, $V_{opt} \approx E_{res} - \frac{i}{2}\Gamma_{res}$; (iv) each structure in the transmission asymmetry arises from only one resonance, without any interference among resonance states. Our objective here is to present the results concerning the least-squares fit of eq. (2.5.28) to the 3BrC electron transmission data (figure 4.1), reported by Mayer and Kessler [1], and compare it with similar data obtained by Dreiling and Gay [50].

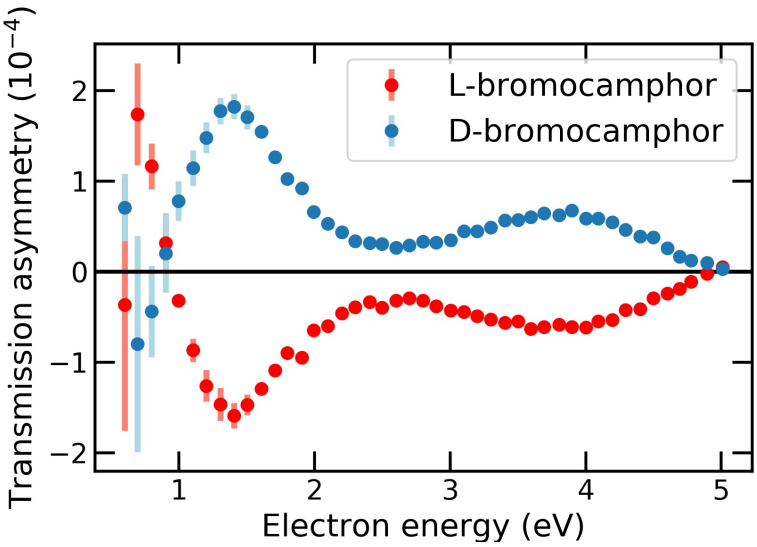

Figure 4.1: 3BrC transmission asymmetry data for the *L*- and *D*- species [1].

It should be clear that $W^0_{\boldsymbol{k_i}}$ is the object of interest, the matrix element that gives the order of magnitude for the asymmetry. Estimating a value for this amplitude is challenging and it is not feasible for us in this study. Nevertheless, we can obtain the quantity $\langle \mathrm{Re}[W^{0*}_{\boldsymbol{k_i}} U_{\boldsymbol{k_i}}] \rangle$ from the fit rather than $W^0_{\boldsymbol{k_i}}$. The quantity of interest can be written as

$$\langle \mathrm{Re}[W^{0*}_{\boldsymbol{k_i}} U_{\boldsymbol{k_i}}] \rangle = \frac{1}{4\pi} \int_{\Omega} d\Omega_{\boldsymbol{k_i}} |W^{0*}_{\boldsymbol{k_i}}||U_{\boldsymbol{k_i}}| \cos\delta(\boldsymbol{k_i}), \tag{4.1.1}$$

where $\delta(\boldsymbol{k_i})$ is the phase difference between $W^0_{\boldsymbol{k_i}}$ and $U_{\boldsymbol{k_i}}$. In the expression above, the average over target orientations in the laboratory-fixed frame (indicated by the brackets) is equivalent to an average over incident electron direction in the molecule-fixed frame. We consider the relation between Γ and $U_{\boldsymbol{k_i}}$ defined in eq. (2.5.13),

$$\Gamma(R, E) = 2\pi \int_{\Omega} d\hat{\boldsymbol{k}}_{\boldsymbol{i}} |U_{\boldsymbol{k_i}}|^2.$$

In view of eq. (2.5.13), we expect that $\langle \mathrm{Re}[W^{0*}_{\boldsymbol{k_i}} U_{\boldsymbol{k_i}}] \rangle$ scales with $\Gamma^{\frac{1}{2}}$, and can then estimate

the magnitude $\overline{W}$ of the spin-orbit coupling to evaluate

$$\overline{W} \equiv \frac{\langle \mathrm{Re}[W^{0*}_{\boldsymbol{k_i}} U_{\boldsymbol{k_i}}] \rangle}{\Gamma^{\frac{1}{2}}}. \tag{4.1.2}$$

Since we assume that Γ_{res} is expressed in the local approximation, $\langle \mathrm{Re}[W^{0*}_{\boldsymbol{k_i}} U_{\boldsymbol{k_i}}] \rangle$ can be taken as only one optimized parameter in the fitting. Additionally, Γ_{res} and E_{res} are adjusted to represent the width and energy position of the structure in the transmission asymmetry. This construction allows us to obtain the spin-orbit term apart from the Coulomb term, although it includes the relative phase between the spin-orbit and Coulomb terms. In this construction, we neglect the phase dependence on the energy, considering a fixed phase.

We must also take into account the experimental parameters, which are fundamental to comprehend the magnitude of the asymmetry. The electron beam employed in the Kessler transmission experiment had a 40% spin polarization asymmetry [1]. As we do not have detailed information about ρd, it is replaced for $\log\left(\frac{I}{I_0}\right)/Q_{tot}$ using the Beer-Lambert Law. The fraction $\frac{I}{I_0}$ is the transmitted/incident current ratio, which would be around 10%. The total cross section Q_{tot}, which, at the low energy of interest, can be reasonably approximated by the elastic integral cross section computed with the SMCPP method and the Born Closure approach [18].

Finally, the expression to be applied in the non-linear fit is given by

$$a_{trs}(E) = \frac{\log\left(\frac{I}{I_0}\right)}{Q_{tot}} P_0 \frac{(2\pi)^3}{E} \left[\sum_{res} \frac{\overline{W}\, \Gamma_{res}^{\frac{3}{2}}}{(E - E_{res})^2 + (\frac{1}{2}\Gamma_{res})^2} \right], \tag{4.1.3}$$

where the sum is over the resonant states, although neglecting any interference among them (sum over isolated resonances). We fit this expression for the total asymmetry data, that is, $A_{tot} = a_L - a_D$, and statistical uncertainties were obtained from $\sigma_{A_{tot}} = \sqrt{\sigma^2_{a_L} + \sigma^2_{a_D}}$, as usual in uncertainty propagation.

4.1.1 Transmission asymmetry fit

We considered, to perform the fit, the energy region between 1.0 eV and 2.6 eV, where a structure is found around 1.4 eV in the transmission asymmetry data. Here, we assumed this structure arises from the σ_2^* transient state, without any contribution from other res-

onances. The data below 1 eV is less accurate due to instrumental uncertainties [1], while above 2.6 eV the data suggests a structure with no clear correspondence to resonances in our calculations. The fitted curve for 3-bromocamphor A_{tot} in this region is presented in Figure 4.2. We obtained $\overline{W}_{\mathrm{Br}} = (5.0 \pm 0.6) \times 10^{-4}$ $(\mathrm{eV})^{1/2}$. We notice that $\overline{W}^2_{\mathrm{Br}}$ is about 10^{-7} eV, which is consistent with the preliminar assumption $\mathcal{O}(V^2_{SO}) \ll \mathcal{O}(V^2_C) \sim \Gamma$ considered in the formulation of the Feshbach formalism with spin-orbit coupling. The least-square fit fails to reproduce the experimental data when the energy is between 1.0 eV and 1.1 eV, in which the data goes to zero rapidly as close as the energy is 1 eV. The discrepancy between fitted curve and the data comes from the lower lying resonance contribution, which produces a well, rather than a peak, in the asymmetry data. since we are neglecting any contribution from other resonances, the expression is not designed to predict the data behaviour (we discuss more about it below). In spite of this, the fitted curve describes reasonably well the asymmetry above 1.1 eV.

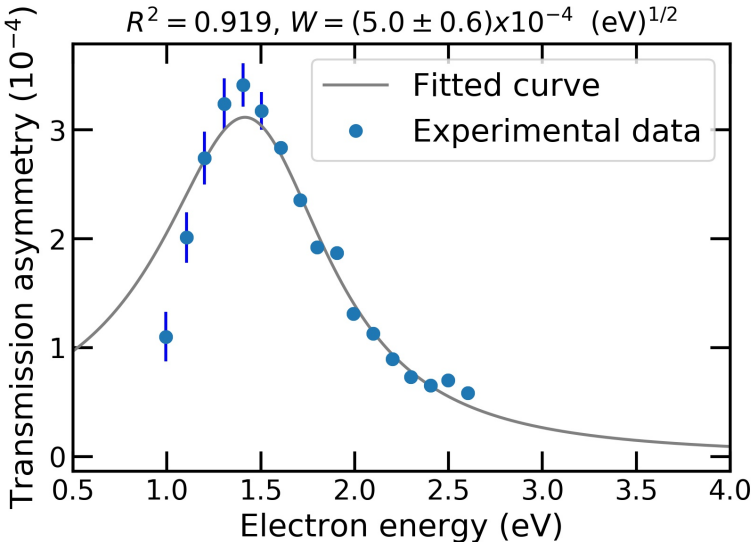

Figure 4.2: Least-squares fit of the model in eq. (4.1.3) to the transmission asymmetry data [1] for the 3BrC. The R^2 coefficient and the value of the $\overline{W}$ model parameter are shown on the top of the panel.

We assumed a proportionality between $\overline{W}_{\mathrm{I}}$ and $\overline{W}_{\mathrm{Br}}$ based on the expected dependence of the Mott-scattering asymmetry on the atomic numbers [11], i.e, $\overline{W}_{\mathrm{I}} = (Z^2_{\mathrm{I}}/Z^2_{\mathrm{Br}})\overline{W}_{\mathrm{Br}}$. As a result, we obtained $(11.5 \pm 1.4) \times 10^{-4}$ $(\mathrm{eV})^{1/2}$ for $\overline{W}_{\mathrm{I}}$. We used the result of the least-squares fit to estimate the transmission asymmetries for the iodocamphor isomers and the scaling of the SO interaction with respect to the atomic number. A comparison between asymmetries for the halocamphors is presented in Fig. 4.3. We also compared

our results with those obtained by the Nebraska group [50]. Their data were taken with a different set up from the Münster group, including different spin polarization (30%), electron beam attenuation (70%) and electron beam energy resolution (0.3 eV). We therefore standardized the 3BrC data in order to compare them. The Münster results were rescaled according to the polarization and attenuation employed by the Nebraska group applying

$$A_{tot}^{std} = A_{tot}\left(\frac{0.3}{0.4}\right)\left(\frac{\log(0.3)}{\log(0.1)}\right), \tag{4.1.4}$$

where the first and second parenthetical terms account for the corrections in polarization and attenuation, respectively. Finally, the results were convoluted, employing the expression

$$A_{tot}^{\text{conv}}(E) = \int_0^\infty dE' f(E' - E) A_{tot}^{std}(E) \tag{4.1.5}$$

to account for differences from the electron-beam energy resolution. In the expression above, $f(E' - E)$ is the energy distribution of the electron beam, which has typically a Gaussian profile. It is worth to mentioning that the 3BrC data obtained by the Nebraska group is consistent with those obtained by the Münster group, which only differ in magnitude due to these different experimental parameters [55]. The calculated transmission asymmetries for 3BrC, 3IC and 10IC were also rescaled and convoluted according to eqs. (4.1.4) and (4.1.5), in order to be compared with the experimental data obtained by Dreiling *et al* [50].

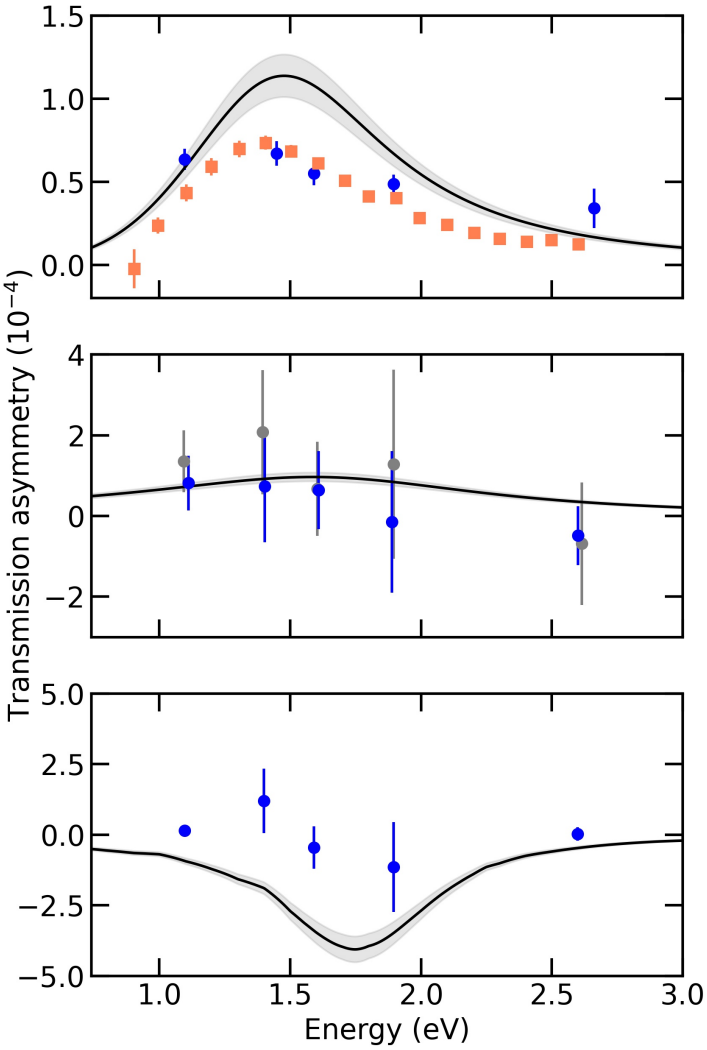

Figure 4.3: Convoluted transmission asymmetries calculated for 3-bromocamphor (top panel) and 3IC (central panel) and 10IC (bottom panel). The shaded areas indicates their standard deviation. Experimental data by the Nebraska group [50] are represented as blue circles, and the grey circles in the center panel represent similar data with reversed sign. The 3-bromocamphor data by the Münster group [1] are represented as orange squares.

The rescaled and convoluted asymmetries obtained for the halocamphor molecules are **in qualitative agreement with the experimental data**. The agreement between the magnitude of the calculated asymmetries and the experimental data indicates our model, although simplified, is able to predict reasonably well the chiral sensitivity, since the elastic integral cross section and the resonance parameters are sufficiently well described. As one can notice in the top panel of Fig. 4.3, the calculated asymmetry for 3BrC is

overestimated in relation to both data sets. This difference comes from the convolution process, in which the original calculated transmission asymmetry is overestimated close to 1 eV (see Fig. 4.2). The overlap between the overestimated asymmetry and the energy distribution $f(E' - E)$ in this energy region is significant and its contribution is systematically summed along the convolution integral. Similar behavior can occur for the calculated 10IC asymmetry, in which the result is overestimated compared to experimental data. On the other hand, the small amount of data reported for 3IC and 10IC in the resonance energy region, as well as the energy resolution (about 0.3 eV) close to the resonance widths, restrict us to a qualitative discussion concerning the iodocamphor transmission asymmetries. The ratio of the maximum calculated asymmetry for 10IC and 3BrC (estimated at 3.6) is also consistent with the experimental one (between 1.8 and 4.2), therefore the overestimated calculated asymmetries do not compromise our investigation.

When we inspect the data by Munster group, it is clear that the asymmetry changes sign below 1 eV. This could occur due to a different phase $\delta(\boldsymbol{k})$ in the energy region of the σ_1^* resonance, providing a structure with a well profile at around 0.7 eV. Similarly, a sign change is also noted in the DEA asymmetry for 3BrC, but with energy below 0.5 eV (see Fig. 1.7). The energy dependent phase factor between $W^0_{\boldsymbol{k_i}}$ and $U_{\boldsymbol{k_i}}$, given in eq. (4.1.1), could account for the change in sign. More generally, the phase difference between the resonant and the background terms can affect the cross section (and therefore, the asymmetry) dependence on the energy, producing peaks or wells. As a first approximation, we could consider a fixed phase for energies above 1 eV that corresponds to a positive $\overline{W}$, while the phase for energies below 1 eV corresponds to $-\overline{W}$. From this simple model, we estimate the transmission asymmetry for energies below 1 eV, presented in Figure 4.4. We evaluated eq. (4.1.3) with the obtained $\overline{W}$ for the iodine and bromine atoms, as well as the energy and width of the first resonance for both 3BrC and 10IC, given in Table 3.1. The asymmetries were obtained with the same experimental parameters employed by the Nebraska group, and were convoluted as described above. We estimate the 10IC maximum asymmetry is about twice the 3BrC maximum asymmetry, which indicates the magnitude of asymmetry should depend not only on the spin-orbit coupling, but also on the resonance position and width. The experimental data are significantly less accurate below 1 eV, so any interpretation about the results would be just a conjecture, without experimental data to support the arguments. Even so, our results are useful for the DEA

asymmetry calculation, discussed in the next section.

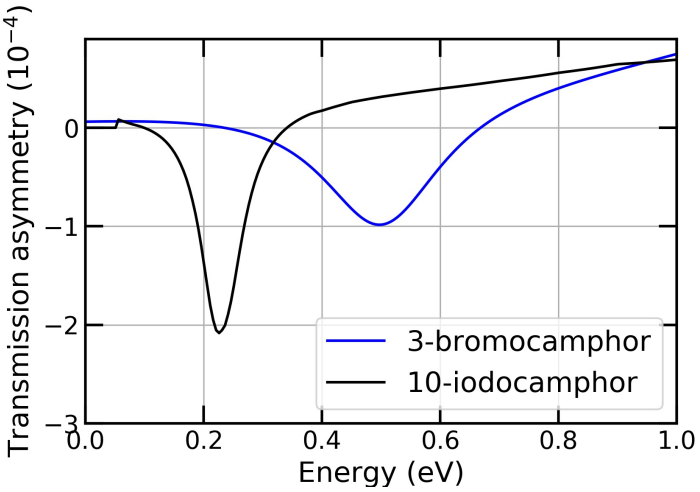

Figure 4.4: Calculated transmission asymmetry for 3-bromocamphor and 10-iodocamphor, for energies below 1 eV.

4.2 DEA asymmetry

As discussed in Section 2.4, the ECD formalism also allows us to derive the expression for the DEA asymmetry in eq. (2.4.30), reproduced below:

$$A_{DEA} = 0.3\,[\alpha_{DEA} + 0.69 a_{tot}]. \tag{4.2.1}$$

The expression above was obtained from the spin polarization ($\sim 30\%$) and beam attenuation ($\sim 50\%$) used in the experiments of the Nebraska group [53, 12]. In the expression above, a_{tot} is the total scattering asymmetry,

$$a_{tot} = \frac{Q^{+}_{tot} - Q^{-}_{tot}}{Q^{+}_{tot} + Q^{-}_{tot}} \equiv \frac{\Delta Q_{tot}}{Q_{tot}}, \tag{4.2.2}$$

which can be associated with the transmission asymmetry discussed in the previous section,

$$a_{trs} = P_0 \rho d \Delta Q_{tot} \Rightarrow \frac{\Delta Q_{tot}}{Q_{tot}} = \frac{a_{trs}}{P_0 \log\left(\frac{I}{I_0}\right)}, \tag{4.2.3}$$

by using the Beer-Lambert Law. The other term in eq. (4.2.1) is the dissociation probability asymmetry, α_{DEA}, which can be approximated as

$$\alpha_{DEA} = \frac{(Q^+_{DEA}/Q^+_{tot}) - (Q^-_{DEA}/Q^-_{tot})}{(Q^+_{DEA}/Q^+_{tot}) + (Q^-_{DEA}/Q^-_{tot})} \approx \frac{Q^+_{DEA} - Q^-_{DEA}}{Q^+_{DEA} + Q^-_{DEA}} \equiv a_{DEA}, \tag{4.2.4}$$

since $Q^+_{tot}/Q^-_{tot} \approx 1$. We remember that $Q^\pm_{DEA}$ is the dissociation cross section, and $\pm$ indicate the longitudinal projections of the incident electron spin. We assume the total cross sections to be averaged over the molecular orientations, therefore it does not depend on $\hat{\boldsymbol{k}}_{\boldsymbol{i}}$. The spin-dependent DEA cross section $Q^\pm_{DEA}$ can be obtained from the Feshbach formalism, as shown in Section 2.5. It is expressed as

$$Q^\pm_{DEA} = \frac{2\pi^3}{E}|T^\pm_{DEA}|^2, \tag{4.2.5}$$

where $T^\pm_{DEA}$ is the DEA scattering amplitude with the spin-orbit coupling included. Therefore, estimating the DEA scattering amplitude is required to compute the DEA asymmetry.

Let us consider the pseudo-diatomic model, as proposed earlier, where all vibrational coordinates but the reactive coordinate C–X bond are kept fixed. In this case, the T-matrix element for the C–X bond breaking DEA reaction can be expressed as

$$\begin{aligned} T^\pm_{DEA} \approx \left(\frac{\mu}{K}\right)^{1/2} \lim_{R\to\infty} e^{iKR}\Bigg[&\langle R|\frac{1}{E - T_{nuc} - V^{(+)}_{opt}} U_{\boldsymbol{k}_{\boldsymbol{i}}}|\nu_i\rangle \\ &\pm \langle R|\frac{1}{E - T_{nuc} - V^{(+)}_{opt}} W^0_{\boldsymbol{k}_{\boldsymbol{i}}}|\nu_i\rangle\Bigg] \equiv T_0 \pm T_1, \end{aligned} \tag{4.2.6}$$

where μ, R, K are the reduced mass of the products, the reaction coordinate and its linear moment, respectively, and T_{nuc} is the nuclear kinetic energy operator. The above expression combined with eq. (4.2.5) gives

$$a_{DEA} = \frac{2\,\mathrm{Re}(T_1^*\ T_0)}{|T_0|^2 + |T_1|^2}. \tag{4.2.7}$$

The two A_{DEA} components a_{DEA} and a_{trs} come from the fragment and electron currents, respectively, where the first should be the largest one. We expect a_{DEA} about 10^{-3} for a DEA asymmetry around 10^{-4}, while a_{trs} is about 10^{-4} according to the experimental data. In the following, we evaluate a_{DEA} for 3-bromocamphor and 10-iodocamphor

in two different ways. The first one employs the Condon approximation, which could be viewed as questionable, but provides qualitatively correct information on the asymmetry ratio for 3BrC and 10IC from inexpensive calculations. The second one is based on more elaborate DEA simulations, along the lines of studies reported by W. Domcke and coworkers [40, 56]. We do not present results for 3-iodocamphor since the fact that the σ^* resonance is vertically bound for 3IC makes the DEA models more complicated for this system (see below). We believe our main conclusions can be drawn from the comparison between 3BrC and 10IC.

4.2.1 Condon approximation

We propose a simple approximation to obtain a first estimate for the DEA scattering amplitude. We invoke the Condon approximation, in the sense of the electronic transitions, and therefore the operators $W^0_{\boldsymbol{k_i}}$ and $U^0_{\boldsymbol{k_i}}$ are assumed vertical, and thus independent of nuclear positions. This means that $W^0_{\boldsymbol{k_i}}$ and $U^0_{\boldsymbol{k_i}}$ are just complex numbers, denoted as U and W, and do not depend on the energy or the reaction coordinate. This way, $T^{\pm}_{DEA}$ becomes

$$\begin{aligned} T^{\pm(\text{Condon})}_{DEA} &= \left(\frac{\mu}{K}\right)^{1/2} \lim_{R\to\infty} e^{iKR}\left[U\langle R|\frac{1}{E-T_{nuc}-V^{(+)}_{opt}}|\nu_i\rangle \pm W\langle R|\frac{1}{E-T_{nuc}-V^{(+)}_{opt}}|\nu_i\rangle\right] \\ &= \left(\frac{\mu}{K}\right)^{1/2} (U\pm W) \lim_{R\to\infty} e^{iKR}\left[\langle R|\frac{1}{E-T_{nuc}-V^{(+)}_{opt}}|\nu_i\rangle\right], \end{aligned} \tag{4.2.8}$$

such that eq. (4.2.7) simplifies to

$$a^{(\text{Condon})}_{DEA} = \frac{2\,\text{Re}(W^*U)}{|U|^2+|W|^2}. \tag{4.2.9}$$

In the expression above, the numerator is identified as the quantity $\langle \text{Re}[W^{0*}_{\boldsymbol{k_i}} U_{\boldsymbol{k_i}}]\rangle$ which could be obtained from the transmission asymmetry fit and associated to eq. (4.1.2), as discussed in the last section. In the denominator, the term $|U|^2$ is related to Γ as expressed in equation (2.5.13). Therefore, the resonance width is predominant in the denominator as it is significantly larger than $|W|^2$. The quantity a_{DEA} in the Condon approximation becomes

$$a_{DEA}^{(\mathrm{Condon})} = 4\pi\overline{W}\Gamma^{-\frac{1}{2}}, \tag{4.2.10}$$

which does not depend on the collision energy, since Γ and $\overline{W}$ are described in the local approximation. As a consequence, the approximation does not describe the energy dependence of the dissociation asymmetries, but it can provide crude upper bounds values for a_{DEA} and, consequently, for the DEA asymmetry A_{DEA}.

Table 4.1 presents the values for $\overline{W}$ and Γ, as well as $a_{DEA}^{(\mathrm{Condon})}$ obtained with eq. (4.2.10) for 3-bromocamphor and 10-iodocamphor. We employed the widths of the first resonances (σ_1^* for 3BrC and the σ^* for 10IC) obtained from the SMCPP calculations. The DEA asymmetry in the Condon approximation was obtained employing eq. (4.2.1). We used the maximum values of a_{tot} from eq. (4.2.3) and from the transmission asymmetries calculated in the previous section (Fig. 4.4). Table 4.2 presents the components $a_{DEA}^{(\mathrm{Condon})}$ and a_{tot}, and compares the values of $A_{DEA}^{(\mathrm{Condon})}$ with the maximum DEA asymmetries experimentally observed [12].

Table 4.1: Values for $\overline{W}$, the σ^* resonances widths Γ (in eV), and a_{DEA} obtained in the Condon approximation.

	$\overline{W}(10^{-4})$	Γ	$a_{DEA}^{(\mathrm{Condon})}$	$(\times 10^{-4})$
3-bromocamphor	5.0	0.126	177	
10-iodocamphor	11.5	0.037	749	

Table 4.2: Values for A_{DEA} and its components in the Condon approximation (multiplied by 10^4). Observed maximum DEA asymmetries [12] are also shown for comparison.

	$a_{DEA}^{(\mathrm{Condon})}$	$a_{tot}^{(max)}$	$A_{DEA}^{(\mathrm{Condon})}$	$A_{DEA}^{(\mathrm{exp})}$	$(\times 10^4)$
3-bromocamphor	177	2.8	54	4	
10-iodocamphor	749	5.5	226	16	

Firstly, we would like to discuss the DEA asymmetry ratio between 3-bromocamphor and 10-iodocamphor. We note in Table 4.1 that the ratio for our calculations is consistent with those noted by Drailing and Gay. The agreement can be understood since $\overline{W}_{\mathrm{I}}$ is about twice $\overline{W}_{\mathrm{Br}}$ while **the resonance width for 3BrC is about three times the one for 10IC**. When these values are combined as it is shown in eq. (4.2.10) and (4.2.3), the 10IC/3BrC asymmetry ratio is evaluated as 4.2, in good agreement with those obtained

experimentally. The calculated DEA asymmetries are overestimated with respect to the experimental data by one order of magnitude. The discrepancy in the absolute A_{DEA} values arises from the many approximations underlying the results in Table 4.1: (i) the parameter $\overline{W}$ obtained from the fit is overestimated, as discussed in the previous section and noted in Fig. 4.3; (ii) the relative phase between $W^0_{\boldsymbol{k_i}}$ and $U^0_{\boldsymbol{k_i}}$ for the σ^* resonances was neglected. As we do not have any information to check this quantity, the term $\langle \mathrm{Re}[W^{0*}_{\boldsymbol{k_i}} U_{\boldsymbol{k_i}}] \rangle$ could be significantly smaller.

As already pointed out, the Condon approximation only provides a rough estimate for A_{DEA}. To obtain more accurate values it is necessary to consider dissociative dynamics accounting for a potential energy curve along the reaction coordinate for the anion states, along with the geometry dependence of the resonance width as the vibrational wave packet evolves in time.

4.2.2 Dissociative dynamics of the transient anion

We propose a time-dependent approach to describe the dissociative electron attachment dynamics. The methodology is based on by studies developed by Domcke and co-workers [24, 40, 56, 57], in which the time-dependent wavefunction description contains the complete information on all resonant scattering amplitudes. Our contribution in this study is the inclusion of the spin-orbit coupling in the dynamics to obtain the energy-dependent scattering amplitude matrices T_0 and T_1.

Theoretical Background

The TNI time-dependent wave package (WP) evolves according to the projected equation of motion (EOM) onto the diabatic discrete space Q. The WP propagation is evaluated employing the local approximation (see eq. (2.5.14)), and the EOM is written as [57]

$$i\frac{\partial}{\partial t}\xi_d^{(+)}(R,t) = \left[T_N + V_r(R) + \Delta_L(R) - \frac{i}{2}\Gamma_L(R)\right]\xi_d^{(+)}(R,t), \tag{4.2.11}$$

where $\xi_d^{(+)}(R,t)$ is the anionic state projected on Q in the $R-$space, as presented in eq. (2.5.16). In this case, $\xi_d^{(+)}$ depends on the reaction coordinate R since the pseudo-diatomic model is employed. The optical potential in the local approximation has the real component $V_r(R)$ represented by the anionic potential energy curve (PEC), responsible for

the WP propagation. The imaginary component is given by $V_i = \frac{\Gamma_L(R)}{2}$, accounting for the autoionization. Ideally, the description of $\Gamma_L(R)$ requires several solutions for the scattering problem, mapping the autoionization in different reaction coordinate values. Performing several scattering calculations for the halocamphors is computationally demanding. Rather than do this, we employed an alternative fashion to account for the spatial dependence of the autoionization [58], given by

$$\Gamma_L(R) = [V_r(R) - V_0(R)]\frac{\Gamma_0}{E_0}, \tag{4.2.12}$$

where $V_0(R)$ is the neutral ground state PEC, Γ_0 is the vertical resonance width and E_0 is the vertical resonance energy.

For our proposes, the initial condition of the WP is the formation of the TNI state, when the neutral vibrational ground state $|\nu_i = 0\rangle$ couples with the continuum of the incident electron. Usually, electron attachment and detachment are mediated only through $U_{\boldsymbol{k}}$, but in our model it also occurs mediated through $W^0_{\boldsymbol{k_i}}$. Thus, the electron attachment forms two anionic states simultaneously,

$$\xi_d^{(0)}(R, t = 0) = U_{\boldsymbol{k}_i}\nu_0(R) \tag{4.2.13}$$

and

$$\xi_d^{(1)}(R, t = 0) = W^0_{\boldsymbol{k}_i}\nu_0(R), \tag{4.2.14}$$

where $\nu_0(R) = \langle R|\nu_i = 0\rangle$. As it was employed for the WP propagation, we can use the local width to account for the probability of attachment and autodetachment. In this approximation, which is called local-complex-potential (LCP) approximation [59], eq. (2.5.13) becomes

$$\Gamma_L(R) = \Gamma(R, E(R)) = 2\pi \int d\Omega_{\boldsymbol{k_i}} |U_{\boldsymbol{k_i}}|^2. \tag{4.2.15}$$

The initial condition is then given by

$$\xi_d^{(0)}(R, 0) = \left[\frac{\Gamma_L(R)}{2\pi}\right]^{\frac{1}{2}} \nu_0(R) \tag{4.2.16}$$

and

$$\xi_d^{(1)}(R,0) = \overline{W}\nu_0(R), \tag{4.2.17}$$

where the average over target orientation in the laboratory-fixed frame (or over incident electron direction in the fixed-molecule frame) is assumed. In the same sense, $\overline{W}$ is employed rather than the spin-orbit term $W^0_{\boldsymbol{k}_i}$, according to eq. (4.1.2). The DEA scattering amplitude in the LCP approximation is then written as

$$T_{DEA}^{(\mathrm{LCP})} = \left(\frac{K}{2\pi\mu}\right)^{\frac{1}{2}} \lim_{R\to\infty} e^{-iKR}\left[\int_0^\infty dt\, \xi_d^{(0)}(R,t)e^{-iEt} + \int_0^\infty dt\, \xi_d^{(1)}(R,t)e^{-iEt}\right], \tag{4.2.18}$$

where the WP has evolved sufficiently in time ($t \to \infty$), and the reaction products are sufficiently separated ($R \to \infty$). LCP produces adequate results to calculate DEA and inelastic vibrational cross sections, similar to those obtained with full nonlocal descriptions, as long as the resonance width is sharp and the resonance position is sufficiently far from the collision threshold. Nevertheless, LCP tends to overestimate the cross sections when the resonance width overlaps the collision threshold [60]. One can improve the description of the WP dynamics using a semi-local approximation [40, 57], which preserves the energy-dependence of the resonance width $\Gamma(R,E)$ in the attachment and autodetachment probabilities. In the semi-LCP approximation, the separability of the energy and R dependence of Γ it is assumed:

$$\Gamma(R,E) = \gamma(E)\Gamma_L(R), \tag{4.2.19}$$

where $\gamma(E)$ accounts for the continuum $N+1$ electron and the discrete neutral state coupling.

The Coulomb and spin-orbit potentials are not dependent on the collision energy, which is only accounted for in the continuum component of WP. Since the spin-orbit potential is significantly smaller than the Coulombic one, this component should be essentially the same for $\xi_d^{(0)}(R,t)$ and $\xi_d^{(1)}(R,t)$, and accounted for $\gamma(E)$. We define a modified WP $\widetilde{\xi}(R,t)$ with an energy-independent initial condition to be propagated, while the WP on an instant t carries the energy-dependent autoionization probability [57]. Thus, the

spin-orbit independent component of WP is written as

$$\widetilde{\xi}_d^{(0)}(R,t) = \left[\frac{\gamma(E)}{2\pi}\right]^{-\frac{1}{2}} \xi_d^{(0)}(R,t). \tag{4.2.20}$$

with the initial condition

$$\widetilde{\xi}_d^{(0)}(R,0) = g(R)\xi_d^{(0)}(R,t). \tag{4.2.21}$$

In the same sense, we modify the spin-orbit term to account for the energy-dependent autodetachment probability,

$$\widetilde{W}(E) = \overline{W}\frac{\gamma(E)}{\gamma(E_0)}, \tag{4.2.22}$$

which becomes to $\overline{W}$ when the electron attachment is the vertical energy E_0, restoring those employed in the previous results.

For low-energy resonances, and specially the shape-type, the energy dependence of Γ is strongly governed by Wigner's threshold law [61]. We parametrize $\gamma(E)$ in accordance with the threshold law [57] as

$$\Gamma(E) = A(E/B)^{l+\frac{1}{2}}\exp(-E/B), \tag{4.2.23}$$

where l represents the lowest partial wave into which the resonance can decay, which we consider to be s-wave. The parameters A and B were obtained from least-squared fits of Breit-Wigner profiles $\delta_{sum}(E) = \delta_{res}(E) + \delta_{bg}(E)$ to the eigenphase sums, calculated with SMCPP methodology. We employ the parameterisation $\delta_{res} = -\text{atan}[\gamma(E)/2(E - E_{res})]$, and second-degree polynomials to model the background components $\delta_{bg}(E)$. The DEA scattering amplitude in the semi-LCP approximation is obtained as

$$\begin{aligned} T_{DEA}^{(\text{semi-LCP})} = \left[\frac{\gamma(E)K}{4\pi^2\mu}\right]^{\frac{1}{2}} \lim_{R\to\infty} e^{-iKR}\Bigg[\int_0^\infty dt\, \widetilde{\xi}_d^{(0)}(R,t)e^{-iEt} \\ + \int_0^\infty dt\, \widetilde{\xi}_d^{(1)}(R,t)e^{-iEt}\Bigg]. \end{aligned} \tag{4.2.24}$$

Once $T_{DEA}^{(\text{LCP})}$ and $T_{DEA}^{(\text{semi-LCP})}$ are evaluated, we are able to obtain the DEA cross section Q_{DEA}, as well as a_{DEA}, in both LCP and semi-LCP approximations, through the equations (4.2.5) and (4.2.7), respectively.

Below we present the model for the potential energy curves, the the disosciative dy-

namics results, the comparison of DEA cross sections in the two approximations and, finally, the convoluted DEA asymmetry for 3-bromocamphor and 10-iodocamphor.

Dynamics Calculation

A harmonic potential was employed for the neutral PECs $V_0(R)$ and a single-exponential dissociative curve for the anion PECs. We performed subsequent bond state calculations for different C-X bond lengths (rigid scan), which for each bond stretching we employed the DFT/M06-2X method with the aug-cc-pVDZ basis set. The curve parameters were obtained employing least-square fits to the rigid scan results. PECs were constructed with 16,384 points in the spatial grid and a 0.002 Angstrom step. The fitted curves and results from quantum calculations are shown in Fig. 4.5 for both molecules.

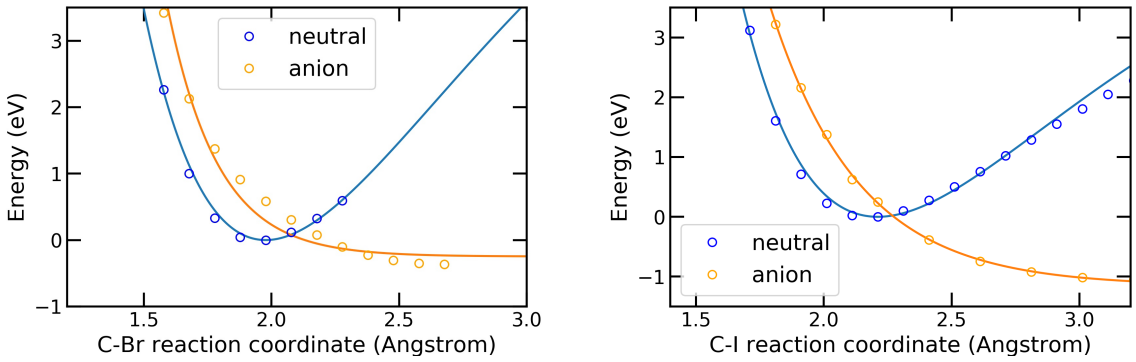

(a) (b)

Figure 4.5: PECs obtained from least-square fit to energies of neutral and anion states. Circles represent the energy states (in eV) obtained employing M06-2X/aug-cc-pVDZ methodology. The left panel contains the results for 3BrC, while the right panel shows the results for 10IC.

The WP was propagated employing a split-operator algorithm with a Fast Fourier Transform (FFT) algorithm with 32,768 discrete points in the time grid, and a time-step of 0.6 fs. The exponential curves obtained for the anion states represent the real component of the optical potential in the LCP approximation, while the imaginary component is obtained by eq. (4.2.12). The real and imaginary components of the optical potential are shown in Fig. 4.6, as well as the neutral PEC, for both molecules, along with the region representing a bound state regime. For bond lengths larger than a specific value, the neutral PECs have energy above their correspondings real components, characterizing anionic bound states. When the state becomes stable, the imaginary component vanishes,

and the molecule dissociates.

Analyzing real and imaginary components allows us to predict a larger DEA cross section for 10IC, compared with 3BrC, since the dissociative process concerns the competition between the autoionization (WP population decay) and energy stability of the fragmented molecule state. The real component shows how fast the WP tends to move towards dissociation the dissociation process, where more steep curves imply more repulsive potentials. Thus, comparing the real components of the two molecules, it is expected that 10IC dissociates faster than 3BrC. In turn, since the imaginary component is responsible for the WP population decay, the smaller its magnitude is, the larger the WP survival probability, therefore 10IC WP has a higher probability to survive during the WP propagation until it becomes stable.

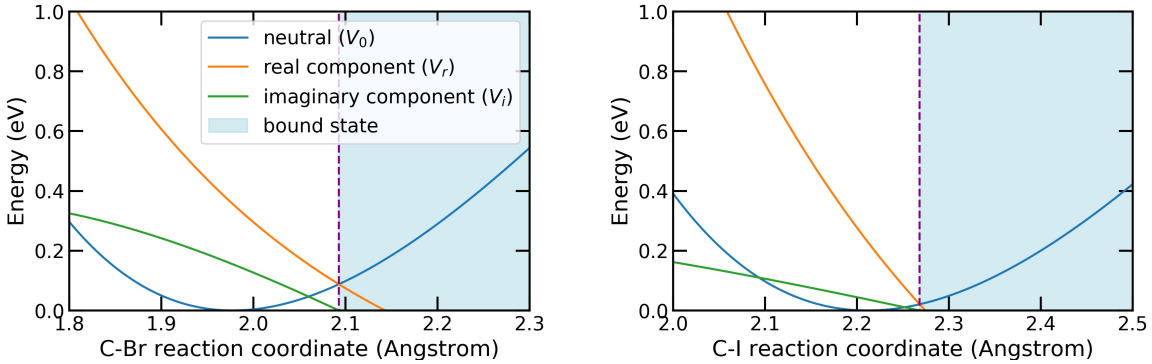

(a) (b)

Figure 4.6: Real and imaginary components of the optical potential in the local approximation, and the neutral PEC for comparison. The shaded area indicates the region where the anion state is bound. Left panel contains the curves for 3BrC, while the right panel presents the curves for 10IC.

Fig. 4.8 presents the results of the dynamics calculations for both molecules. Fig. 4.7a and 4.7b show the evolution of the squared modulus of WP during the first 40 fs. We observe that the magnitude of the 10IC WP is consistently larger than the 3BrC WP in all time instants, which confirms the WP survival probability is larger for 10IC. Fig 4.8a shows a comparison between the expectation value of the reaction coordinates $\langle \xi_d^{(+)}(R,t)|R|\xi_d^{(+)}(R,t)\rangle$. Our results show that 3BrC dissociates after about 20 fs, while 10IC presents a faster process, at about 15 fs. Fig 4.8b presents the DEA cross section obtained in both LCP and semi-LCP approximations. The DEA cross sections obtained in LCP approximation are five times larger than the cross sections obtained with the

semi-LCP approximation, indicating the overlaps between resonance width and energy resonance threshold is significant. Even so, 10IC DEA cross section magnitudes are about three times higher than the 3BrC DEA cross sections, in both LCP and semi-LCP approximation, confirming that 10IC produces more ion fragments than 3BrC.

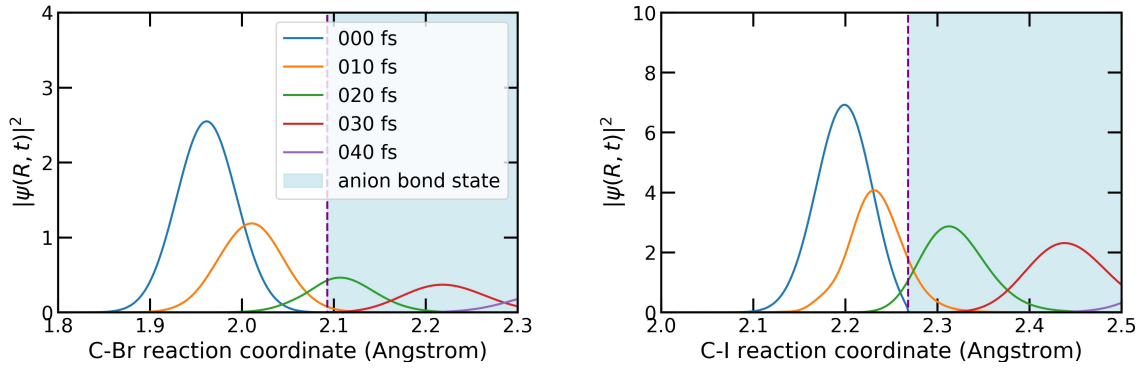

(a) (b)

Figure 4.7: Evolution of probabilities (squared modulus of the WPs) in the first 40 fs. The shaded areas indicates the anionic bound state region. The left panel shows the curves for 3BrC, while the right panel presents the curves for 10IC.

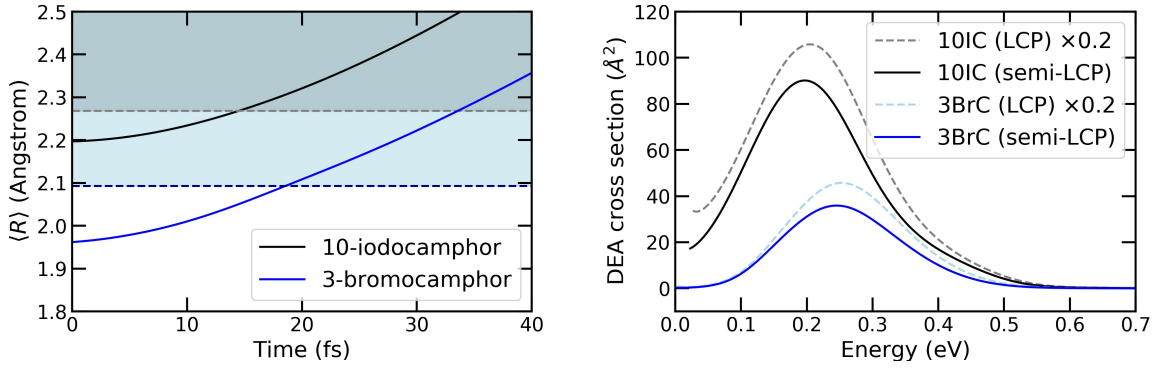

(a) (b)

Figure 4.8: Results of the dynamics calculation for 3-bromocamphor and 10-iodocamphor. Top panels show the evolution of probabilities (squared modulus of WP) for the first 40 fs. Top-left panel shows the curves for 3BrC, while the top-right panel presents the curves for 10IC. The shaded region indicates the anionic bound state region. Bottom panels show the results obtained employing the LCP and semi-LCP approximations. Bottom-left panel: Averaged trajectory of WP in time for 3BrC and 10IC. The blue and gray segmented lines(3BrC and 10IC, respectively) represent the threshold for the bound states. Bottom-right panel: DEA cross sections in the LCP approximation rescaled by 0.2 (segmented lines) compared with the semi-LCP approximation (full lines).

Dissociation asymmetry

The inclusion of the SO coupling in the dynamics allows us to calculate a_{DEA} energy dependence, as well as the DEA asymmetry according to eq. (4.2.7). Calculated a_{DEA} obtained with LCP and semi-LCP approximations are presented in Fig 4.9, for both molecules. The results obtained with LCP consistently present smaller magnitudes, since $|T_0|$ in the denominator is systematically larger in this approximation than in the semi-LCP approximation, as shown in Fig 4.8b. The quantity a_{DEA} represents to be major component in the DEA asymmetry and is estimated, in the LCP approximation, from 10 to 100 times larger than the transmission electron component a_{trs}. The results for 10IC are systematically larger than those for 3BrC (three to four times), which is consistent with the ratio observed in the experimental results [12]. However they are systematically above the expected magnitude. Based on the maximum magnitudes observed experimentally, 4×10^{-4} for 3BrC and 16×10^{-4} for 10IC, and the spin polarization employed (30%), we would be expect a_{DEA} up to 13×10^{-4} and 53×10^{-4} for 3BrC and 10IC, respectively. The magnitude of the calculated results are 5 times larger in LCP and 10 times larger in semi-LCP. The calculated a_{DEA} has a maximum magnitude at 0 eV, decreasing as the collision energy increases. The calculated a_{DEA} is minimal near the threshold energy of the indirect dissociation process (TNI formation in the π^* and internal combination to σ^*). Close to this energy (about 0.7 eV, see Chapter 3) the DEA cross section goes to zero (T_0 and $T_1 \sim 0$), and the unlikely fragment production implies small asymmetry. For energies close to 0 eV the DEA scattering amplitude T_0 tends to zero, as we observe the calculated DEA cross section in Fig. 4.8b. However, the DEA scattering amplitude T_1 tends to zero less dramatically than T_0, resulting in a non-zero asymmetry for nearly-zero energy of electron impact. Small variations in the denominator (essentially $|T_0|^2$) produce spurious structures in the curves, mainly in 10IC. These structures come from numerical instabilities during the WP propagation due to the time step size and spatial grid. More refined time and space grids were tested to obtain smoother curves, but the computational cost increases exponentially since FFT requires grids proportional to a power of 2. Although the improvement of the numerical model would significantly increase the computational effort, it would not be expected to modify our conclusions.

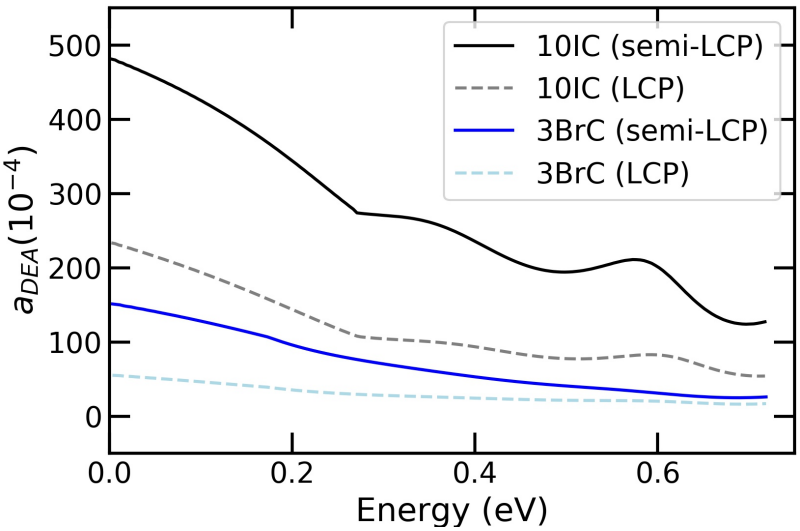

Figure 4.9: a_{DEA} asymmetry calculated in the LCP (segmented lines) and semi-LCP (full lines) approximations, for 3BrC (blue lines) and 10IC (black lines).

We convoluted the a_{DEA} obtained with LCP using the same experimental parameters applied in section 4.1. The convoluted A_{DEA} is obtained from the summed components a_{trs} and a_{DEA} according to eq. (4.2.1) and compared with the experimental results reported by Dreiling and Gay in Fig 4.10. Although the present results are overestimated compared to the experimental data, the ratio of the maximum calculated asymmetry for 10IC and 3BrC is 4.0, in good agreement with the reported by Dreiling and Gay. **We conclude that the TNI lifetime, the energy of attachment and the typical dissociation times, characteristics of the electron attachment and the dissociation dynamics, are preponderant on the DEA asymmetry, and not only the spin-orbit coupling strength, which scales as Z^2.** Our main contribution in this study is hopefully helping to answer "why the DEA asymmetry for 10IC is anomalously larger than for 3BrC". 10IC has a higher electron attachment probability, forms a TNI with longer lifetime and dissociates faster, besides the fact that it has a heavier halogen substituent than 3BrC.

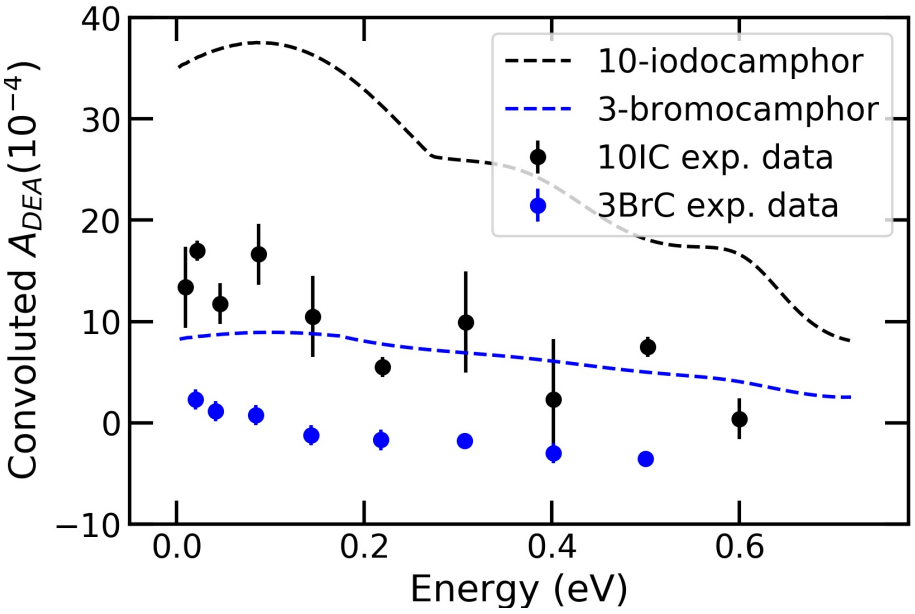

Figure 4.10: Convoluted DEA asymmetry calculated with the LCP approximation for 10IC (dark line) and 3BrC (blue line). Black and blue circles represent, respectively, the 10IC and 3BrC experimental values [12].

The calculated DEA asymmetries are about overestimated by a factor of three when compared with the experimental data. With the improved calculation using semi-LCP approximation, our results present magnitudes even larger, indicating how challenging it is obtaining accurate asymmetries. Besides that, the fragment current purity in the experiments should impact the magnitude of the data. The experimental setup employed by Dreiling and Gay does not perfectly distinguish anion fragments and electrons in the current asymmetry, where an electronic transmitted current could compose up to 20% of the total collected current [53]. In addition, the experimental setup would account for a current composed by the negative molecule species (parent anion), which could be present according to our calculations [41] (see Chapter 3). These two currents compose a background in the DEA asymmetry measurements and may result in a magnitude smaller than data obtained from a purely ion fragment current. Since we do not account for these background currents in our calculations, our calculations result in an overestimated a_{DEA}, and consequently an overestimated DEA asymmetry.

The convoluted 10IC A_{DEA} presents a decreasing curve as the energy increases, with maximum values between 0.0 eV and 0.1 eV, which is consistent with the experimental data. The calculated 3BrC asymmetry presents a similar pattern that does not agree

with experimental results. The sign change in the data has an unclear nature, remaining an unanswered question about the DEA asymmetry observed by Dreiling and Gay. An investigation concerning the spin-orbit coupling would be an important contribution to clarify this aspect, better describing the relative phase between $U_{\boldsymbol{k}}$ and $W_{\boldsymbol{k}}$.

Chapter 5

Conclusions

We presented a study showing that the characteristics of the transient negative ion species formed by the electron attachment has a fundamental role in the chiral sensitivity in halocamphor molecules. Our investigation is based on experimental results reported by Mayer and Kessler [1], as well as Dreiling and Gay [12]. The second experiment produced intriguing results for the dissociative electron attachment asymmetry for 3-bromocamphor, 3-iodocamphor and 10-iodocamphor, demanding a description of the electron attachment and dissociation process.

Our work consisted of a three step investigation. The first step was the most computationally expensive, in which we characterize the anionic states of the three halocamphor molecules. We performed electron scattering calculations, combined molecular dynamics and bond state calculations, as well as employed composed quantum chemistry methods, in order to characterize the dissociation mechanisms of interest for the halocamphor species. We show that the dissociation is triggered by electron attachment in the low-lying σ^* resonances, in the energy range considered in the experiments performed by Dreiling and Gay [12]. We understand that only these low-lying states should give rise to direct dissociation mechanisms (σ^* resonance formation followed by C-X stretch, where $X = Br^-, I^-$). The scattering calculations indicate resonance widths compatible with the related magnitudes of 3BrC and 10IC DEA asymmetries, and the more efficient dissociation explains the fourfold difference between the maximum DEA chiral asymmetries. However, our calculations indicating the dissociation for 3IC is a more complicated process. The σ^* state only has a resonance character for short bond lengths, suggesting the vibrational suppression of the attachment cross section for this molecule. The twofold

difference between the DEA asymmetries of the iodocamphor isomers could be related to the partial suppression of the cross section for electron attachment to 3IC, compared to 10IC.

For a more enlightening understanding of the asymmetries nature, an investigation of the dissociation process was required, allowing us to quantify and compare the anionic fragment production between the halocamphor compounds. The inclusion of spin-orbit coupling in the electron scattering problem is fundamental to reproduce the transmission and DEA asymmetries. The second step of our investigation was the formulation of a model for the spin-dependent electron scattering problem. Describing the dissociative electron attachment process is challenging, mainly for not-so-simple molecular structures like the halocamphors. We employed the well-known Feshbach formalism for the electron attachment process, using a simplified model assuming a pseudo-diatomic approximation and the local dependence of the resonance width in a single vibrational coordinate (C-X stretch) [40]. The novelty we bring is the spin-orbit coupling inclusion, and the formulation of the spin-dependent scattering and DEA matrix amplitudes. We also designed a model to account for the transmission and DEA asymmetries based on the formulation of the transmission asymmetry. We therefore have all the ingredients to understand the observed transmission and DEA asymmetries [1, 12, 50] and the relation of the magnitude asymmetries for the halocamphors.

The third step of the investigation was employing the developed model for the transmission asymmetry and estimating a feasible value for the spin-orbit coupling. Above 1 eV, resonances with a π^* character are found in the iodocamphor molecules, as well as a mixed σ^*/π^* resonance in 3BrC. They give rise to the transmission asymmetry peaks experimentally observed [1, 50]. We reproduced the transmission asymmetries and obtained good agreement with the experimental data. In the following, we performed simulations for the anionic states, where the dissociation mechanism of 3BrC and 10IC could be explored considering only the stretch of the halogen bond. We investigated how the molecules dissociate and how fast each compound evolves to the halide elimination. The dependence of the width of a resonance on the geometry of the molecule can be decisive when determining the DEA and electron scattering cross sections. As the vibrational relaxation takes place, the anionic state energy stabilizes and the width narrows down. This is directly related to the derivatives of the potential curve of the resonance as a function

of the stretching of the reaction coordinate. As the absolute values of the derivatives increase, the rate at which the resonance widths go to zero also increases, resulting in larger DEA cross sections. Finally, we reproduce the DEA asymmetry for 3BrC and 10IC. We obtained results from three different approximations employed, with different levels of accuracy. Our results are overestimated in comparison with the experimental data, pointing out how challenging the phenomenon of chiral sensitivity on the degradation species is. Nevertheless, we systematically obtained a 10IC DEA asymmetry from three to four times larger than the 3BrC, confirming that the character of the resonance, as well as the lifetime and topology of the TNI are deeply important in the DEA asymmetry. Our main contribution helpfully provides an understanding of the anomalously large asymmetry for 10IC.

Bibliography

[1] S. Mayer, C. Nolting, and J. Kessler, "Electron scattering from chiral molecules," *Journal of Physics B: Atomic, Molecular and Optical Physics*, vol. 29, no. 15, p. 3497, 1996.

[2] A. C. Evans, C. Meinert, C. Giri, F. Goesmann, and U. J. Meierhenrich, "Chirality, photochemistry and the detection of amino acids in interstellar ice analogues and comets," *Chemical Society Reviews*, vol. 41, no. 16, pp. 5447–5458, 2012.

[3] T. Ulbricht and F. Vester, "Attempts to induce optical activity with polarized β-radiation," *Tetrahedron*, vol. 18, no. 5, pp. 629–637, 1962.

[4] J. Geiger, G. Ewan, R. L. Graham, and D. MacKenzie, "Measurements on the longitudinal polarization of beta rays from p 32, y 90, pr 144, au 198, and bi 210 (rae)," *Physical Review*, vol. 112, no. 5, p. 1684, 1958.

[5] L. Hodge, F. Dunning, G. Walters, R. White, and G. Schroepfer Jr, "Degradation of dl-leucine with longitudinally polarised electrons," *Nature*, vol. 280, no. 5719, p. 250, 1979.

[6] D. Campbell and P. Farago, "Spin-dependent electron scattering from optically active molecules," *Nature*, vol. 318, no. 6041, pp. 52–53, 1985.

[7] S. Mayer and J. Kessler, "Experimental verification of electron optic dichroism," *Physical review letters*, vol. 74, no. 24, p. 4803, 1995.

[8] C. J. Joachain, "Quantum collision theory," 1975.

[9] P. Farago, "Spin-dependent features of electron scattering from optically active molecules," *Journal of Physics B: Atomic and Molecular Physics*, vol. 13, no. 18, p. L567, 1980.

[10] P. Farago, "Electron optic dichroism and electron optic activity," *Journal of Physics B: Atomic and Molecular Physics*, vol. 14, no. 22, p. L743, 1981.

[11] R. A. Hegstrom, "β decay and the origins of biological chirality: theoretical results," *Nature*, vol. 297, no. 5868, p. 643, 1982.

[12] J. Dreiling, F. Lewis, J. Mills, and T. J. Gay, "Anomalously large chiral sensitivity in the dissociative electron attachment of 10-iodocamphor," *Physical review letters*, vol. 116, no. 9, p. 093201, 2016.

[13] A. Rich, J. Van House, and R. Hegstrom, "Calculation of a mirror asymmetric effect in electron scattering from chiral targets," *Physical Review Letters*, vol. 48, no. 19, p. 1341, 1982.

[14] D. Walker, "Electron scattering from optically active molecules," *Journal of Physics B: Atomic and Molecular Physics*, vol. 15, no. 8, p. L289, 1982.

[15] A. Scheer, G. A. Gallup, and T. J. Gay, "An investigation of electron helicity density in bromocamphor and dibromocamphor as a source of electron circular dichroism," *Journal of Physics B: Atomic, Molecular and Optical Physics*, vol. 39, no. 9, p. 2169, 2006.

[16] I. Anusiewicz, M. Sobczyk, J. Berdys-Kochanska, P. Skurski, and J. Simons, "A theoretical model for indirect dissociative electron attachment," *The Journal of Physical Chemistry A*, vol. 109, no. 3, pp. 484–492, 2005.

[17] K. Blum and D. Thompson, "Spin-dependent electron scattering from oriented molecules," *Journal of Physics B: Atomic, Molecular and Optical Physics*, vol. 22, no. 11, p. 1823, 1989.

[18] R. F. da Costa, M. T. d. N. Varella, M. H. Bettega, and M. A. Lima, "Recent advances in the application of the schwinger multichannel method with pseudopotentials to electron-molecule collisions," *The European Physical Journal D*, vol. 69, no. 6, p. 159, 2015.

[19] F. Kossoski, M. Bettega, and M. d. N. Varella, "Shape resonance spectra of uracil, 5-fluorouracil, and 5-chlorouracil," *The Journal of chemical physics*, vol. 140, no. 2, p. 024317, 2014.

[20] J. Kopyra, H. Abdoul-Carime, F. Kossoski, and M. d. N. Varella, "Electron driven reactions in sulphur containing analogues of uracil: the case of 2-thiouracil," *Physical Chemistry Chemical Physics*, vol. 16, no. 45, pp. 25054–25061, 2014.

[21] F. Kossoski, J. Kopyra, and M. d. N. Varella, "Anion states and fragmentation of 2-chloroadenine upon low-energy electron collisions," *Physical Chemistry Chemical Physics*, vol. 17, no. 43, pp. 28958–28965, 2015.

[22] L. Cornetta, F. Kossoski, and M. d. N. Varella, "Transient anion spectra of the potential radiosensitizers 5-cyanateuracil and 5-thiocyanateuracil," *The Journal of chemical physics*, vol. 147, no. 21, p. 214310, 2017.

[23] H. Feshbach, "H. feshbach, ann. phys.(ny) 5, 357 (1958)," *Ann. Phys.(NY)*, vol. 5, p. 357, 1958.

[24] W. Domcke, "Analytic theory of resonances, virtual states and bound states ion electron-molecule scattering and related processes," *Journal of Physics B: Atomic and Molecular Physics*, vol. 14, no. 24, p. 4889, 1981.

[25] R. Fandreyer, D. Thompson, and K. Blum, "Attenuation of longitudinally polarized electron beams by chiral molecules," *Journal of Physics B: Atomic, Molecular and Optical Physics*, vol. 23, no. 17, p. 3031, 1990.

[26] J. J. Sakurai and E. D. Commins, "Modern quantum mechanics, revised edition," 1995.

[27] F. Blanco and G. García, "Interference effects in the electron and positron scattering from molecules at intermediate and high energies," *Chemical Physics Letters*, vol. 635, pp. 321–327, 2015.

[28] K. Gottfried and T.-M. Yan, *Quantum mechanics: fundamentals*. Springer Science & Business Media, 2013.

[29] B. A. Lippmann and J. Schwinger, "Variational principles for scattering processes. i," *Physical Review*, vol. 79, no. 3, p. 469, 1950.

[30] S. Geltman, *Topics in atomic collision theory*, vol. 30. Academic Press, 2013.

[31] M. A. Lima and V. McKoy, "Aspects of the schwinger multichannel variational formulation," *Physical Review A*, vol. 38, no. 1, p. 501, 1988.

[32] C. Winstead and V. McKoy, "Electron collisions with nitrous oxide," *Physical Review A*, vol. 57, no. 5, p. 3589, 1998.

[33] F. Kossoski and M. Bettega, "Low-energy electron scattering from the aza-derivatives of pyrrole, furan, and thiophene," *The Journal of Chemical Physics*, vol. 138, no. 23, p. 234311, 2013.

[34] C. W. Bauschlicher Jr, "The construction of modified virtual orbitals (mvo's) which are suited for configuration interaction calculations," *The Journal of Chemical Physics*, vol. 72, no. 2, pp. 880–885, 1980.

[35] G. Bachelet, D. Hamann, and M. Schlüter, "Pseudopotentials that work: From h to pu," *Physical Review B*, vol. 26, no. 8, p. 4199, 1982.

[36] M. H. Bettega, A. P. Natalense, M. A. Lima, and L. G. Ferreira, "Note on the generation of gaussian bases for pseudopotential calculations," *International journal of quantum chemistry*, vol. 60, no. 4, pp. 821–824, 1996.

[37] J. S. d. Santos, R. F. da Costa, and M. T. d. N. Varella, "Low-energy electron collisions with glycine," *The Journal of chemical physics*, vol. 136, no. 8, p. 02B616, 2012.

[38] H. Feshbach, "Unified theory of nuclear reactions," *Annals of Physics*, vol. 5, no. 4, pp. 357–390, 1958.

[39] H. Feshbach, "A unified theory of nuclear reactions. ii," *Annals of Physics*, vol. 19, no. 2, pp. 287–313, 1962.

[40] W. Domcke, "Theory of resonance and threshold effects in electron-molecule collisions: The projection-operator approach," *Physics reports*, vol. 208, no. 2, pp. 97–188, 1991.

[41] J. C. Ruivo, F. Kossoski, and M. T. d. N. Varella, "Anion states of halocamphor molecules: insights into chirally sensitive dissociative electron attachment," *Physical Chemistry Chemical Physics*, vol. 23, no. 32, pp. 17616–17624, 2021.

[42] M. J. Frisch, G. W. Trucks, H. B. Schlegel, G. E. Scuseria, M. A. Robb, J. R. Cheeseman, G. Scalmani, V. Barone, B. Mennucci, G. A. Petersson, H. Nakatsuji, M. Caricato, X. Li, H. P. Hratchian, A. F. Izmaylov, J. Bloino, G. Zheng, J. L. Sonnenberg, M. Hada, M. Ehara, K. Toyota, R. Fukuda, J. Hasegawa, M. Ishida, T. Nakajima, Y. Honda, O. Kitao, H. Nakai, T. Vreven, J. A. Montgomery, Jr., J. E. Peralta, F. Ogliaro, M. Bearpark, J. J. Heyd, E. Brothers, K. N. Kudin, V. N. Staroverov, R. Kobayashi, J. Normand, K. Raghavachari, A. Rendell, J. C. Burant, S. S. Iyengar, J. Tomasi, M. Cossi, N. Rega, J. M. Millam, M. Klene, J. E. Knox, J. B. Cross, V. Bakken, C. Adamo, J. Jaramillo, R. Gomperts, R. E. Stratmann, O. Yazyev, A. J. Austin, R. Cammi, C. Pomelli, J. W. Ochterski, R. L. Martin, K. Morokuma, V. G. Zakrzewski, G. A. Voth, P. Salvador, J. J. Dannenberg, S. Dapprich, A. D. Daniels, Ö. Farkas, J. B. Foresman, J. V. Ortiz, J. Cioslowski, and D. J. Fox, "Gaussian09 Revision E.01." Gaussian Inc. Wallingford CT 2009.

[43] K. A. Peterson, D. Figgen, E. Goll, H. Stoll, and M. Dolg, "Systematically convergent basis sets with relativistic pseudopotentials. ii. small-core pseudopotentials and correlation consistent basis sets for the post-d group 16–18 elements," *The Journal of chemical physics*, vol. 119, no. 21, pp. 11113–11123, 2003.

[44] M. S. Gordon and M. W. Schmidt, "Advances in electronic structure theory: Gamess a decade later," in *Theory and applications of computational chemistry*, pp. 1167–1189, Elsevier, 2005.

[45] T. H. Dunning Jr, "Gaussian basis functions for use in molecular calculations. i. contraction of (9s5p) atomic basis sets for the first-row atoms," *The Journal of Chemical Physics*, vol. 53, no. 7, pp. 2823–2833, 1970.

[46] S. McKechnie, G. H. Booth, A. J. Cohen, and J. M. Cole, "On the accuracy of density functional theory and wave function methods for calculating vertical ionization energies," *The Journal of chemical physics*, vol. 142, no. 19, p. 194114, 2015.

[47] P. Skurski, M. Gutowski, and J. Simons, "How to choose a one-electron basis set to reliably describe a dipole-bound anion," *Int. J. Quantum Chem.*, vol. 80, no. 4-5, pp. 1024–1038, 2000.

[48] S. W. Staley and J. T. Strnad, "Calculation of the energies of. pi.* negative ion resonance states by the use of koopmans' theorem," *The Journal of Physical Chemistry*, vol. 98, no. 1, pp. 116–121, 1994.

[49] D. Chen and G. A. Gallup, "The relationship of the virtual orbitals of self-consistent-field theory to temporary negative ions in electron scattering from molecules," *The Journal of Chemical Physics*, vol. 93, no. 12, pp. 8893–8901, 1990.

[50] J. Dreiling, F. Lewis, and T. Gay, "Spin-polarized electron transmission through chiral halocamphor molecules," *Journal of Physics B: Atomic, Molecular and Optical Physics*, vol. 51, no. 21, p. 21LT01, 2018.

[51] D. Marx and J. Hutter, *Ab initio molecular dynamics: basic theory and advanced methods*. Cambridge University Press, 2009.

[52] J. Hutter, M. Iannuzzi, F. Schiffmann, and J. VandeVondele, "Cp2k: atomistic simulations of condensed matter systems," *Wiley Interdisciplinary Reviews: Computational Molecular Science*, vol. 4, no. 1, pp. 15–25, 2014.

[53] J. Dreiling and T. Gay, "Chirally sensitive electron-induced molecular breakup and the vester-ulbricht hypothesis," *Physical review letters*, vol. 113, no. 11, p. 118103, 2014.

[54] L. A. Curtiss, P. C. Redfern, and K. Raghavachari, "Gaussian-4 theory using reduced order perturbation theory," *J. Chem. Phys.*, vol. 127, no. 12, p. 124105, 2007.

[55] J. Dreiling and T. J. Gay, "Chirally-sensitive electron-molecule interactions," in *Journal of Physics: Conference Series*, vol. 635, p. 012015, IOP Publishing, 2015.

[56] H. Estrada and W. Domcke, "Non-markovian dynamics of electron-molecule collision complexes," *Physical Review A*, vol. 40, no. 3, p. 1262, 1989.

[57] P. Gertitschke and W. Domcke, "Time-dependent wave-packet description of dissociative electron attachment," *Physical Review A*, vol. 47, no. 2, p. 1031, 1993.

[58] F. Kossoski, M. d. N. Varella, and M. Barbatti, "On-the-fly dynamics simulations of transient anions," *The Journal of chemical physics*, vol. 151, no. 22, p. 224104, 2019.

[59] C. W. McCurdy and J. L. Turner, "Wave packet formulation of the boomerang model for resonant electron–molecule scattering," *The Journal of Chemical Physics*, vol. 78, no. 11, pp. 6773–6779, 1983.

[60] C. Mündel, M. Berman, and W. Domcke, "Nuclear dynamics in resonant electron-molecule scattering beyond the local approximation: Vibrational excitation and dissociative attachment in h 2 and d 2," *Physical Review A*, vol. 32, no. 1, p. 181, 1985.

[61] E. P. Wigner, "On the behavior of cross sections near thresholds," *Physical Review*, vol. 73, no. 9, p. 1002, 1948.